Preparation of $CuInSe_2$ and $CuInGaSe_2$ nanoparticles and thin films for solar cells applications

A thesis submitted to the University of Manchester for the Degree of Master of Philosophy in the Faculty of Engineering and Physical Sciences

2010

Sajid Nawaz Malik

School of Chemistry, The University of Manchester,
Oxford Road, Manchester M13 9PL, UK

Table of Contents

Title Page 1

Table of Contents 2

List of Figures 5

List of Tables 10

Abstract 11

Declaration 13

Copyright 14

Acknowledgements 15

Dedication 17

Abbreviations 18

Chapter 1 **Introduction**

1.1. Energy 20

1.2. Solar energy 21

1.3. Solar photovoltaic technologies 22

1.4. Background semiconductor theory 24

1.4.1. Differences between semiconductors, insulators and conductors... 26

1.4.2. Direct and indirect bandgap semiconductors 29

1.4.3. Intrinsic semiconductors 30

1.4.4. Extrinsic semiconductors 31

1.5. Thin film deposition techniques 34

1.5.1. Chemical vapour deposition 34

1.5.2. Metal organic chemical vapour deposition 35

1.5.3. Aerosol-assisted chemical vapour deposition (AACVD) 35

1.6. Nanoparticles 37

1.6.1. Preparation techniques for nanoparticles 38

1.7. Solar cells based on nanocrystals 39

1.8. Copper selenide 42

1.9. Indium selenide 44

1.10. Gallium selenide 46

1.11. I-III-VI_2 chalcopyrite semiconductors …………………………………………48
1.11.1. Factors affecting the performance of I-III-VI_2 materials ……...50
1.11.2. Deposition techniques for I-III-VI_2 semiconductors …………..51
1.11.3. Selenization of metallic precursor layers ………………..……..54
1.11.4. Chemical vapour deposition ……………………………………54
1.12. Phosphorus-chalcogen-metal ring system containing compounds as single source precursors ………………………………………………………57
1.13. Aim and objectives ……………………………………………………….60
References ……………………………………………………………….62

Chapter 2 **Experimental**

2.1 Chemicals ……………………………………………………………………77
2.2 Experimental …………………………………………………………………77
2.3 Synthesis of $[HNEt_3][^iPr_2PSe_2]$ ligand ……………………………………..77
2.4 Synthesis of precursors ……………………………………………………..78
2.4.1 Synthesis of copper precursor $[Cu_4(^iPr_2PSe_2)_4]$ …………………....78
2.4.2 Synthesis of indium precursor $In(^iPr_2PSe_2)_3$ ………………………78
2.4.3 Synthesis of gallium precursor $Ga(^iPr_2PSe_2)_3$ ……………………..79
2.5 Deposition of thin films by AACVD ………………………………………...79
2.6 Growth of nanoparticles ………………………………………………….....80
2.6.1 Growth of indium selenide nanoparticles …………………………80
2.6.2 Attempted growth of gallium selenide nanoparticles …………....81
2.6.3 Growth of copper selenide nanoparticles …………………………81
2.6.4 Growth of copper indium diselenide nanoparticles ……………81
2.6.5 Growth of copper gallium diselenide nanoparticles …………...82
2.6.6 Growth of copper indium gallium diselenide nanoparticles …..82
2.7 Characterization of thin films and nanoparticles ……..………………..82
2.7.1 Uv-Vis optical absorption spectroscopy …………………………..83
2.7.2 Photoluminescence (PL) studies …………………………………..83
2.7.3 Powder X-ray diffraction ……………………………………………83
2.7.4 Scanning electron microscopy (SEM) and energy dispersive X-ray (EDX) analysis ………………………………………………………..….84

2.7.5 Transmission electron microscopy (TEM) ………………………...84
References ………………………………………………………..85

Chapter 3 **Results and Discussion**

3.1 Results and Discussion ……………………………………………..……87
3.2 Synthesis and characterization of ionic ligand …………………………...89
3.3 Synthesis of $M_x[^iPr_2PSe_2]_y$ (M=In, Ga, Cu) complexes ………………… 89
3.4 Growth of nanomaterials ……………………………………………….....91
3.5 Growth of copper selenide nanostructures ……………………………….92
3.5.1 Copper selenide thin films …………………………………………92
3.5.2 Copper selenide nanoparticles …………………………………….94
3.6 Growth of indium selenide nanostructures ……………………………….97
3.6.1 Indium selenide thin films ………………………………………….97
3.6.2 Indium selenide nanoparticles ……………………………………100
3.7 Growth of gallium selenide nanostructures …………………………..…103
3.7.1 Gallium selenide thin films ………………………………………..103
3.7.2 Attempted growth of gallium selenide nanoparticles …………..106
3.8 Growth of copper indium diselenide nanostructures …………………...107
3.8.1 Copper indium diselenide thin films ……………………………...107
3.8.2 Copper indium diselenide nanoparticles ………………………...111
3.9 Growth of copper gallium diselenide nanostructures …………………..114
3.9.1 Copper gallium diselenide thin films ……………………………..114
3.9.2 Copper gallium diselenide nanoparticles ………………………..118
3.10 Growth of copper indium gallium diselenide (CIGS) nanostructures …122
3.10.1 Copper indium gallium diselenide thin films ……………………122
3.10.2 Copper indium gallium diselenide nanoparticles ……………....128
References ………………………………………………………………133

Chapter 4 **Conclusion**……………………………………………………………136

List of Figures

Figure 1.1 Current market share of various PV technologies ……………….23

Figure 1.2 Schematic illustration of typical band diagrams for a metal, an intrinsic semiconductor and an insulator…………………………..26

Figure 1.3 Fermi-Dirac distribution function. Theoretical curves at 0 K (T=0), and two higher temperatures where (T_2>T_1>0) …………………..28

Figure 1.4 Part of the photoelectron spectrum of metallic ruthenium at three different temperatures. The smooth line is theoretical and the dotted experimental……………………………………………….28

Figure 1.5 Energy band diagram for direct and indirect semiconductors ….29

Figure 1.6 Electron Diagram diagrams representing (a) a donor impurity located within the band gap and just below the conduction band; (b) Subsequent excitation of the electron from the band gap to the conduction band…………………………………………………...32

Figure 1.7 Electron band structure for (a) an acceptor impurity level, located within the band gap and lying just above the valence band; (b) excitation of an electron into the acceptor level, leaving behind a positive hole in the valence band…………………………………..33

Figure 1.8 Diagram showing the larger band gap in nanoparticles in comparison to bulk semiconductors ……………………………….37

Figure 1.9 Schematic representation of $CuInSe_2$ chalcopyrite crystal structure ……………………………………………………………………….50

Figure 2.1 Schematic of an AACVD Kit ………………………………………..80

Figure 3.1 $(\alpha th\upsilon)^2$ vs. hυ plots of $Cu_{2-x}Se$ films deposited at 475 °C showing a direct bandgap of ~ 2.1 eV ………………………………………….92

Figure 3.2 XRD patterns of as deposited thin films of $Cu_{2-x}Se$ at 350 °C, 375 ºC, 425 ºC and 475 ºC. Red vertical lines at the bottom show standard ICDD pattern (00-006-680) for berzelianite phase of $Cu_{2-x}Se$ material …………………………………………………..93

Figure 3.3 SEM images of the $Cu_{2-x}Se$ films deposited at (a) 350 °C (b) 375 °C (c) 425 °C and (d) 475 °C ………………………………………94

Figure 3.4 UV-vis absorption spectrum of $Cu_{2-x}Se$ nanoparticles synthesized from 0.3 g precursor at 250 °C……………………………………...95

Figure 3.5 (A) XRPD pattern of cubic $Cu_{2-x}Se$ (JCPDS 06-0680) nanoparticles synthesized at 250 °C. (B) XRD patterns of cubic $Cu_{2-x}Se$ (JCPDS 06-0680) nanoparticles synthesized from (a) 0.3 g precursor at 250 °C, (b) 0.15 g precursor at 250 °C, (c) 0.15 g precursor at 300 °C……………………………………………………..96

Figure 3.6 (a-b) TEM (c-d) HR-TEM images of $Cu_{2-x}Se$ nanoparticles grown from thermolysis of $[Cu_4(^iPr_2PSe_2)_4]$ precursor at 250 °C ……….97

Figure 3.7 Plot of $(\alpha h\upsilon)^2$ *vs* band gap of γ-In_2Se_3 thin film showing bandgap of ~ 1.82 eV ……………………………………………………98

Figure 3.8 XRD pattern of γ-In_2Se_3 thin film at 450 °C. Red lines below show standard ICDD pattern 00-040-1407 for γ-phase of In_2Se_3 ……..99

Figure 3.9 SEM images of as deposited γ-In_2Se_3 thin film at 450 °C………..99

Figure 3.10 Room temperature (a) Optical absorption spectrum and (b) emission spectrum of toluene suspension of HDA capped InSe nanoparticles grown at 270 °C …………………………......100

Figure 3.11 XRD pattern of HDA capped In_2Se_3 nanoparticles grown at 250 °C ………………………………………………………………101

Figure 3.12 (a-c) TEM and (d) HR-TEM images of HDA capped indium selenide nanoparticles grown at 270 °C …………………………102

Figure 3.13 Plot of $(\alpha h\upsilon)^2$ *vs* band gap of Ga_2Se_3 thin films (bandgap ~ 2.15 eV) ……………………………………………………………..…103

Figure 3.14 XRD patterns of Ga_2Se_3 thin films deposited at 400 ºC (red), 450 ºC (black) and 500 (blue) ºC indexed with standard ICDD pattern 01-076-0975 …………………………………………………………...104

Figure 3.15 (a – b) SEM images of thin film of monoclinic Ga_2Se_3 deposited at 500 ºC (c – d) SEM image of monoclinic Ga_2Se_3 after annealing at 400 ºC for 14 hours ………………………………………………...105

Figure 3.16 1D and 2D AFM images of as deposited Ga_2Se_3 thin films at 500 ºC and Histogram of AFM image shown in Figure 5 showing size distribution along with surface roughness ………………………..106

Figure 3.17 XRD pattern of gallium selenate hydrate nanoparticles corresponding to standard ICDD pattern 00-022-0301 ………..107

Figure 3.18 Plot of $(\alpha h\upsilon)^2$ *vs* band gap of $CuInSe_2$ thin films showing band gap of 1.17 eV…………………………………………………………108

Figure 3.19 XRPD patterns of as deposited $CuInSe_2$ thin films in 1:4 ratios at temperatures (a) 350 °C, (b) 400 °C, (c) 450 °C and (d) 500 °C..108
Figure 3.20 SEM images of as deposited thin films of CuInSe2 at (a) 400 °C, (b) 450 °C and (c) 500 °C. Figures (d-f) show various magnifications of the thin film deposited at 400 °C ……………109
Figure 3.21 1D and 2D AFM images of as deposited $CuInSe_2$ thin films at 450 °C along with AFM histogram showing grain size distribution and surface roughness …………………………………………………110
Figure 3.22 Room temperature Vis-NIR absorption spectra of HDA capped $CuInSe_2$ nanoparticles grown at different temperatures (120 – 210 °C) showing red shift of absorption band edge with increased growth temperatures……………………………………………….……111
Figure 3.23 XRPD pattern of HDA capped $CuInSe_2$ nanoparticles grown at (a)120 °C (b) 150 °C (c) 180 °C and (d) 210 °C. Red lines below represent standard ICDD pattern (00-040-1487) for tetragonal $CuInSe_2$ phase…………………………………………………...112
Figure 3.24 (a-d) TEM images (e) HR-TEM image and (f) SAED pattern of the HDA capped $CuInSe_2$ Quantum dots grown at 180 °C (g) Histogram showing size distribution of $CuInSe_2$ Quantum dots …………………………………………………………………….....113
Figure 3.25 Plot of $(\alpha h\upsilon)^2$ *vs* band gap of $CuGaSe_2$ thin films showing band gap energy of 1.74 eV……………….…………………………..115
Figure 3.26 XRD pattern of as deposited $CuGaSe_2$ thin films at (a) 350 °C, (b) 400 °C, (c) 450 °C and (d) 500 °C from 1:4 molar ratios of Cu and Ga precursors …………………….…………………………………116
Figure 3.27 SEM images of as deposited $CuGaSe_2$ thin films at (a) 300 °C, (b) 350 °C, (c) 400 °C, (d) 450 °C and (e) & (f) 500 °C……………...117
Figure 3.28 1D and 3D AFM images of as grown $CuGaSe_2$ thin films at 450°C from 1:4 equivalent of $[Cu_4({}^iPr_2P_2Se_2)_4]$ and $[Ga({}^iPr_2PSe_2)_3]$ respectively along with AFM histogram showing size distribution and surface roughness ……………………………………………..118
Figure 3.29 UV-Vis absorption spectrum of HDA capped $CuGaSe_2$ nanoparticles grown at 250 °C……………………………………..119

Figure 3.30 XRD pattern of HDA capped $CuGaSe_2$ nanoparticles grown at 250 °C ……………………………………………………………………..120
Figure 3.31 (A - D) TEM images of HDA capped $CuGaSe_2$ nanoparticles grown at 250 °C (e) Histogram showing size distribution of HDA capped $CuGaSe_2$ nanoparticles ……………………………………………121
Figure 3.32 (a) XRD patterns of as deposited $CuIn_{1-x}Ga_xSe_2$ in 1:1:1 ratio showing $CuIn_{0.7}Ga_{0.3}Se_2$ along with $CuGaSe_2$ as secondary phase, (b) XRD patterns of as deposited $CuIn_{1-x}Ga_xSe_2$ in 1:2:4 ratios at 450 ºC showing $CuIn_{0.7}Ga_{0.3}Se_2$ along with $CuInSe_2$, $Cu_{2-x}Se$ and α-In_2Se_3 as additional phases…………………………………...122
Figure 3.33 XRD pattern of as deposited $CuIn_{0.7}Ga_{0.3}Se_2$ thin films at (a) 300 °C, (b) 350 °C, (c) 400 °C, (d) 450 °C and (e) 500 °C from 1:2:2 molar equivalents of $[Cu_4(^iPr_2P_2Se_2)_4]$, $[In(^iPr_2PSe_2)_3]$ and $[Ga(^iPr_2PSe_2)_3]$ respectively……………………………………...124
Figure 3.34 Plot of $(\alpha h\upsilon)^2$ *vs* band gap of $CuIn_{0.7}Ga_{0.3}Se_2$ thin films showing band gap energy of 1.46 eV……………………………………..124
Figure 3.35 SEM images of as deposited $CuIn_{0.7}Ga_{0.3}Se_2$ at (a) 350 °C, (b) 400 °C, (c) 450 °C and (d) 500 °C from 1:2:2 molar equivalent of $[Cu_4(^iPr_2P_2Se_2)_4]$, $[In(^iPr_2PSe_2)_3]$ and $[Ga(^iPr_2PSe_2)_3]$…………..125
Figure 3.36 (a) 2D (b) 3D AFM image of as deposited $CuIn_{0.7}Ga_{0.3}Se_2$ thin films at 400 °C with Root mean square roughness 55.46 nm….126
Figure 3.37 (a) SEM image of $CuIn_{0.7}Ga_{0.3}Se_2$ at 450 °C, (b) 2D, (c) 3D AFM images of as deposited $CuIn_{0.7}Ga_{0.3}Se_2$ at 450 °C with Root mean square roughness 44.50 nm, (d) 3D AFM image of nano indent type microstructures found at the surface of the subject film ….126
Figure 3.38 SEM images of as deposited $CuIn_{0.7}Ga_{0.3}Se_2$ thin films in 1:2:4 ratio at 450 ºC showing various secondary phases especially random distribution of big grains of $CuInSe_2$……………………127
Figure 3.39 Powder XRD Pattern of various stoichiometric compositions of HDA capped $CuInGaSe_2$ nanoparticles indexed with standard ICDD Patterns for $CuIn_{0.7}Ga_{0.3}Se_2$, $CuIn_{0.5}Ga_{0.5}Se_2$ and $CuIn_{0.4}Ga_{0.6}Se_2$. . XRD Patterns shift to higher diffraction angles with increase in gallium content…………………………………...130

Figure 3.40 Plot of the Gallium composition variable x in $CuIn_{(1-x)}Ga_xSe_2$ verus lattice parameter 'c' ……………………………………………..130

Figure 3.40 Magnification of (112) peak of XRPD patterns of various compositions of CIGS. Vertical lines show standard ICDD patterns 00-35-1102 (red) and 00-35-1101 (blue) ………………………..131

Figure 3.41 (a-d) show TEM images of tetragonal$CuIn_{0.7}Ga_{0.3}Se_2$ quantum dots (e) SAED pattern of the $CuIn_{0.7}Ga_{0.3}Se_2$ nanoparticles and (f) Histogram representing size distribution for $CuIn_{0.7}Ga_{0.3}Se_2$ quantum dots ………………………………………………………132

List of Tables

Table 3.1 Summary of the synthesis process for diisopropyldiselenophosphinato- metal complexes ………………79

Table 3.2 Summary of H NMR data of diisopropyldiselenophosphinatometal complexes ……………………………………………….……………..80

Table 3.3 Summary of the combination of precursors used and stoichiometric compositions of CIGS materials obtained after reaction …………128

Abstract

In present work, thin films and nanoparticles of copper selenide ($Cu_{2-x}Se$), indium selenide (In_2Se_3), copper indium diselenide ($CuInSe_2$), copper gallium diselenide ($CuGaSe_2$) and copper indium gallium diselenide ($CuIn_{(1-x)}Ga_xSe_2$) were deposited from diisopropyldiselenophosphinatometal complexes $M_x[^iPr_2PSe_2]_y$ (M = Cu, In, Ga). Thin films were deposited onto glass substrates by AACVD method whereas nanoparticles were grown by colloidal method which involved thermal decomposition of precursors in HDA/TOP system at desired growth temperature. The semiconductor thin films and nanoparticles obtained were characterized by UV-Vis spectroscopy, X-ray powder diffraction (XRPD), scanning electron microscopy (SEM), atomic force microscopy (AFM), transmission electron microscopy (TEM) and energy dispersive X-ray (EDX) analysis. Thin films of copper selenide were deposited at temperatures ranging from 300 to 475 ^{0}C, using copper complex $[Cu_4(^iPr_2PSe_2)_4]$ as single source precursor (SSP). Berzelianite phase of $Cu_{2-x}Se$ (ICDD pattern 00-006-680) with predominantly triangular morphology was deposited at 350 and higher temperatures whereas thermal degradation of precursor in HDA/TOP system resulted in growth of colloids having 15 ± 2.5 nm size. AACVD process involving $In(^iPr_2PSe_2)_3$ as SSP yielded uniform and well adhered films of γ-In_2Se_3 (ICDD pattern 00-040-1407) having cylinderical morphology. Bandgap of the films deposited at 400 °C was found to be 1.82 eV. Nanoparticles representing hexagonal phase of In_2Se_3 (ICDD pattern 00-012-0117) were obtained by degradation of this precursor in HDA/TOP at 270 °C. Size of the nanocrystals was found to be 5.0 nm (± 1.1). Copper indium diselenide ($CuInSe_2$) thin films were deposited from 1:4 molar equivalents of $[Cu_4(^iPr_2PSe_2)_4]$ and $[In(^iPr_2PSe_2)_3]$ precursors, respectively at temperatures ranging from 350 to 500 ^{0}C. Tetragonal phase of $CuInSe_2$ (ICDD pattern 01-075-0107) was deposited and the films had an optical bandgap of around 1.17 eV. Similarly, thermolysis of 1:4 molar equivalents of $[Cu_4(^iPr_2PSe_2)_4]$ and $[In(^iPr_2PSe_2)_3]$ precursors in HDA/TOP at temperatures ranging from 120 ^{0}C to 210 ^{0}C yielded monodispersed

spherical particles. Size of the nanoparticles obtained showed strong dependance upon the growth temperature and reaction duration. Higher growth temperatures and longer reaction durations resulted in formation of larger nanoparticles. Tetragonal phase of chalcopyrite $CuGaSe_2$ (ICDD pattern 00-035-1100) was deposited from AACVD of 1:4 molar equivalents of $[Cu_4(^iPr_2PSe_2)_4]$ and $[Ga(^iPr_2PSe_2)_3]$ precursors at 400 - 500 °C. Similarly, thermolysis of 1:4 molar equivalents of these precursors in HDA/TOP at 250 °C yielded polycrystalline tetragonal chalcopyrite nanocrystals of $CuGaSe_2$. Thin films of CIGS material were deposited at temperatures ranging from 300 to 500 ºC by using different molar equivalents of copper, indium and gallium precursors. Best films were deposited and by using 1:2:2 molar equivalents of copper, indium and gallium precursor, respectively at 450 °C. Colloidal synthesis of $CuIn_{(1-x)}Ga_xSe_2$ nanoparticles was also carried out by thermolysing different molar equivalents of copper, indium and gallium precursors in HDA/TOP at 250 °C. Tetragonal chalcopyrite phase of the material was deposited in all cases. It was possible to tune the In/Ga ratio across the whole range of stoichiometric compositions with value of *x* ranging from 0 to 1 using this approach. Different stoichiometric compositions of CIGS nanoparticles grown in the present work include $CuIn_{0.81}Ga_{0.19}Se_2$, $CuIn_{0.68}Ga_{0.32}Se_2$, $CuIn_{0.54}Ga_{0.46}Se_2$, $CuIn_{0.47}Ga_{0.53}Se_2$, and $CuIn_{0.19}Ga_{0.81}Se_2$. Size of the nanoparticles was found to be around 14 nm with standard deviation of 2.21 nm.

Declaration

I hereby declare that no portion of the work referred to in the thesis has been submitted in support of an application for another degree or qualification of the University of Manchester or any other university or other institute of learning.

Sajid Nawaz Malik

Copyright

The author of this thesis (including any appendices and/or schedules to this thesis) owns any copyright in it (the "Copyright") and he has given The University of Manchester the right to use such Copyright for any administrative, promotional, educational and/or teaching purposes.

Copies of this thesis, either in full or in extracts, may be made only in accordance with the regulations of the John Rylands University Library of Manchester. Details of these regulations may be obtained from the Librarian. This page must form part of any such copies made.

The ownership of any patents, designs, trade marks and any and all other intellectual property rights except for the Copyright (the "Intellectual Property Rights") and any reproductions of copyright works, for example graphs and tables ("Reproductions"), which may be described in this thesis, may not be owned by the author and may be owned by third parties. Such Intellectual Property Rights and Reproductions cannot and must not be made available for use without the prior written permission of the owner(s) of the relevant Intellectual Property Rights and/or Reproductions.

Further information on the conditions under which disclosure, publication and exploitation of this thesis, the Copyright and any Intellectual Property Rights and/or Reproductions described in it may take place is available from the Head of School of Chemistry.

ACKNOWLEDGEMENT

I owe my profound thanks and deepest gratitude to Almighty ALLAH, Creator of the universe, and worthy of all praises, who blessed me with the potential, ability and determination to complete this research work. This is his extreme blessing on me for which I cannot adequately thank.

I wish to express my heartfelt thanks, respect and admiration to my supervisor, Prof. Dr. Paul O'Brien, Head, School of Chemistry, The University of Manchester for accepting me as research student in his prestigious research group, his kind supervision and paramount support during the course of this study. He is one of the most learned researchers and I really feel proud of being his student.

I am immensely indebted to Dr. Mohammad Azad Malik, Senior Research Fellow, School of Chemistry, The University of Manchester. He is an excellent advisor and a good friend. He provided me the knowledge base for my research activities, enabled me to learn more about this field and provided me the opportunities to collaborate with other researchers. I would also like to thank Dr. Mohammad Afzaal for his commendable and valued help, whenever I required.

My sincere gratitude is due to Defence Science & Technology Organization (DESTO), Government of Pakistan for providing me this opportunity and financial support to undertake M. Phil studies at The University for Manchester. This study would not have been possible without this financial support.

This acknowledgment will be incomplete if I do not appreciate with thanks, the moral support and technical help extended by my worthy colleague Dr. Nazre Haider. He has always been a source of inspiration during whole course of my research work. Furthermore, I wish to extend my heartiest thanks to all my research fellows of the POB group, especially Javeed Akhtar, Sumera Mahboob, Kibriya Ahmad, Khalid Hussain Thebo, Karthik Ramaswamy, Rana Farhat, Masood Akhtar and Dr. Tariq, for all the interactions, both scientific and personal. Their earnest support has been very helpful and they have had a great impact on my research and my life. My work was certainly made better with their consultations. My special thanks are due to Weerakanya

Maneeprakorn and Javeed Akhtar for their help in the Transmission Electron Microscopy (TEM) of my samples.

Understanding and unconditional support, extended by my family has played a key role in my research efforts. I wish to thank my parents for teaching me to be sparing, honest, obliging, generous, and hardworking. Last, but certainly not least, I would like to thank my wife for taking care of everything so that I can concentrate on my research. Moreover, special thanks to my One-year-old son, Muhammad Hassan Nawaz, who let me to learn patience, circumspection, and responsibility.

Dedication

In memory of the life in Manchester, United Kingdom

Abbreviations

AACVD	aerosol-assisted chemical vapour deposition
^{i}Pr	iso-propyl group
Eg	band gap energy
EDAX	energy dispersive X-ray analysis
Eq	equation
JCPDS	joint committee of powder diffraction standard
ICDD	international centre for diffraction data
LED	light emitting diode
Me	methyl group
MOCVD	metal-organic chemical vapour deposition
MS	mass spectroscopy
mmol	millimole
m.p	melting point
NMR	nuclear magnetic resonance
Ph	phenyl group
ppm	part per million
SEM	scanning electron microscopy
AFM	atomic force microscopy
TEM	transmission electron microscopy
SSP	single source precursor
TGA	thermogravimetric analysis
UV/Vis	ultra-violet/visible
XRD	X-ray diffraction

CHAPTER 1

INTRODUCTION

Introduction

1.1. Energy

Energy is an integral part of human development. Energy from natural resources has been the main source to cater for development needs. Fossil fuels have been of special interest in this regard and the 20th century may rightly be described as 'the century of man's love for oil'. Even in the 21st century, energy mix of almost all the countries is dominated by fossil fuels. Nuclear energy has emerged as another leading energy source in lesser developed countries. Different factors mainly increasing growth of industrial activity in developing countries and subsequent change in lifestyle of people have resulted in significant increase in energy consumption, leading to drastic changes in global energy supply trends. Therefore, the current energy situation is now considered as environmentally, economically and socially unsustainable and an 'Energy Revolution' is urgently needed. Major focus of the future energy planning would lie on securing the supply of dependable and cost effective energy. Another important area in this regard would be transformation of world's energy mix to an efficient, low carbon emission and environmentally benign system.[1]

Energy consumption is more in developed countries than in developing or underdeveloped countries.[2] Economists have identified a positive correlation between Human Development Index (HDI) and the energy consumption.[3] Similarly, correlation between the gross domestic product (GDP) of a country and its energy consumption has been identified by Arunachalam and Fleischer.[4] This highlights that more development would result in a significant increase in energy consumption in developing countries. With the orld's population already exceeding 6 billion, it may rightly be anticipated that the energy requirements of the world might dominate the politics of 21st century.

Currently employed power production technologies are based on fossil fuels (oil, coal or natural gas), nuclear reactors and hydroelectric power projects. Emerging technologies like solar thermal and solar photovoltaics, wind power, biofuels and tidal energy have demonstrated significant potential as well. At present, electricity all over the world is mainly produced by burning natural gas, oil and coal.[5] Nuclear power production is the second leading source of electricity generation in technologically advanced countries.[6] Hydroelectric

power is another attractive electricity generation technology, especially in developing countries. However, environmental footprints, varying in severity, are associated with all types of energy technologies. These include emission of greenhouse gases especially CO_2 in the atmosphere, production of both long-lived and short lived radioactive isotopes from nuclear reactors and drastic influence on river ecosystem and fisheries as well as dislocation and disruptions caused by large hydropower projects.[7,8]

Besides these environmental aspects, other factors like finite availability and non-equitable distribution of fossil fuels, and issues related to energy security necessitate development of viable, clean, efficient and environmentally benign power generation sources and technologies. Leading options may include:

(a) Wind Energy
(b) Solar Thermal Energy
(c) Solar Photovoltaics
(d) Geothermal
(e) Biomass
(f) Ocean Energy

The work described in this thesis deals with solar photovoltaic materials. Therefore, the following sections give some background to these types of materials.

1.2. Solar energy

The sun is considered as the most abundant source of energy for the inhabitants of earth. Solar energy striking the earth issurface in one hour is estimated to be more than the total energy consumed on the planet in a year.[9] Another calculation suggests that the solar energy falling on the earth in 30 sunny days is equivalent to the energy produced from all fossil fuels on earth, either consumed or unused. There are also some issues which limit the use of solar energy. But despite all limitations, technical potential for converting sunlight into heat or electricity is approximately calculated as about four times of the total energy consumption on earth.[10] Photovoltaics (PV), therefore have the potential to ensure the revolutionary transformation of present global energy

situation to a reliable and sustainable energy supply system for the 21st century. It may provide environmentally benign energy with no emissions and would enhance energy security because of its global availability. Augmented by improved energy efficiency practices and other renewable energy technologies, photovoltaics may be envisioned as a key energy technology in the forthcoming decades.

Solar photovoltaics is the process which deals with the conversion of solar energy directly into usable electric power by employing solar cells. E. Becquerel discovered photovoltaic effect in 1839. However, more than 100 years later, Chapin, Pearson and Fuller of Bell Telephone Laboratories for the first time demonstrated crystalline silicon based viable solar electricity production in 1954.[11] This may be regarded as the beginning of commercial photovoltaics. Since then a steady and substantial growth in this technology has been observed mainly due to government subsidies and incentives. However, during the past two decades a booming growth in the photovoltaic industry occurred because of economic volatility due to an increase in oil prices worldwide and raising awareness about environmental impacts of conventional energy technologies.

Despite all this progress and the inherent potential of photovoltaics, the current share of photovoltaics in global energy production is very low; the cost per Watt-peak of electricity produced being the most important daunting factor. The price of standard PV modules is currently around 3 €/W, which is significantly higher than conventional electricity generation technologies. However, different studies have established that this cost may potentially be lowered to 2 €/W by 2010, 1 €/watt till 2020 and till the end of 2030 further cost reduction to the level of 0.5 €/W is expected. Even after 2030, a further price reduction is also expected.[12] Major factors contributing to this cost reduction are continued market growth, superior production strategies, improvement in solar module efficiencies and technological developments in this area.[13]

1.3 Solar photovoltaic technologies

A PV system consists of solar cells and these cells arrayed together constitute a solar module for generating the electricity. Other important components include the cabling, battery, charge controller, DC/AC inverter and

other support components. The most important component of the solar cell is the light absorbing semiconductor material which absorbs photons of light to produce electron and hole carriers via the photovoltaic effect. Current PV market relies on various technologies employing wafer based silicon and some thin film technologies, which may be categorized as first generation and second generation technologies. Figure 1.1 represents current share of various PV technologies in global PV market.

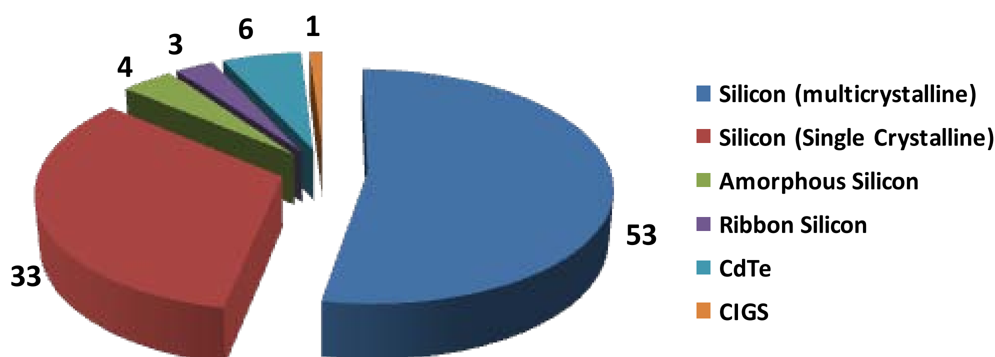

Figure 1.1 Current market share of various PV technologies

First generation PV technologies are based on silicon wafers having maximum power conversion efficiencies of ~ 25% and ~ 13-15.5%, for single crystalline and multi-crystalline silicon wafer based cells, respectively.[14,15] Around half of the cost involved in first generation PV technologies is the material cost for silicon wafers as it requires high quality feed stock and much silicon is lost during processing. Furthermore, above 30% increase in PV manufacturing during recent years has now resulted in more excessive demand for silicon feedstock than supplies, thereby causing significant increase of its costs. Therefore, it is likely that cost reduction trend for first generation PV technologies will reach its limits before they reach full-cost competiveness.[16]

Second generation PV technologies are single junction devices that offer the key advantage of reduced material use and thus reduced associated costs, while still maintaining the efficiencies comparable or better than first generation PV technologies. In this approach, thin layers of semiconductors like amorphous, polycrystalline, microcrystalline or nanocrystalline silicon, cadmium telluride (CdTe), chalcopyrite compound semiconductors like copper indium

diselenide (CIS) or copper indium gallium diselenide (CIGS) are deposited on less costly substrates like glass. Semiconductor materials used in these technologies have high solar optical absorption coefficients (greater than 10^5/cm). Therefore, absorber film thickness is typically less than a micron and 100-1000 times lesser materials than silicon wafers-based PV are required. Besides, it makes it possible to manufacture thin film solar cell modules as expanded units. Large scale production, thus offers even better economy of scales.[17,18]

Efficiencies obtained so far for second generation PV technologies are low. Highest stabilized efficiencies for amorphous silicon, micro- or nanocrystalline silicon and polycrystalline silicon are ~ 9.5 %,[19] 13%,[20] and 10.4%,[21] respectively. Similarly, maximum power conversion efficiencies of ~ 16.7%,[22] and 19.4% [23] have been reported for cadmium telluride (CdTe) and copper indium gallium diselenide, $CuIn_{(1-x)}Ga_xSe_2$ (CIGS) based solar cells.

Third generation photovoltaics covers a range of budding devices, upstarts, and emerging ideas that have joined the race for achieving requisite performance and cost targets for delivering 15-30 terawatts of solar power by mid-century.[24] No clear definition of the term third generation exists. Whereas second generation technologies might be competing or even surpassing silicon wafer based technologies in the near term, third generation technologies have yet to undergo a marathon struggle to demonstrate their applicability and bring them to commercialization.[25] Notable development has been made, especially in tandem or multijunction devices, dye-sensitized solar cells, quantum dot solar cells and organic solar cells with an efficiency of 32 ± 1.5 has already been reported for GaInP/GaAs/Ge multi-junction devices under global AM 1.5 spectrum.[26] Even higher efficiencies of ~ 40% have been demonstrated for multijunction or tandem cells with concentrators.

1.4 Background Semiconductor Theory

An insight into properties at an atomic level is required in order to fully understand the electronic properties of semiconductors.[27-29] Band theory represents a common approach utilized to explain the fundamental properties of semiconductors. This originates from molecular orbital theory in which the linear combination of atomic orbitals approximation is used to describe the formation

of molecular orbitals on the basis of interaction of wavefunctions. In a simple case of hydrogen, the single *s* electron wavefunctions of two hydrogen atoms (commonly represented as χ_A and χ_B) interact in all possible linear combinations to generate a bonding and antibonding orbital (ψ_1 and ψ_2 respectively):

$$\psi_1 = \chi_A + \chi_B$$

$$\psi_2 = \chi_A - \chi_B$$

The molecular orbitals thus formed are having differing energy levels than the corresponding atomic *s* orbitals. The bonding orbitals have lower energy than the original atomic energy levels while the antibonding orbitals are higher in energy than the original atomic energy levels. The two *s* electrons from hydrogen atoms A and B in this case occupy the lowest possible energy configuration therefore populating the bonding orbital whereas the antibonding orbitals remain unoccupied.

In a similar way, bound electrons in an individual atom have discrete energy levels separated by forbidden energy regions while in solids, the discrete levels broaden to form allowed bands which are separated by bandgaps. Band theory can be used to describe these continuous bands of energy levels displayed in solids. This continuous band is caused by the negligible energy gap between the molecular orbitals arising from the interaction of wavefunctions of atomic orbitals. It is possible for the energy states within each band to be occupied by pairs of electrons (according to the Pauli's exclusion principle). Electrons will reside in the lowest energy levels at absolute zero, commonly called the valence band while the higher energy levels termed as the conduction band remain unoccupied at absolute zero temperature. Electrons are unable to occupy the region in between these energy bands and this region is termed as the band gap (E_g). Absorption of sufficient energy, results in transition of an electron from the valence band that crosses the band gap and shifts to the conduction band. The energy required for this transition is characteristic of the particular material in question and these unique band gaps, are usually measured in electron-volts (eV). For conduction to be possible a partially filled band is required (as a net motion of electrons is required for

conduction). More electrons present in the conduction band would mean that the material would be more conductive.

1.4.1 Differences between semiconductors, insulators and conductors

The difference in the band gap makes a material either an insulator or semiconductor. Materials with larger band gaps, 9 eV or greater are insulators whereas semiconductors usually have a band gap in the region 0.5-2.0 eV. Therefore in the insulator, no transition of electrons from the valence band to the conduction band is feasible, no matter how much external energy is applied to make this transfer. This therefore means no conduction is possible in these types of materials, as electrons are not likely to populate a partially occupied conduction band, and hence the term "insulator" is used for such materials. The opposite is true for a metallic conductor, where the valence and the conduction bands overlap each other meaning there is essentially no band gap present. This means that even at low temperatures, there is continuous transfer of electrons from the valence band to the conduction band. Therefore, the electrons in metallic conductors have sufficient freedom to move about the lattice.

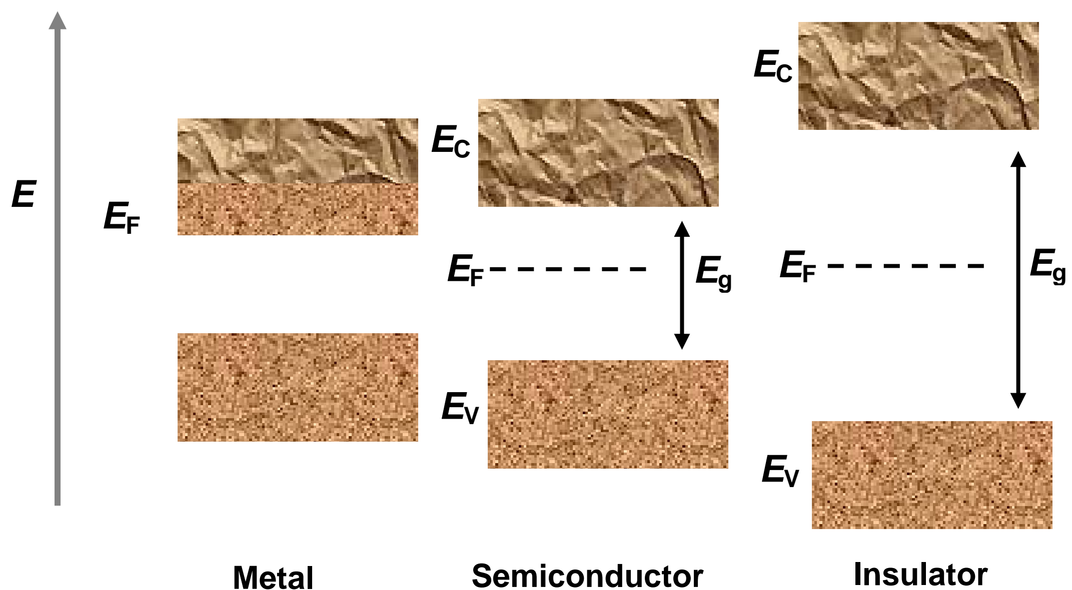

Figure 1.2 Schematic illustration of typical band diagrams for a metal, an intrinsic semiconductor and an insulator. Ev represents the energy associated with valence band while Ec represents the energy associated with the conduction band.

Semiconductors possess a band structure that is intermediate between that of insulators and metallic conductors. At absolute zero temperature, all electrons of the semiconductor material occupy the lower energy valence band while conduction band remains unoccupied. However, at finite temperatures, the band gap is significant but is well below that of insulators. At low temperature, electrons mostly occupy the valence band with little or no electrons in the conduction band. Therefore at low temperature there is little, if any, conduction. While at higher temperature, electrons have enough energy to get promoted to the conduction band via the band gap thus making the conduction possible.

For molecules, the amount of molecules inhabiting a particular energy level at a particular temperature can be calculated using the Boltzmann distribution, but in the case of electrons in semiconductors, Fermi-Dirac distribution function is used to calculate occupation statistics of energy levels. This means that Fermi-Dirac distribution gives the probability of an electron occupying a particular energy band in semiconductors at a given temperature:

$$f(E) = \frac{1}{1 + \exp[(E-E_f)/K_bT]}$$

This expression suggests that an exponential relationship exists between the temperature and the probability of occupancy. The chances of electrons being promoted to the conduction band increase significantly with an increase in the temperature (i.e. increases the chances of electrons appearing above the Fermi level). Therefore, this expression clearly suggests an increase in conductivity of semiconductors with a rise in temperature. Theoretical curves of the Fermi-Dirac distribution function given in Figure 1.3 clearly demonstrate this phenomenon. Figure 1.4 shows part of the photoelectron spectrum of ruthenium at three different temperatures, with the theoretical curves of the Fermi-Dirac distribution function superimposed (as the smooth line). A very strong correlation between the theoretical curves and experimental curves is clearly evident from this figure.

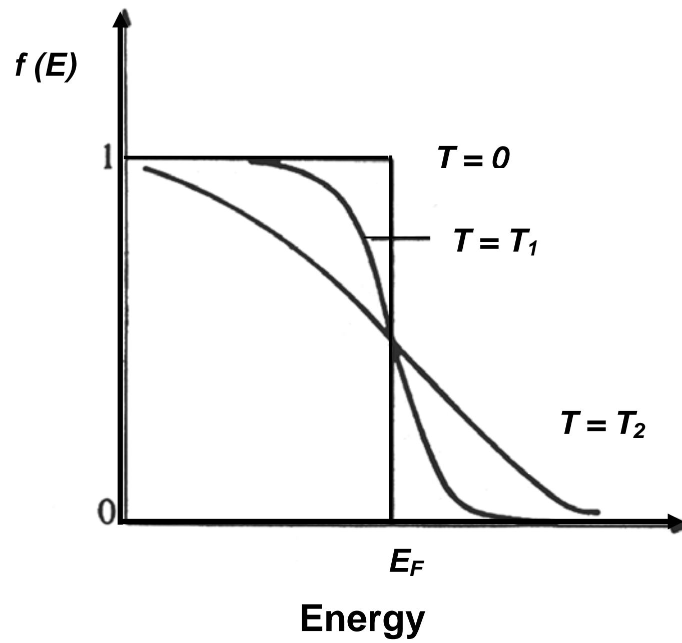

Figure 1.3 Fermi-Dirac distribution function. Theoretical curves at 0 K (T=0), and two higher temperatures where (T_2>T_1>0)

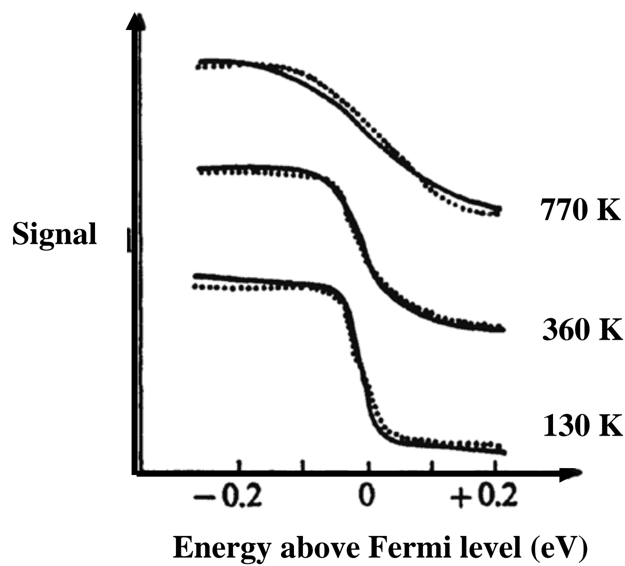

Figure 1.4 Part of the photoelectron spectrum of metallic ruthenium at three different temperatures. The smooth line is theoretical and the dotted experimental (G. K. L. Cranstoun, R. G. Egdell, M. D. Hill and R. Samson, *Journal of Electron Spectroscopy and Related Phenomena*, 1984, **33(1)**, 23.)

1.4.2 Direct and Indirect bandgap Semiconductors

An important factor determining the efficiency of absorption of light photons in a semiconductor absorber and electron-hole pairs generation is known as the absorption coefficient. When transitions of electrons from the valence band to the conduction band occur in semiconductors, a change in crystal momentum (k, wavevector) may or may not occur. This occurrence of change in k, wavevector depends on the possible route available involving lowest energy transition. In a typical absorption process, an electron is excited from the valence band to the conduction band upon absorption of a photon. This absorption process occurs with conservation of both the energy and the momentum. The momentum of photon being so small in comparison with the momentum of crystal, electron's momentum should essentially be conserved in the absorption process. If the minima of the conduction band and the maxima of the valence band occur at the same value of the wavevector k (Figure 1.5a) in a transition, such transitions are called direct transitions, and the material is termed a direct band gap semiconductor.

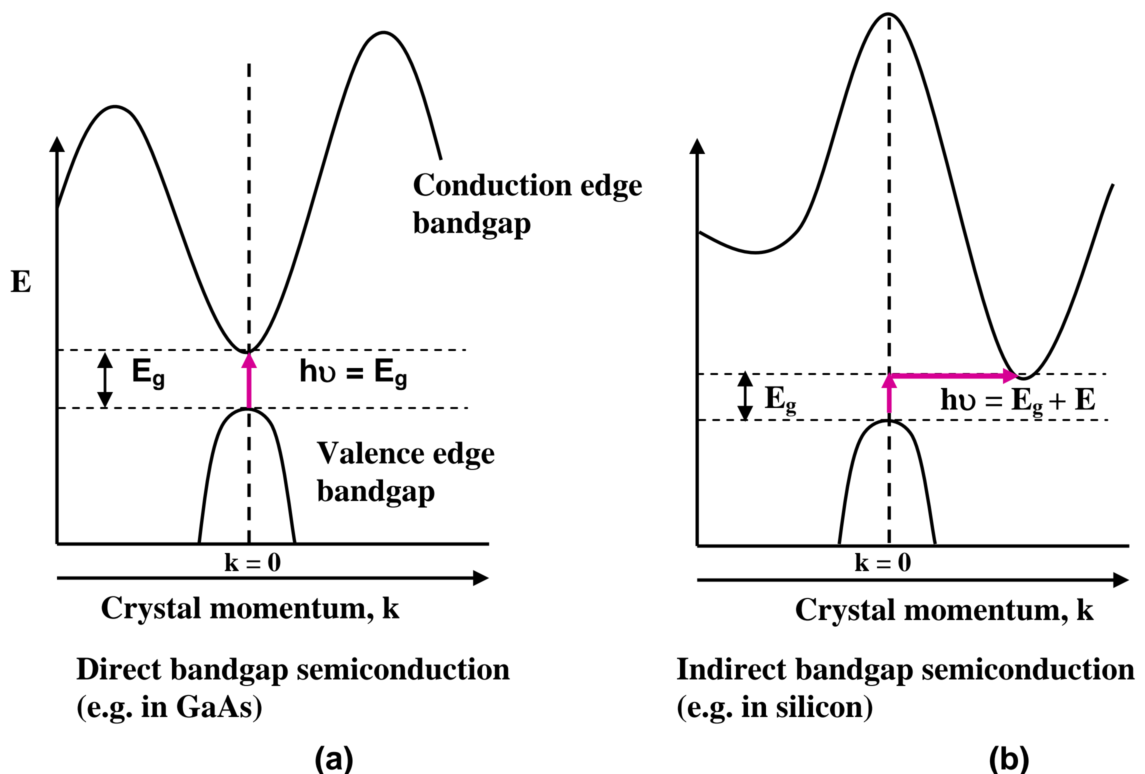

Figure 1.5 Energy band diagram for direct and indirect semiconductors

Transitions are referred to as indirect transitions if they involve a situation in which band extrema occur at different values of wavevector k, (Figure 1.5b) and accordingly the material is referred to as an indirect band gap semiconductor. Another particle i.e. a phonon is necessary for momentum conservation in such transitions. As compared to direct transitions, the probability for indirect transitions is substantially lower. Therefore, relatively weaker fundamental absorption generally occurs in indirect band gap materials as compared to direct band gap materials. This means that before absorption, a photon is required to travel a long distance into the material thereby limiting the chances of such transitions. Therefore, direct band gap materials have much higher probability of the absorption of photons and therefore possess higher absorption coefficients than indirect band gap materials.[30] Direct transitions, may have values of absorption coefficients varying from 10^4 to 10^5 cm^{-1} while the same may vary from 10 to 10^3 cm^{-1} for indirect transitions.

1.4.3 Intrinsic Semiconductors

An ideal intrinsic semiconductor is an impurity free semiconductor having no lattice defects in the crystal (e.g. pure silicon). Such semiconducting materials show increased conductivity with increased temperature. An intrinsic semiconductor at T = 0 K, has completely filled valence band energy states while in the conduction band, there are all empty energy states. The Fermi energy must, therefore, be somewhere between E_c and E_v. With the rise in temperature above 0 K, the valence electrons gain thermal energy. As soon as sufficient energy level is achieved, few electrons in the valence band traverse the bandgap and are promoted to the conduction band. Such transition results in generation of an empty state or hole in the valence band.

In an intrinsic semiconductor, thermal energy plays a key role in generating electrons and holes in pairs; thus an equal number of electrons in the conduction band and holes in the valence band are created. The resulting conduction is the result of motion of electrons as well as positively charged holes in the conduction band. Effectively, this can be seen as the two bands now being more partially filled than they were before, hence allowing more conduction.

At any given temperature:

$$n(T) = p(T) = n_i(T)$$

Where n(T) is the number of electrons in the conduction band, p(T) is the number of holes in the valence band, and n_i is the intrinsic free carrier concentration. Examples of elemental intrinsic semiconductors are silicon and germanium whereas compound intrinsic semiconductors are gallium arsenide, indium phosphide and zinc sulfide.

1.4.4 Extrinsic Semiconductors

Though intrinsic semiconductors are of remarkable interest in academic research, the true strength of semiconductors is manifested by extrinsic semiconducting materials. All commercially available semiconductors are extrinsic which are different from intrinsic semiconductors only due to the presence of intentionally added impurity which changes whole scenario in context of the electronic properties of the material. This process of introducing controlled quantity of impurity is known as doping. There are two types of doping and an extrinsic semiconductor will either be electron donor (n type) or electron acceptor (p type), thus the resulting material will be electron rich or electron deficient. At room temperature relatively high conductivities may be obtained for extrinsic semiconductors as the doping significantly changes the band structure. Therefore, extrinsic semiconductors can be fabricated in a form, useable in electronic devices at ambient temperatures.

In a semiconductor, doping causes an electronic discontinuity within the lattice which is compensated by the induction of additional energy levels within the band gap. Figure 1.6 represents the band diagram for extrinsic semiconductors of n-type and p-type. If the semiconducting material is doped with an electron donor atom like phosphorus or arsenic, the non-bonding electron in dopant atom is loosely held by weak electrostatic forces. Therefore, at finite temperatures (even at room temperature), thermal energy is sufficient enough to cause transition of electrons to the conduction band, from the valence band. Now a conduction band electron is able to move within a crystal generating a current, while the positive ion remains fixed in the crystal. An electron is therefore donated by such an impurity atom to the conduction band

and hence it is called as a donor impurity. It causes an increased number of free electrons in the conduction band than the number of holes present in the

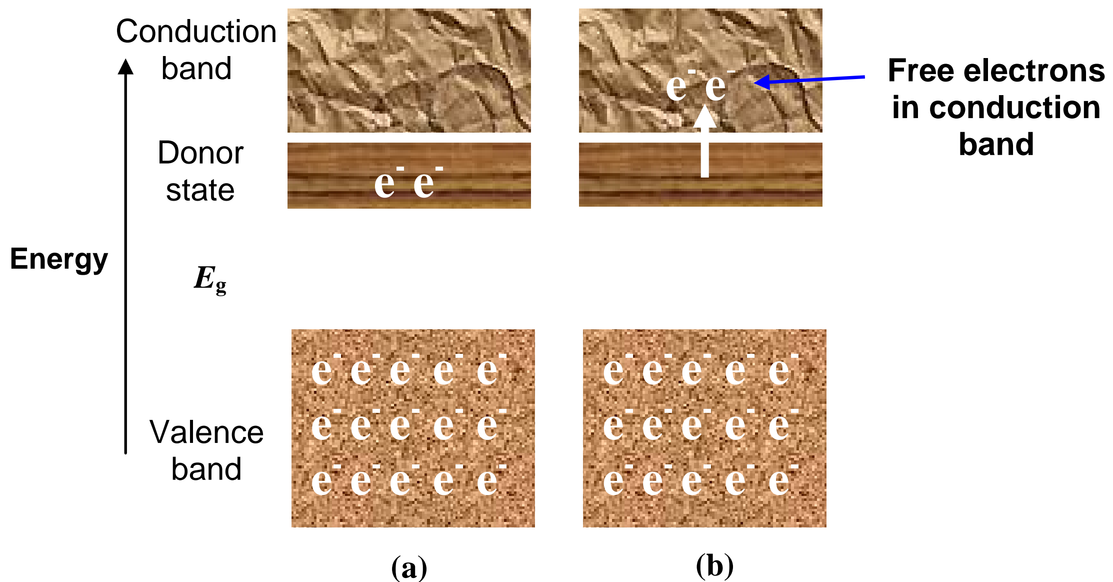

Figure 1.6 Electron Diagram diagrams representing (a) a donor impurity located within the band gap and just below the conduction band; (b) Subsequent excitation of the electron from the band gap to the conduction band.

valence bond. Such a material is termed as *n-type* extrinsic semiconductor. Electrons by virtue of their concentration are majority carriers in n-type materials whereas the holes are minority carriers. The Fermi level, for *n-type* semiconductors, is raised within the bandgap i.e. near to the conduction band. The fermi level's exact position would however, be a function of both the temperature and the donor concentration.

When the semiconductor atom is substituted by an impurity containing one electron less than the semiconductor atom, this impurity used for doping the semiconductor is called an acceptor (see figure 1.7). Such an impurity introduces an energy level within the bandgap, located near the top of the valence band as the fermi level. Thermal excitation of an electron from the valence band into the impurity acceptor level creates a positively charged hole. No free electron is created in either the impurity level or in the conduction band. It is noteworthy that the mobile holes are created in valence bands, while the thermally excited electrons are bound to the acceptor atoms. Such kinds of extrinsic semiconductors are commonly termed as *p-type* semiconducting

materials in which majority carriers are the holes and electrons may be called the minority carriers. The acceptor levels in p-type materials do not display band-like qualities and electrons cannot move around in them (i.e. they are discrete energy levels). Movement of the holes in the valence band contributes to conduction of the material in this case. Movement of the holes in valence band is responsible for conduction abilities of the semiconducting material. A good example of such materials is silicon doped with precisely controlled amount of gallium.

This may be summarized as in the case of intrinsic semiconductors, the band structure and hence electrical properties solely depend on inherent properties of the pure material and equal concentrations of electrons and holes exist in the material, whereas in the case of extrinsic semiconductors, impurity or dopant alters the band structure and hence dictates the electrical properties of the material. Electron-hole concentrations are not equal in the case of extrinsic semiconductors and depend on the donor or acceptor properties of the dopant used.

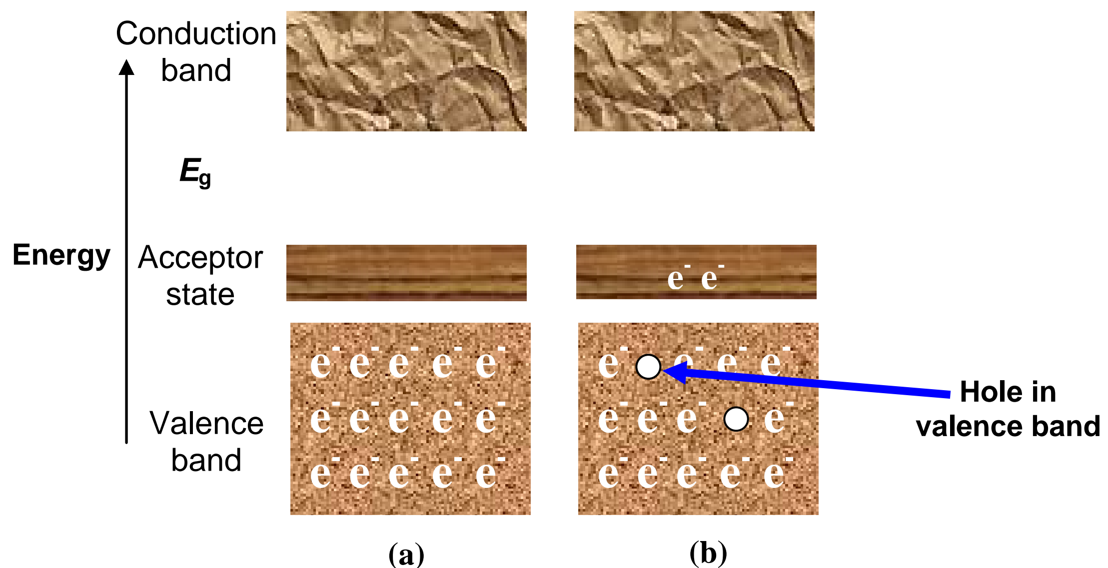

Figure 1.7 Electron band structure for (a) an acceptor impurity level, located within the band gap and lying just above the valence band; (b) excitation of an electron into the acceptor level, leaving behind a positive hole in the valence band.

1.5 Thin film deposition techniques

During the past two decades, the synthesis of nanomaterials with precisely controlled size and shape has attracted a great deal of research interest and new synthetic routes for the synthesis of low-dimensional nanomaterials and complex hetero-nanostructures have been developed. Thin film deposition techniques such as molecular beam epitaxy (MBE) and chemical vapor deposition (CVD) have paved the path to remarkable achievements in the fabrication of low dimensional semiconductor materials. MBE involves base pressure at about 10^{-11} Torr; hence it is regarded as an ultrahigh vacuum (UHV) method while CVD requires relatively lower vacuums of about 10^{-2} Torr or greater. A CVD process that employs metal-organic compounds for epitaxial growth of materials is termed as metal-organic chemical vapor deposition (MOCVD) which has been extensively employed for the deposition of structures like superlattices and quantum wells (QWs) having requisite properties (e.g. band-gap engineering).[31] Other commonly employed thin-film deposition methods include chemical bath deposition (CBD), evaporation, sputtering and spin-coating.

Synthetic approaches to semiconducting nanoparticles have been reviewed in many literature reports.[32] In the present work, aerosol-assisted chemical vapor deposition was utilized for the deposition of thin films of semiconductor materials, whereas a colloidal approach involving thermolysis of precursor was exploited to synthesize semiconductor quantum dots (QDs). Next section of the thesis will therefore focus on these techniques.

1.5.1 Chemical Vapor Deposition

Earlier experiments conducted by Van Arkel and De Boer may be marked as the origin of chemical vapor deposition and during last few decades, activity in this field has increased dramatically. CVD involves the deposition of solid thin films on a selected substrate from the precursors in vapor form. Chemical reaction, mostly decomposition of volatile precursor material occurs on the substrate to form a solid deposit. Metal organic chemical vapor deposition (MOCVD) including aerosol-assisted chemical vapor deposition (AACVD) and low-pressure chemical vapor deposition (LP-CVD), photo-assisted chemical vapor deposition (PACVD), plasma-enhanced chemical vapor

deposition (PECVD), and laser-assisted chemical vapor deposition (LACVD) are various variants to the conventional CVD process. Different factors such as availability of the process, nature of the precursor to be used, desired features of the deposited material dictate the choice of process for undertaking deposition experiments.

1.5.2 Metal organic chemical vapor deposition

MOCVD is a process employing the pyrolysis of vapor-phase mixture of various chemical reagents (i.e., precursors) onto substrate to form thin solid films of materials. Deposited materials may be as diverse as metals, semiconductors, and insulators. Currently, the primary use of MOCVD is for deposition of crystalline thin films of semiconductors and related materials. The MOCVD technology has advanced remarkably since the first report of the growth of semiconductor epitaxial films by H. M. Manasevit in 1968. The first high-performance semiconductor devices realized by MOCVD were solar cells and AlGaAs/GaAs injection lasers reported by R. D. Dupuis *et al.* in 1977.[33] In the past forty years, MOCVD has been extensively utilized for the deposition of a wide range of semiconductor materials. It is now considered as the leading technology worldwide for the commercial production of solar cells, light-emitting diodes (LEDs), photodetectors, injection lasers, quantum-well lasers, hetero-junction bipolar transistors and various other electronic and optoelectronic devices.[34]

1.5.3 Aerosol-Assisted Chemical Vapor Deposition (AACVD)

The dilemma of finding suitable chemical precursors for optimal delivery, especially while attempting the deposition of multi-component products, limits the usefulness of conventional CVD techniques. The major hindrances to the application of CVD include the unfavourable volatility of precursors and the difficulty in precisely controlling stoichiometry of the deposits. AACVD method circumvents these limitations as it utilizes aerosols for delivery of the precursors, in a stream of inert carrier gases. It is not necessary for the chemical precursors to be volatile for AACVD, but they should be merely soluble in any solvent so that their aerosol can be obtained by using any suitable technique like ultrasonic modulation. AACVD is an especially useful

option to deposit coatings, films, and other related structures from the involatile or thermally unstable precursors. As AACVD can be carried out using less volatile precursors of even poor thermal stability, high-class CVD products can be produced at a lower cost by employing this method. Key advantages offered by the AACVD, in comparison with other CVD techniques, may be enumerated as follows:

- Wider availability and broader choice of chemical precursors for obtaining high quality CVD structures at lower cost;
- Simple mass transport of precursors to the reactor as aerosols of precursor generated by simple means;
- Precise control over deposition rate through adjusting the mass transport of precursors;
- More flexible reaction environment ranging from low pressure to atmospheric pressure;
- Simplified growth/deposition of multi-component products with strict control over product stoichiometry.

In a typical procedure, the precursor is fully dissolved in a solvent, usually toluene, tetrahydrofuran (THF) or acetonitrile. However, the relatively high boiling point of toluene makes it the preferred choice over other two solvents. A carefully controlled stream of carrier gas (usually argon or nitrogen) flows through the precursor/solvent flask, which is placed in an ultrasonic modulator to generate micron-sized aerosol droplets. These aerosols are transported by the carrier gas into the heated reactor, where the precursor is decomposed and produces a thin film of material. The solvent vapors and volatile by-products are then carried out into a liquid nitrogen trap.

AACVD technique also has a few disadvantages in comparison with other techniques in that it is limited by the solubility of precursor in a solvent, i.e. if the precursor is not soluble in a suitable solvent, then it will not be possible to use AACVD to grow thin films using that precursor. Also the process involves a large volume of the solvent which means that large amounts of flammable vapor are present in the reactor chamber that could potentially ignite. An efficient exhaust in fume cupboard is therefore an essential pre-requisite for carrying out an AACVD experiment.

1.6 Nanoparticles

Semiconducting nanoparticles have been the area of immense research interest during the previous decade, the main reason being their novel catalytic and optoelectronic properties. Substantial research efforts have been focused in the synthesis and characterization of nanosized semiconductor particles (in the order of 2-100 nm size). Many devices like LEDs, solar cells, photodetectors and lasers have been fabricated exploiting the unique properties of semiconducting nanoparticles. Furthermore, nanoparticles (quantum dots) have been successfully used in biological labelling and biological imaging.

The properties of semiconductor nanoparticles differ considerably from their macro-crystalline bulk counterparts, chiefly because of two fundamental factors (see figure 1.8). Firstly, the particles in nano-dimension possess a larger surface to volume ratio, therefore surface properties become considerably important in this size regime. Secondly, nanoparticles possess larger band gap energies than corresponding bulk materials because of quantum confinement effects. In semiconductors, promotion of an electron to the conduction band

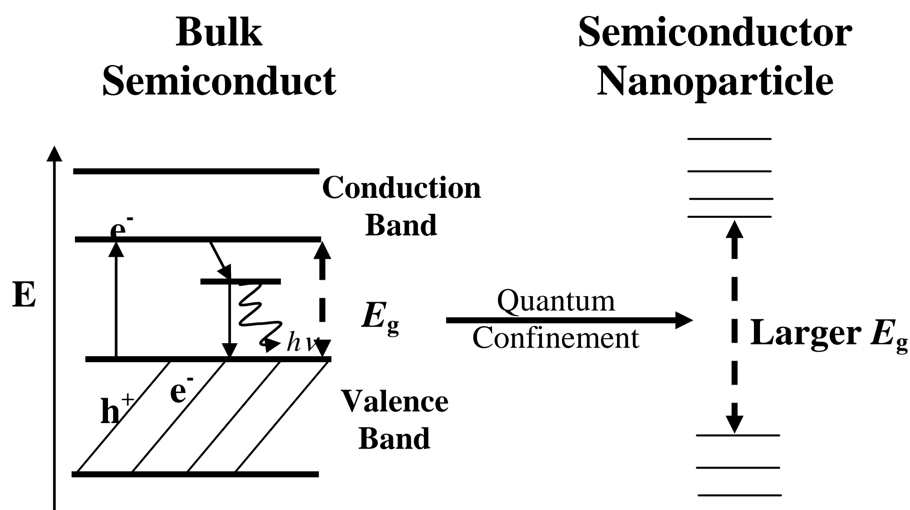

Figure 1.8 Diagram showing the larger band gap in nanoparticles in comparison to bulk semiconductors

results in a hole in the valence band where both electrons and holes are considered as a charge carrier. When they approach each other, they form an exciton, delocalized within the crystal lattice, where the Bohr exciton radius is

effectively the distance between the electron and the hole. Quantum confinement effect arises as an outcome of the confinement of an ‘electron in a box’ as the size of the particle becomes smaller than Bohr exciton radius, thus creating discrete energy levels in contrast to a continuous band as found in bulk materials. Additionally, coulombic interactions between the electrons and holes result in higher kinetic energy states than corresponding bulk semiconductors, therefore manifesting a blue shift in optical spectra.

This phenomenon has got special significance as it allows tunability of optical and electronic properties of the nanoparticles by carefully controlling the size of nanoparticles, thus making it possible to obtain materials with better suitability for a particular opto-electronic application. Light emitting diodes (LED), photovoltaic cells and non-linear-optics (NLO) are a few examples of the device applications making beneficial use of this effect.

1.6.1 Preparation techniques for nanoparticles

Synthetic strategies used for nanoparticles have considerable impact on certain features of the product and play a crucial role in their successful use in device applications. Characteristics ideally desired in the synthesized nanoparticles include a fairly narrow size distribution, high degree of crystallinity, appropriate surface layer composition and higher luminescence quantum yield. Synthetic methods should be readily available, reproducible and those involving reagents with low toxicity. Other important applied aspect to be considered include final production cost, reaction duration and the prospects for up-scaling the reaction *etc.* Synthesis techniques for semiconducting nanoparticles have been reviewed in the current literature. Various strategies employed for the synthesis of semiconducting nanoparticles include gas phase synthesis,[35-37] colloidal approaches,[38-40] solvothermal synthesis,[41,42] synthesis in confined matrices,[43-45] and methods involving metal-organic routes to nanoparticles.

The colloidal route involves using controlled precipitation reactions which yield dilute suspensions of colloidal particles. Bawendi *et al.* developed this technique for the synthesis of CdSe, CdS, and CdTe nanoparticles.[46] Solutions of dimethylcadmium (Me_2Cd) and TOPSe (in case of CdSe for example) in trioctylphosphine (TOP) were injected into TOPO at high temperature (250°C

for CdSe). Decomposition of the precursors yielded TOPO capped nanoparticles. To avoid use of hazardous precursors (e.g. dimethylcadmium in this case), Trindade and O'Brien modified this approach by using single source precursors, thus devising safer and better controllable methodology.[47-49] CdSe CdS, PbS, and PbSe nanoparticles capped with TOPO have been successfully produced by this method.

1.7 Solar cells based on nanocrystals

Current developments in the colloidal synthesis of nanomaterials have opened up promising avenues in research for the development of low-cost next generation solar cells with higher power conversion efficiency. Development of safe, simple and straightforward techniques for solution phase synthesis of nanoparticles have boosted the development, fabrication and even commercialization of new photovoltaic devices.[50] These techniques have demonstrated significant potential for yielding fairly monodispersed, well passivated, non-aggregated semiconductor nanocrystals. Additionally, high quality nanomaterials with superior optoelectronic properties are being explored to develop photovolatic devices. In order to lower the fabrication cost of the light absorbing layer of the solar cells, one approach involves using colloidal semiconductor nanocrystals as photo-absorber 'ink'. Either electronically coupled arrays of nanocrystal are cast onto a substrate or bulk semiconductor layers of nanocrystals are developed by sintering and thus a desired bandgap of the absorber material is obtained for harvesting the solar radiations spectrum in an efficient and effective manner.[51]

Although the sintered and nanocrystals array devices are less than 37% efficient in power conversion (i.e. the Shockley–Queisser limit). Solar cells and modules can be produced at significantly lower cost. In fact, this approach yields more cost effective solar cells and solar modules than corresponding vacuum based methods for photoabsorber layer deposition. Discovery of "carrier multiplication" or "multiple exciton generation" in some nanocrystals may give quantum yields greater than 100%. Research efforts are underway to develop solar photovoltaic devices based on these nanoparticles and it is anticipated that such devices may exceed the Shockley–Queisser limit, thus giving rise to a new generation of commercially viable photovoltaic technology.

The phenomenon of multiple exciton generation has been studied in colloidal quantum dots of low band-gap materials (0.6– 1.1 eV) like PbS, PbSe, InAs *etc.*[52-54]

Vacuum based deposition processes, high processing temperatures, longer processing times and expansive precursors as well as substrate materials increase the manufacturing cost of solar cells and solar modules. Consequently, this cost can be significantly decreased by the utilization of solution-phase processes, lower processing temperatures, shorter processing time and cheaper precursors as well as substrates that may permit optimal scale up like 'roll to roll' manufacturing process.[55] The bandgap value of the nanocrystal array or sintered nanocrystal layer is the issue of prime importance in selection of absorber material for solar cells and modules. This value ranges from 1.0 to 1.6 eV for non-MEG solar devices. This is obtained for large nanocrystals that have only weak quantum confinement effects as in the case of CdTe, Cu_2S, $CuInSe_2$, CIGS and Si nanocrystals. Due to quantum confinement effects in nanocrystals, the bandgap of suspended colloidal nanocrystals may be tuned by carefully controlling the size of nanocrystal. Recently, well established synthetic procedures have been developed for the nanocrystals of I–III–VI_2 semiconductor $CuInSe_2$ and the I_2–VI semiconductor Cu_2S, for their applications as solar photoabsorber materials. $CuInSe_2$ possesses direct bandgap of 1.04 eV which can be further broadened by incorporation of Ga leading to formation of $CuInGaSe_2$. In this way, bandgap can be tuned from 1.04 eV to 1.68 eV by controlled substitution of Ga for In atoms.[56] The factors like higher quantum yield, oxidation stability, stability of the heterojunction, cost incurred on the material and synthetic process, abundant availability of the material, and prospective health and environmental hazards are the factors which must be taken into consideration while choosing semiconductor nanocrystals for photovoltaic applications. Some of the materials like PbTe nanocrystals are extremely air sensitive. This limits their practical application due to substantial degradation of these materials out of an oxygen-free glove box. In contrast, $CuInSe_2$ nanocrystals based devices are fairly stable. Even non-encapsulated devices exposed to humid air remain stable for years. It is also considered that toxicity associated with solar devices based on Cd or Pb has significantly hindered their large scale commercialization, whereas devices

based on $CuInSe_2$ are a better choice as they possess very low toxicity profile and are environmentally benign.

Recently, a new synthetic approach for Cu_2S nanocrystals and a low temperature processing route to photovoltaic devices has been reported.[57] In an oxygen-free environment, the devices having 1.6 % efficiency have shown stability for over 4 months. Amongst solar cells based on nanocrystals, those having chalcopyrite I–III–VI_2 family of semiconductor nanocrystals have shown the highest efficiency so far. These semiconductor materials may be generally represented by formula $Cu(In_{1-x}Ga_x)(Se_{1-y}S_y)_2$. State-of-the-art thin-film bulk devices have been made by a process that involves co-evaporation of Cu, In, and Ga metals. However, this fabrication technology has many limitations. Being too costly, it is not suitable for wide range applications and cannot be scaled up. Many efforts have been made to evolve non-vacuum based methods for fabrication of CIGS devices. Solar cells having ~ 13% efficiency have been developed by some of these approaches.[58-60] However, many of these approaches suffer the drawbacks that they either lead to formation of binary structures or additional phases are formed and precise control over structure, morphology and composition becomes somewhat difficult. Preparation of stoichiometric nanocrystals with required chemical composition and structure, prior to film formation may solve this problem. Stoichiometric synthesis of chalcopyrite or sphalerite $CuInSe_2$ from elemental Se and chloride precursors by gradual heating has been reported by Guo *et al.*[61] It was further demonstrated that controlled incorporation of Ga yielding stoichiometric $CuInGaSe_2$ nanocrystals and CuGaSe2 nanocrystals was also feasible. Very similar synthesis strategies for $CuInSe_2$ and $CuInGaSe_2$ nanocrystals have also been reported by the Korgel group and the Sargent group. [62,63]

Guo *et al.* have also prepared fairly stable solar cells based on $CuInSe_2$ nanocrystals.[61] In their experiment, molybdenum coated soda lime glass substrates were coated by $CuInSe_2$ nanocrystal ink by simple drop cast methods. In order to avoid loss of Se from the film, sintering of the layer was carried out at 500 °C in the presence of Se vapors and subsequently CdS layer was deposited by using chemical bath deposition. Finally a transparent layer of conducting oxide was grown by sputtering. 2.8% Efficiencies were obtained while final device architecture may be represented as soda-lime

glass/Mo/sintered $CuInSe_2$/CdS/i-ZnO/ITO/Ni/Al. Panthani *et al.* have demonstrated that photovolatic devices having 0.2% efficiency can be fabricated without carrying out any sintering.[62] A company Nanosolar has been actively pursuing development of thin film solar cells based on CIGS absorber layer from nanocrystal precursors. Lab-scale device with 13.95% power conversion efficiency have already been reported by the company.[64]

It may be concluded that the nanocrystals of $CuInSe_2$ and its gallium alloy (CIGS) are the most promising materials as solar photo-absorbers. They may yield the devices with higher efficiencies and reduced manufacturing cost. However, much effort is still required to evolve an even clearer understanding of the phenomena of nucleation and growth. Further insight into role of additives, ligands, surfactants and impurities during nanocrystals growth would be helpful in suitably controlling morphology of nanocrystals as well as controlling formation of alloys and heterostructures. It is imperative to evolve simple, safe and reproducible large-batch synthetic strategies that give higher yields of materials and offer precise control over surface morphology and size-dispersion.

1.8 Copper selenide

The semiconductor copper selenide (CuSe) has attracted significant research attention during the past few decades mainly because of its exciting photoelectrical characteristics. It has found wide range of applications in electronic and optoelectronic devices like solar cells,[65-67] optical filters,[68] thermo electric converters,[69] and super ionic conductors.[70,71] A number of stoichiometric compositions like (CuSe, Cu_2Se, $CuSe_2$, Cu_3Se_2, Cu_5Se_4, Cu_7Se_4, etc.) and various non-stoichiometric compositions ($Cu_{2-x}Se$), have been reported for copper selenide.[72-76] Copper selenide crystals have been grown into a number of crystallographic structures like cubic, monoclinic, tetragonal, orthorhombic and hexagonal.[77] At room temperature, CuSe exists as hexagonal phase but at 48 °C, it is converted to orthorhombic form and reverts back to hexagonal form at 120 °C.[78]

Due to special constitution and properties of these compositions, copper selenide have been extensively studied in recent years. A large diversity of techniques has been explored for depositing thin films of copper selenide. A few

techniques to name here include the vacuum evaporation,[79] melting of elemental copper and selenium,[80] electrodeposition,[81,82] D.C. magnetron sputtering,[83] solution phase growth[84] and chemical bath deposition.[85,86] Lokhande and co-workers have used solution growth techniques for room temperature deposition of copper selenide semi-conductor thin films onto glass substrates.[87] The films possessed monoclinic crystal structures with needle like fine grain particles. Paul O'Brien and co-workers have reported the deposition of highly oriented copper sulfide and copper selenide thin films by LP-MOCVD and AACVD from new asymmetric carbamato- compound $Cu[E_2CNMe^nHex]_2$ (where E=S, Se) as single source precursor.[88] The growth of CuSe films by AACVD was found to be problematic with these precursors whereas good quality films were obtained using LP-MOCVD.

Liu *et al.* have synthesized chalcogen bridged copper cluster $[Cu_4\{Se_2P(O^iPr)_2\}_4]$ and used it for the deposition of non-stoichiometric copper selenide $Cu_{2-x}Se$ nanowires onto fused amorphous silica substrates in a hot-wall tubular quartz reactor by CVD under reduced pressure.[89] Characterization revealed that a thin film of CuSe was first formed on the substrate surface as a result of thermal decomposition of the precursor. Subsequently, the $Cu_{2-x}Se$ nanowires were grown on the CuSe thin film through a self-catalytic vapor-liquid-solid (VLS) growth mechanism with Cu particles generated in-situ acting as the catalyst. The $Cu_{2-x}Se$ nanowires were found to have direct band gap absorption at 558 nm and emit excitonic photoluminescence at 575 nm. More recently, Sharma and co-workers have carried out the deposition of semi-conducting thin films of copper selenide onto glass substrates using cupric chloride, selenium powder, sodium sulphite, and ammonia at room temperature by solution growth technique.[90] It was revealed by scanning electron microscopy (SEM) and atomic force microscopy (AFM) studies that fairly uniform deposition was obtained. The average grain size was found to be 144.53±10 nm while the optical band gap was 2.03 eV. Surface roughness was calculated as 13.1 nm.

Fewer reports of preparing size and shape controlled copper selenide nanocrystals have also appeared in the literature. Some of the methods employed for producing nanoparticles include mechanical alloying,[91] gamma irradiation,[92] microwave assisted heating,[93] sonochemical method,[94,95]

hydrothermal method,[96] electrodeposition,[97] solid-state chemical reaction,[98] and solution-phase chemical reaction.[99-101]

1.9 Indium selenide

Indium selenide, a representative of the III-VI binary chalcogenide family of compounds, consists of Se – In – In – Se sheets bound together by weak van der Waal forces. These sheets are in turn arranged two dimensionally to give hexagonal crystalline structure. By virtue of such a layered structure, InSe semiconductor materials exhibit highly anisotropic optical and electronic properties as intercalation of atoms or molecules is possible without destroying the initial structure.[102] At room temperature, InSe has a band gap about 1.24 eV at room temperature, which is pretty close to the value calculated theoretically for obtaining maximum efficiency in solar devices. Efficient current collection is also feasible as InSe has a minority carrier diffusion length of about 10 μm.[103] These features make indium selenide a potentially suitable material for solar photovolatics.[104] InSe may also be employed for heterojunction device applications because of the absence of dangling bonds on the (001) surface.

Furthermore, InSe is a useful material for electrochemical devices like solid solution electrodes.[105] Indium selenide (In_2Se_3) can present five different phases including α, β, γ, k and δ- phases. Among these phases, α and β phases have further structures, namely hexagonal and rhombohedral structures.[106] Due to this phase structure, In_2Se_3 has also been used as a programmable material in phase change random access memory (PRAM) applications.[107]

In_2Se_3 thin films have been grown by exploiting many techniques like evaporation, sol-gel synthesis,[108] MBE[109] and MOCVD including LP-CVD and AACVD.[110,111] Deposition of In_2Se_3 thin films is commonly encountered with the problems of obtaining polyphasic mixture or the materials with bad orientation, unless expansive deposition techniques are employed. The single source precursor approach has been used to deposit good quality thin films of indium selenide. Deposition temperature, decomposition mechanism, and the choice of precursor are the important parameters which determine the quality of deposited materials. Molecular design of the precursor can play an important role in the deposition route taken and in determining the nature of the thin films

deposited. Bochmann has investigated the control of deposited phase of material in the CVD of indium and gallium chalcogenides.[112]

Barron and co-workers have reported the synthesis of a number of dialkylindium selenolates and alkylindium selenides, and deposited indium selenide films by LP-MOCVD.[113] Indium-rich In_2Se_3 films were deposited from $[(But)_2In(SeBut)]_2$ precursor using LP-MOCVD at temperatures between 230 °C and 420 °C. Whereas $[(Me_2EtC)InSe]_4$ gave crystalline films of InSe, the film quality being dependent on the growth temperature employed. Gysling and co-workers have also prepared thin films of indium selenide on GaAs (100) from $[(Me)_2In(SePh)]$ and $[In(SePh)_3]$ by a spray-assisted MOCVD technique.[114] Pyrolysis of $[In(SePh)_3]$ gave hexagonal films of In_2Se_3 at temperatures of 470–530 °C whereas the cubic phase is observed at deposition temperatures between 310 °C and 365 °C. Choi *et al.* and Cho *et al.* have reported deposition of phase pure polycrystalline InSe films from $[Me_2In(SeMe)]_2$ precursors at temperatures from 270-310 °C.[115,116]

Paul O'Brien and co-workers have reported the deposition of cubic In_2Se_3 films on glass substrates at 450 °C using the diselenocarbamate $[In\{Se_2CN(Me)Hex\}_3]$ precursor.[117] They have also synthesized the $In[(SeP^{i}Pr_2)_2N]_2Cl$ precursor and used it for deposition of indium selenide thin films on glass, Si (100) and polycrystalline GaAs substrates by AACVD at 375 - 425 and by LP-CVD at 475 - 525 °C.[118] It was found that only hexagonal γ-In_2Se_3 had been deposited, regardless of the deposition temperatures. Furthermore, O'Brien *et al.* have carried out the synthesis of a new class of binary selenium single-source precursors based on the bidentate ligand bis(diisopropylselenophosphoryl)amide, $[NH(SeP^{i}Pr_2)_2]$, and deposited cubic Ga_2Se_3 and hexagonal γ-In_2Se_3 thin films by AACVD and LP-CVD.[119] Huang *et al.* have recently reported the deposition of polycrystalline In_2Se_3 films onto Si (111) substrates by MOCVD technique at the temperatures higher than 500 °C. It has been demonstrated that the growth temperature greatly influences the structure of In_2Se_3 films.[120] γ-In_2Se_3 was the only recognized phase at the growth temperatures below 450 °C, while β-In_2Se_3 could also be found when the film was grown at above 450 °C.

There have appeared relatively fewer reports of the growth of indium selenide nanoparticles in the literature. Poly(vinyl alcohol) PVA stabilized (2-3

nm) and sodium metaphosphate stabilized (30 nm) In_2Se_3 colloids were prepared by Dimitrijevic and Kamat.[121] InSe quantum dots capped with tri-n-octylphosphine oxide (TOPO) and 4-ethylpyridine have been previously synthesized and characterized using tris(diethyldiselenocarbamato)indium(III) as single source precursor.[122] Quantum size effects were shown in the optical absorption and photoluminescence spectra of the synthesized quantum dots showed quantum size effects as there was observed a clear blue shift from those of their corresponding bulk materials.

David F. Kelly and co-workers have synthesized InSe nanoparticles by high temperature reaction between trimethylindium $In(CH_3)_3$ and trioctylphosphine selenium (TOPSe) in TOPO/TOP system. Optical spectroscopy and photophysical characteristics of the nanoparticles have been thoroughly investigated.[123-126] GaSe/InSe Core/Shell nanoparticles having GaSe as core and InSe as shell have also been prepared by Kelly *et al.* through pyrogenation of organometallic precursors at high temperature and some fundamental features concerning relative energetics and charge transfer between the GaSe core and InSe have been explored using absorption spectroscopy as well as static and time resolved emission spectroscopy.[127]

Amorphous In_2Se_3 nanoparticles ranging in size from 40-80 nm have been synthesized by Rabchynski *et al.* through photoelectrochemical reduction of an elemental selenium electrode in a solution of $InNO_3$.[128] Paul O'Brien and co-workers have carried out the colloidal preparation of various phase pure indium chalcogenides of type InE and In_2E_3 (where E = S, Se or Te) by reacting indium acetate with elemental chalcogen in hexadecylamine (HDA) at 300 ^oC. Meyyappan *et al.* have carried out metallic gold catalyzed synthesis of one dimensional hexagonal β-In_2Se_3 nanowires via thermal evaporation.[129] It was further demonstrated that the growth of NWs can also be affected by self catalysis of indium which eliminates the potential risk of gold contamination.

1.10 Gallium selenide

Gallium selenide, another representative of the III-VI family of semiconductor materials, exhibits a hexagonal layered structure containing sheets of Se-Ga-Ga-Se. The sheets are held together only by weak van der Waals forces, which determine the physical appearance of the bulk solid. Four

different crystal structures (β, γ, δ and ε) have been reported for GaSe, depending upon the difference in stacking arrangement of Se-Ga-Ga-Se on each other.[130,131] GaSe is an indirect band gap semiconductor which has a direct band gap energy of 2.11 eV and there is quite a small difference (about 25 meV) between the direct and indirect band gap values.[132]

In layered III-VI crystals like GaSe, GaS, GaTe, InSe and InS, a very important role is played by free excitons in determining photoconductivity and optical characteristics. There are two different types of excitons in GaSe: two- and three-dimensional. The two-dimensional exciton is associated with the indirect transition and is characterized by the effective mass tensor having a very large value along the (unique) *z* axis. The three-dimensional exciton has an approximately isotropic effective mass, with a Bohr radius of 31 Å.[84] Gallium selenide has a number of exciting properties for non-linear optical applications. It is regarded as one amongst the most important nonlinear-optical materials for optoelectronics and for IR frequency conversion.[133] There have been numerous studies for investigating non-linear optical,[134] photoluminescence,[135,136] exciton resonance,[137] electroluminescence[138] and femto-second excitonic effects[139] in these crystals.

While deposition of gallium sulfide thin films and nanoparticles has been undertaken by many groups, there are relatively fewer reports of the deposition of gallium selenide thin films as well as nanoparticles. Barron and co-workers have synthesized a number of metal chalcogenide complexes with cubane structure and deposited hexagonal phase of GaSe by AP-MOCVD at temperatures ~350 °C.[140,141] The compound $[Me_2Ga(SeP^iPr_2)_2N]$ has been prepared via the reaction of Me_3Ga with $NH(SeP^iPr_2)_2$ and used for deposition of cubic Ga_2Se_3 thin films by AACVD and LP-MOCVD.[142] Thin films of cubic Ga_2Se_3 have been grown from Me_3Ga in combination with H_2Se or $^tBu_2Se$. It was found that Me_3Ga initially reacts with H_2Se in the gas phase to give films, which are only partially epitaxial. However, the use of $^tBu_2Se$ yielded superior films of good crystal quality.[143]

T. P. Gujar and co-workers have obtained one dimensional quantum dots of GaSe on tin doped ITO substrates by cathodic electrodeposition using $Ga(NO_3)_3$ and H_2SeO_2 as gallium and selenium sources respectively.[144] XRD showed a mixture of GaSe and Ga_2Se_3 and bandgap of the material was found

to be 2.85 eV with intermediate transition at 1.9 eV. Controlled synthesis of layered GaSe nanowires during evaporation of GaSe powder has been reported by Peng *et al.*[145] Growth occurs through catalyst-assisted vapor-liquid-solid (VLS) growth mechanism. Straight, zigzag, and saw-tooth shapes were the predominant morphologies obtained in their study at different growth temperatures. Recently, thin films of semiconductor Ga_2Se_3 have been prepared using sol–gel method for different crystal formation temperatures.[146] The XRD analysis revealed formation of β-Ga_2Se_3 crystal phase while band gap energy for these thin films was calculated as ~ 2.56 eV.

There have been even fewer reports for the synthesis of GaSe nanoparticles in literature. Barron and co-workers have decomposed the Ga–Se and In–Se clusters $[BuGaSe]_4$ and $[(EtMe_2C)InSe]_4$ in the solid state to produce nanoparticles of GaSe and InSe, respectively.[147] They obtained nanoparticles by thermolyzing heterocubane molecules in vapor phase under CVD conditions. TEM analysis showed a string of pearls like arrangement of GaSe particles with 42 ± 13 nm diameter. Broad rings that are consistent with poorly crystalline GaSe were observed in SAED pattern of these nanoparticles. Allakhverdiev *et al.* have reported the synthesis of GaSe colloids using ultrasonic treatment of bulk GaSe in methanol.[148] Based on absorption spectra, their results showed wide size distribution. Chikan and Kelly have carried out high temperature inorganic synthesis of surface capped GaSe nanoparticles by the reaction of trimethylgallium (Me_3Ga) with trioctylphosphine selenium (TOPSe) in TOPO/TOP system. The diameter of nanoparticles obtained ranged from 2-6 nm with an average diameter of 4 nm. C. N. R. Rao and co-workers have obtained layered GaS and GaSe materials, which possessed mica-type morphologies, form nanotubes and onion like structures on exfoliation by laser irradiation or thermal treatment.[149] Uniform and straight nanotubes having an inner diameter of 5 nm and outer diameter of ~20 nm were obtained in their experiments.

1.11 I-III-VI_2 Chalcopyrite Semiconductors

For thin film solar photovoltaics, chalcopyrite materials based on $CuInSe_2$ (copper indium selenide, CIS) are considered as the most important and promising photoabsorber materials. Partial replacement of indium by gallium

and/or part of selenium by sulfur results in formation of $Cu(In,Ga)(S,Se)_2$ materials, which have significantly different optoelectronic properties. Above 19% power conversion efficiencies have already been reported for solar devices based on these materials.[150] Furthermore, solar cells based on CIS offer yet another advantage of being very stable to photoirradiation, and thus exhibit fairly longer operational lifetimes. The favourable optoelectronic features (direct energy band gap and high absorption coefficient) for these materials make it feasible to use thin films of few microns thickness, thus reducing the material consumption. Both gas and liquid phase deposition strategies and a wide range of methods can be employed for producing CIS-based thin films.

As mentioned before, CdTe and $Cu(In,Ga)(S,Se)_2$ polycrystalline semiconductor materials exhibit excellent photoirradiation stability. No light-induced degradation occurs in these materials and therefore, traditional drawback of degradation, commonly encountered in previous thin film solar cell technologies, is suitably circumvented. Even improved performance is shown by solar cells based on CIS after illumination under usual operating environment.[151,152] Their high absorption coefficients because of being direct band gap semiconductor materials offers further advantage. CdTe has band gap energy of 1.4 eV which is fairly close to the ideal value. However, so far maximum efficiency achieved for CdTe based solar cells is only 16.5 % which is merely half of the efficiency value expected theoretically for this material. $CuInSe_2$ has a relatively lower band gap value of 1.04 eV, but partial substitution of In by Ga or Se by S can yield materials which have ideal bandgap for efficiently harvesting the solar spectrum. Theoretically, this flexible material system may allow band gap tuning from 1.04 eV for $CuInSe_2$ to 2.5 eV for $CuGaS_2$ via band gap energy of 1.53 eV for $CuInS_2$ and 1.7 eV of $CuGaSe_2$.[153]

Tetragonal chalcopyrite structure is most often observed crystallographic arrangement in case of ternary Cu-chalcogenides.[154] This type of structure is shown in Figure 1.9. However, a disordered form of the chalcopyrite, called as the cubic sphalerite phase, has also been reported. An excellent review published by Bily J. Stanbery covers the phase chemistry, crystallography and optoelectronic properties of copper indium diselenide and related semiconductors.[155]

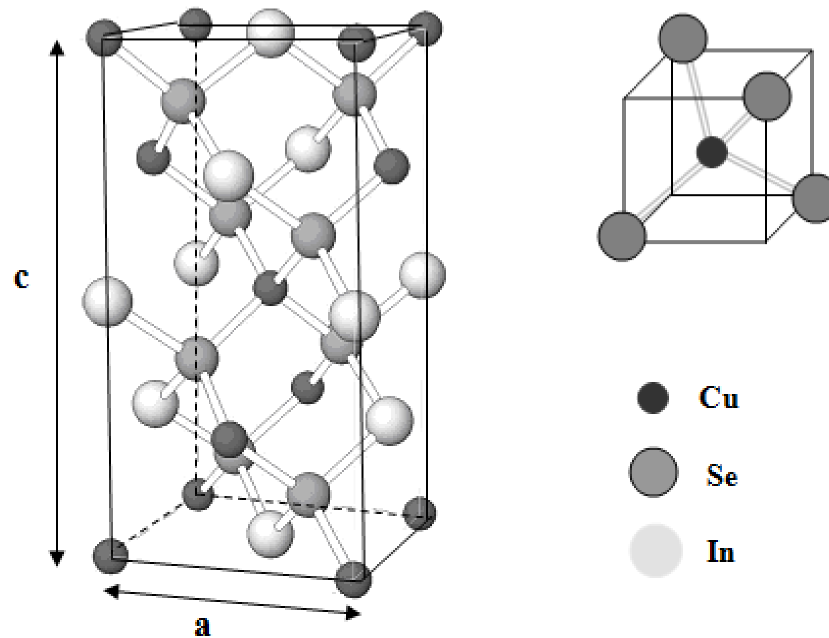

Figure 1.9 Schematic representation of $CuInSe_2$ chalcopyrite crystal structure

1.11.1 Factors affecting the performance of I-III-VI_2 materials

Although optoelectronic properties of I-III-VI_2 materials and solar photovoltaic devices based on these materials are considerably influenced by gallium and sulphur contents of the material, absorption efficiency of the device largely depends on the Cu/(Ga+In) ratio. Better efficiencies are achieved with materials having overall slightly Cu-deficient stoichiometry. On the surface, a thin layer having even more Cu-deficient composition yields further improved efficiency. The composition of this surface layer corresponds to the stable ordered vacancy or ordered defect compound (OVC/ODC) $Cu(In,Ga)_3Se_5$.[156,157] Formation of OVC layer occurs automatically on surface of slightly Cu-deficient $Cu(In,Ga)Se_2$ films if the deposition process is carried out at higher temperatures and higher than 0.52 In/(In+Cu) ratio exists in the bulk of the film. Thus the bulk stoichiometric composition and surface compositions for high quality $Cu(In,Ga)Se_2$ films for solar cell applications are significantly different. Some authors suggest that such an OVC layer may only be formed in absorber films prepared by co-evaporation process.[158]

Theoretically, one would expect that compound semiconductors of the $Cu(In,Ga)(S,Se)_2$ family having higher band gap may yield devices with higher power conversion efficiencies, but the practical situation is somewhat different. $CuInS_2$ having bandgap of 1.53 eV or $CuGaSe_2$ with band gap value of 1.7 eV, exhibit comparatively lower conversion efficiencies than those achieved by low bandgap absorbers like $Cu(In,Ga)Se_2$ or $CuInSe_2$. 14.5%,[159] 9.5%,[160] and 11.1%,[161] respectively are the highest total area power conversion efficiencies achieved for $CuInSe_2$, $CuGaSe_2$, and $CuInS_2$ absorbers. Highest efficiencies in this family of materials have been recorded for CIGS solar absorbers having relatively lower Ga content. For example, the ratio of Ga to (Ga+In) varies in the range of about 15 - 50% as depth of the absorber increases in absorber layer of highest efficiency (19.2%) device. Band gap of the resulting material is 1.12 eV. Furthermore, this ratio varies from 25 – 30% in other high-efficiency devices, while band gap of the material ranges from 1.1 to 1.2 eV.[162-165]

For CIGS material with Cu-poor stoichiometry, defect densities of the absorber material significantly impede open circuit voltages of the cells.[166,167] CIGS materials with Ga/(Ga+In) ratio of around 25–30% and band gap of about 1.2 eV have minimal defect densities and therefore manifest maximum open circuit voltages of solar cells.

Besides power conversion efficiency, stability is yet another factor having crucial effect on cost of electricity generated by the solar cell and on energy payback time. CIGS based solar cells have demonstrated excellent stability under usual working environment. Furthermore, irradiation by X-rays,[168] electrons,[169-170] or protons[171] did not induce any degradation in the performance of the solar cells based on these materials. Due to this radiation hardness, CIGS based solar cells are also considered suitable for space applications.

1.11.2 Deposition techniques for I-III-VI_2 chalcopyrite semiconductors

Many techniques have been used for deposition of the thin film materials employed in $CuInSe_2$ based solar cells. Kemell *et al.* have published an excellent review covering various thin film deposition methods employed for $CuInSe_2$ and related materials.[172] In general, the deposition techniques have significant influence on the properties of the resulting thin films. Choice of the

deposition method is also a decisive factor in determining the overall production costs of the photovoltaic cells and the modules. The most important deposition methods, especially those applied for deposition of the absorber material are briefly reviewed here. More emphasis would lie on the deposition techniques used for CIS and CIGS, because these are the most promising absorber materials in the family of Cu chalcopyrite semiconductors. To more or less extent, the same deposition techniques have also been employed for deposition of $CuGaSe_2$ and $CuInS_2$ thin films.

Thin films of stoichiometric $CuInSe_2$ and CIGS have been obtained by using a variety of techniques that include chemical vapor deposition, deposition of metallic layers followed by their chalcogenization, co-evaporation, evaporation from compound sources, electrodeposition, mechanical alloying *etc.* So far, high efficiency CIGS solar cells having conversion efficiencies of >15 % have been fabricated by using only a few techniques for deposition of absorber layer. Deposition of the CIGS absorber films for these cells is generally carried out by co-evaporation or by employing reactive annealing of precursor films under selenium containing (H_2Se or elemental Se vapor) atmospheres.[173]

Regardless of the deposition technique, the absorber film in high efficiency CIS based solar cells comprises of densely packed and large grains having smooth surface morphologies. The films have chalcopyrite structure and exhibit good crystallinity. Furthermore, they possess slightly Cu-deficient stoichiometry which gives rise to Cu-poor ordered vacancy compound (OVC) on the surface. Presence of additional phases like a copper selenide phase retards the solar cell performance. Higher temperatures (400 °C or above) are required either during deposition of film or during post-deposition annealing to obtain photovoltaic-quality films. Generally, formation of Ga-containing phases (CGS and CIGS) would require relatively longer reaction times and/or higher temperatures than those employed for the deposition of CIS phases.[174] An atmosphere of Se must be maintained to compensate for loss of Se at the higher process temperatures.

The most successful strategy for deposition of an absorber layer in small area high efficiency solar devices involves three-stage co-evaporation of CIGS from elemental sources in the presence of excess Se vapor.[175] Orientation,

morphology, and grain size of the obtained films is greatly influenced by the Se/metal flux ratio.[176] Ultra high vacuum conditions are used to carry out deposition. The three stage process, employed by the US National Renewable Energy Laboratory (NREL), finds its origin in the bilayer process initially developed by Boeing.[177] The process starts with deposition of $(In,Ga)_2Se_3$ layer first at a relatively lower substrate temperature of about 300–350 °C. Subsequently, it involves high temperature evaporation of Cu and Se, thus yielding Cu-rich CIGS layer. Finally, some more $(In,Ga)_2Se_3$ is added to achieve desired, slightly Cu-deficient final film composition and the film is treated by Se vapors during the cooling process. A graded band gap is obtained by varying the Ga/(Ga+In) ratio as a function of depth. Several variants of this three-stage deposition process exist and many groups have reported ~ 20% solar cell efficiencies for CIGS absorber films obtained from three-stage co-evaporation process.

In this process, orientation of the underlying $(In,Ga)_2Se_3$ precursor layer determines the orientation of $CuInSe_2$ and CIGS thin films. Chaisitsak *et al.* have suggested that the most important factor determining orientation is the Se/(In+Ga) flux ratio during evaporation of $(In,Ga)_2Se_3$ precursor layer.[176] Higher flux ratios give rise to CIGS films with predominant orientation along (220/204). The opposite effect is observed if increased substrate temperature is used during first stage of the process. It was found that the (220/204) oriented CIGS films were more resistive to photo-degradation than (112) oriented films and they have lower apparent band gaps than corresponding (112) oriented films.

Though co-evaporation has demonstrated unrivalled strength in deposition of high quality material on a small area, there are some problems associated with upscaling of this technique. This is because of the fact that stringent control of the evaporation flux is difficult to achieve with larger substrates and hence desired properties of film like stoichiometric composition, surface texture, and electrical properties cannot be achieved. Consequently, large area solar cells and solar modules exhibit lower power conversion efficiencies than corresponding smaller-area devices.[178] Furthermore, this process requires sophisticated and costly equipment besides involving higher deposition temperatures. Incomplete utilization of source materials is another

issue which causes further increase in the cost and complexity of the co-evaporation method.

1.11.3 Selenization of metallic precursor layers

If a multi-step approach, involving a number of simple and effective deposition techniques, is used for deposition of absorber layer, it can offer better uniformity in composition on larger substrates. Further beneficial features will be better cost effectiveness and higher throughput. One amongst the most commonly employed multistep approach involves deposition of metal or metallic alloy layers by electrodeposition, evaporation or sputtering and then subsequent selenization of these layers. Higher temperatures have also been used for deposition of precursor layers, but in general, such depositions are carried out at or near room temperature. Pre-annealing of the metal precursors at lower temperatures before selenization facilitates alloy formation. It has been observed that relatively slower reaction occurs between successively deposited Cu/Ga layers than that in analogous Cu/In layers.[179] In another approach, multilayers of Cu/In/Cu/In/Cu/In . . . are deposited instead of a bilayer and resulting materials exhibit relatively smooth surface textures and improved crystallinity.[180]

The process of selenization is carried out at higher temperatures, usually higher than 400 °C in an atmosphere of elemental Se or H_2Se (diluted by Ar). During selenization, CIS is formed relatively faster and at lower temperatures as compared to CGS. Consequently, CIS and CGS may be found as separate phases in CIGS films if lower reaction temperature or shorter selenization times are employed. Thin films of $CuIn(S,Se)_2$ can also be obtained if both the S and the Se precursors are introduced during chalcogenization.[181]

1.11.4 Chemical vapor deposition

Chemical vapor deposition (CVD) has attracted a great deal of research interest because of its versatile application for deposition of a wide range of materials. It offers further advantage that it has the potential for scaling up the technique for larger substrates. Such potential has been amply demonstrated by deposition of transparent conductors of SnO_2 and self cleaning coatings of TiO_2. Atmospheric pressure metal organic chemical vapor deposition (AP-

MOCVD), plasma enhanced chemical vapor deposition (PE-CVD), low pressure chemical vapor deposition (LP-CVD) and aerosol assisted chemical vapor deposition (AACVD) are variants of the conventional chemical vapor deposition process used for deposition of CIS thin films.

Duchemen *et al.* have used APMOCVD for deposition of $CuInSe_2$ from complexes of $Cu(hfac)_2$ (where hfac = hexafluoroacetylacetonate) with trimethylamine and diethylamine as precursors for Cu while trimethylindium and triethylindium were used as the In precursors.[182,183] H_2Se was used as the Se source. Whatever metal ratios were used in the depositions at 400 °C, thin films exhibiting strong (112) orientation were obtained. P. A. Jones and co-workers have used plasma-enhanced CVD processes to grow CIS films from $Cu(hfac)_2$ and $In(hfac)_3$ as the metal precursors for Cu and In, respectively whereas 4-methyl-1,2,3-selenadiazole was used as the Se source. Deposition of Se deficient films resulted at temperatures ranging from 150 to 400 °C.[184]

$CuInSe_2$, $CuInS_2$, and $CuGaS_2$ thin films have been deposited by O'Brien *et al.* using Cu(II) and In(III) complexes of methyl-*n*-hexyl-diselenocarbamate as dual-source precursors by LP-CVD and AACVD. In LP-CVD experiments, the polycrystalline $CuInSe_2$ films were obtained at 400–450 °C while keeping the precursors at 180–250 °C. CIS films thus obtained had a bandgap of about 1.08 eV. In AACVD experiments, the precursors were dissolved in tetrahydrofuran (THF) or toluene and aerosols generated by means of an ultrasonic humidifier were transported to the reactor with the help of the carrier gas. The substrate temperature was between 425 and 475 °C. The resulting films were chalcopyrite $CuInSe_2$.[185,186] They have also used Cu(II) and In(III) complexes of iminobis(diisopropylphosphineselenide), for deposition by AACVD. At deposition temperatures ranging from 375 and 450 °C, as deposited CIS thin films were shown to be (112) oriented chalcopyrite phase having desired, slightly Cu-deficient composition.[187]

Banger *et al.* have reported the synthesis of single-source precursors for various ternary chalcopyrite materials. Preliminary deposition studies using $(PPh_3)_2Cu(SeCH_3)_2In(SeCH_3)_2$ yielded near stoichiometric chalcopyrite $CuInSe_2$ films with strong (112) orientation.[188,189] More recently, Choi and co-workers have applied MOCVD for deposition of III-VI, II-VI and CIS layers.[190-193] This group has also carried out deposition of CIS-CGS double layer from [$(Me)_2In(\mu$-

SeMe)]$_2$, [(Me)$_2$Ga(μ-SeMe)]$_2$ and (hfac)Cu(I)(DMB) precursors by LP-CVD.[194] No formation of CIGS alloy was observed in this study.

Several approaches have been employed for the controllable synthesis of $CuInSe_2$ and related semiconductor nanoparticles. However, many of these approaches suffer the drawbacks that they either lead to the formation of binary structures or additional phases are formed and precise control over structure, morphology and composition becomes somewhat difficult. Besides cost per kilowatt of power produced is too much as most of these processes traditionally require vacuum deposition resulting in loss of materials and cannot be scaled up to reduce manufacturing costs to an optimum level. PV module manufacturing costs may be significantly decreased by avoiding deposition processes that require higher vacuum, higher deposition temperatures, longer processing periods and expansive precursors as well as substrate materials. Consequently, as ideal approach would be utilization of solution-phase processes, lower processing temperatures, shorter processing time and flexible cheaper precursors and substrates that allow optimal scale up like 'roll to roll' manufacturing process.[195]

In recent years, research efforts have been focused on solution-phase approaches and significant improvement has been carried out in the colloidal synthesis of $CuInSe_2$ and related materials as the method offers good control over size, morphology and structure of the nanoparticles. O'Brien *et al.* have carried out the synthesis of $CuInSe_2$ nanoparticles from a two-step reaction using CuCl, $InCl_3$ and TOPSe in TOPO.[196] Castro and co-workers have synthesized chalcopyrite semiconductor nanoparticles of $CuInS_2$ and $CuInSe_2$ by thermal decomposition of ternary molecular single source precursors $(PPh_3)_2CuIn(SEt)_4$ and $(PPh_3)_2CuIn(SePh)_4$ in dioctyl phthalate at temperatures from 200-300 °C.[197] Sargent *et al* have reported the synthesis of $CuInSe_2$, $CuGaSe_2$ and $CuInGaSe_2$ nanoparticles in oleylamine using metal salts and selenium powder.[198] Allen and Bawendi have used hot injection synthetic methodology to synthesize luminescent Cu-In-Se quantum dots of varying stoichiometric composition using metal halides and $[(Me_3Si)_2Se]$ in a combination of TOP and oleylamine as a coordinating solvent.[199] Korgel and co-workers have carried out synthesis of $CuInS_2$, $CuInSe_2$ and $CuIn_{1-x}Ga_xSe_2$

nanocrystals with controlled In/Ga ratio in oleylamine at 240 °C and used these nanocrystals as absorber layer in prototype photovolatic devices.[200] Recently, Mitzi et al have reported a solution-based approach for deposition of CIGS absorber layer that involves dissolving the elements in a hydrazine based solvent system, spin coating the precursor elements as thin films and heating in inert atmosphere at temperature < 500 °C to obtain CIGS layer. The process did not involve any post treatment and the PV devices constructed from this layer have reported power conversion efficiency of up to 10% (1.5 illumination).[201]

1.12 Phosphorus-chalcogen-metal ring system containing compounds as single source precursors

In recent years, synthesis of novel single source precursors (SSPs) and subsequent deposition of thin films and nanoparticles from these precursors has attracted significant research interest. Use of SSPs offers many advantages over conventional metal – organic chemical vapor deposition (MOCVD) process, as it avoids the use of highly toxic and/or moisture sensitive gases like H_2S, H_2Se, SiH_4, NH_3 etc. Furthermore, industrial processes utilizing SSPs are expected to be safer, cost effective and better controlled. Metal chalcogenide semiconductor thin films and nanomaterials find many useful applications in industry. Therefore, considerable reports have appeared in the literature during the past two decades that focus on the synthesis of inorganic rings having P – E – M and N – P – E – M (where E = S, Se, Te and M = metal) and their utilization as SSPs for metal chalcogenide thin films and nanoparticles.

Schmidpeter *et al.* have reported the synthesis of imidodiphosphinic acid derivatives $R_2P(E)NH(E)PR'_2$ (where R, R' = CH_3, C_6H_5; E = O, S, NH).[202] Subsequent research efforts have resulted in the synthesis of a wide range of derivatives (where R, R' = ^{i}Pr, ^{t}Bu, Et, OEt, OPh and E = S, Se).[203,204] Synthetic procedures typically involved condensation of R_2PCl with $NH(SiMe_3)_2$ yielding the phosphorus (III) compound which upon oxidation with O, S or Se gave dichalcogenoimidophosphinate derivatives (Eq. 1).

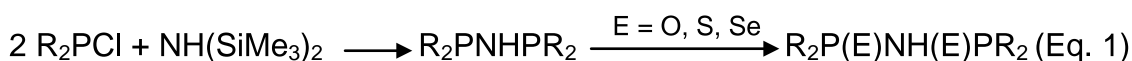

$$2\,R_2PCl + NH(SiMe_3)_2 \longrightarrow R_2PNHPR_2 \xrightarrow{E\,=\,O,\,S,\,Se} R_2P(E)NH(E)PR_2 \quad \text{(Eq. 1)}$$

Deprotonation of the amine N – H formed a bidentate ligand which was structurally analogous to an acac system and produced neutral complexes of the type $M[N(R_2PE)_2]_x$ upon reaction with many transition as well as main group metals. Many groups have successfully utilized Se analogues of these complexes as SSPs for the deposition of metal selenide thin films and nanoparticles.[205,206]

Chivers et al. have reported synthesis of tellurium ligand $Na[N(TeP^iPr_2)]_2$ by metallation of R_2PNHPR_2 by NaH and subsequent reaction with Te in hot toluene in the presence of TMEDA.[207,208] Reaction of this ligands with suitable metal halides gave $M[N(TeP^iPr_2)]_n$ complexes which were fairly stable.[209] Some of these complexes $M[N(TeP^iPr_2)]_2$ (M = Cd, Hg) have been used as SSPs to deposit metal telluride thin films by AACVD process.[210]

Ring systems like dichalcogenophosphate, dichalcogenophosphonate and dichalcogenophosphinate have similar PE_2 moiety (where E = S, Se) and thus form four membered PE_2M rings. Zingaro and co-workers have developed dialkyldiselenophosphate ligands and studied coordination chemistry of several O,O’-diethyldiselenophosphato)metals.[211-213] Liu et al. have reported a number of cluster compounds having dialkyldiselenophosphate ligands.[214-219] Synthesis of diselenophosphate ligand has also been carried out by reaction of Woolins reagent $(PhPSe_2)_2$ with RONa in ROH.[220] The reaction proceeded with cleavage of the four membered ring P_2Se_2.

Sulphur derivatives of dichalogenophosphinate species have been extensively studied.[221-225] However, very few reports on selenophosphinates have been published owing to the diffculty in the synthesis of these compounds. Kuchen and co-workers have reported the synthesis of diselenophosphinate ligand and related complexes.[226] Their synthetic strategy involved reaction of R_2PCl with Se powder to form R_2PSeCl, which upon treatment with NaSeH yielded the $Na[R_2PSe_2]$ ligand. Further reaction of this ligand with metal salts resulted in the formation of diselenophosphinatometal complexes. Muller and co-workers have used this approach to synthesize diphenyldiselenophospinate complexes of Ni, Co, Cd, Zn, Hg and Bi.[227] However, this approach had drawbacks as the $Na[R_2PSe_2]$ ligand was unstable and formation of NaSeH required highly toxic H_2Se gas. Pilkington *et al.* have prepared

$Na_2[Ph_2PSe_2]_2.THF.5H_2O$ by reaction of Ph_2PCl with Na and Se in liquid NH_3 at – 78 °C and reported its structure.[228] However, this synthetic approach was not reproducible. Later on, Davies and co-workers have evolved a new synthetic approach for preparation of diselenophosphinatometal complexes of lithium[229] and potassium.[230] Ion exchange reaction between $InCl_3$ and diselenophosphinatopotassium complex gave diselenophosphinatoindium complex as well.

Paul O'Brien and co-workers had previously obtained a mixture of $^ipr_2P(Se)NHP(Se)^iPr_2$ and $(^ipr_2PSe)_2Se$ at mild reaction conditions, while carrying out the synthesis of imidobis(diisopropylphosphineselenide) ligand by Woollins method.[231] Reaction of metal halides with this serendipitously formed $(^iPr_2PSe)_2Se$ exhibited exciting coordination properties as the reaction yielded $^iPr_2PSe_2$ units by cleavage of the P – Se bonds and these units act as bidentate ligands to give diselenophosphinatometal complexes. However, yield of reaction could not be improved beyond 10 % despite several attempts.

Detailed insight into the reaction mechanism revealed that an intermediate R_2PSiMe_3 is formed in the first step while Se is later inserted into the P – Si bond. It was therefore evident that the diselenophospinate ligand $(R_2PSe)_2Se$ can be synthesized by inserting Se into P – Si bond of the $R_2PSiR'_3$ and overall efficiency of the synthetic procedure depended on formation of $R_2PSiR'_3$ intermediate. Fritz *et al.* have reported that reaction of Li with R_2PCl forms R_2PLi which undergoes further exchange reaction between R_2PLi and R'_3SiCl to give $R_2PSiR'_3$ (Eq. 2). The reaction however, utilized extreme reaction conditions.

$$R_2PCl + Li \xrightarrow{THF} R_2PLi \xrightarrow{R_3SiCl} R_2PSiR'_3 \quad \text{(Eq. 2)}$$

Benkeser reaction can give a similar compound in high yield at normal reaction conditions.[232] Therefore, based on Bankeser reaction, O'Brien *et al.* have developed a new facile method to synthesis dialkyldiselenophosphinate ligands and obtained two different ligands by controlling the Se and R_2PSiCl_3 ratios in the reaction. The ligands thus obtained were characterized by spectroscopic methods and X-ray single crystallographic studies.

It was envisaged that ionic dialkyldiselenophosphinate ligand might offer better yield for complexation reactions because of its easy dissociation. Therefore, attempts were made to stabilize the $(R_2PSe_2)^-$ anion and its recrystallization as an ionic compound. The initial approach that involved use of excess amount of $HSiCl_3/NEt_3$ to produce enough counter ion $(HNEt_3)^+$ proved unsuccessful because the combination resulted in formation of $(HNEt_3)(SiCl_3)$ precipitate. However, when $HSiCl_3$ was replaced by $HSiEt_3$, ionic compounds $[HNEt_3]^+[R_2PSe_2]^-$ were obtained in fairly higher yields. The synthetic reaction can be represented as Eq. 3.

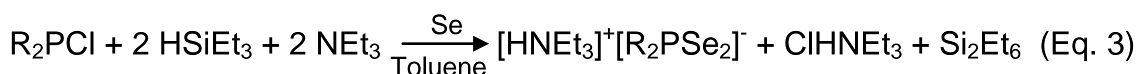

$$R_2PCl + 2\ HSiEt_3 + 2\ NEt_3 \xrightarrow[\text{Toluene}]{\text{Se}} [HNEt_3]^+[R_2PSe_2]^- + ClHNEt_3 + Si_2Et_6 \quad \text{(Eq. 3)}$$

By exploiting this synthesis approach, they have synthesized three ionic ligands having structure $[HNEt_3][R_2PSe_2]$ (where R = ^iPr, ^tBu, Ph) and dialkyldiselenophosphinatometal complexes of these ligands having $M_x[R_2PSe_2]_y$ structure were used to deposit metal selenide thin films by AACVD process.

In present work, $M_x[R_2PSe_2]_y$ complexes (where M = Cu, In, Ga) are used as single source precursors for the deposition of binary, ternary and quaternary metal chalcogenide thin films and nanoparticles by AACVD and colloidal method.

1.13 Aim and objectives

This research project is primarily aimed at finding the new and safer routes to ternary copper chalcogenide semiconductor materials for photovoltaic applications. In this work, diisoprpyldiselenophosphinatometal complexes with general formula $M_x[^iPr_2PSe_2]_y$ (Where M=In, Ga, Cu) will be synthesized and evaluated as precursors for the deposition of copper based **I-III-VI**$_2$ semiconductor thin films and nanoparticles. Objectives of the project include:

- To carry out synthesis and analysis of ionic ligand $[HNEt_3]^+[^iPr_2PSe_2]^-$
- To carry out synthesis and analysis of Diisoprpyldiselenophosphinatometal complexes with general formula $M_x[^iPr_2PSe_2]_y$ (Where M = In, Ga, Cu)

- To grow thin films and nanoparticles of $Cu_{2-x}Se$, In_2Se_3 and Ga_2Se_3 semiconductor materials using corresponding metal selenophosphinato complexes
- To establish the suitability of diisoprpyldiselenophosphinatometal complexes $M_x[^iPr_2PSe_2]_y$ as precursors for the deposition of thin films and nanoparticles of copper based ternary I-III-VI_2 chalcogenides
- To study the effect of various deposition parameters like deposition temperature, solvent, and molar ratio of precursors on optical properties and stoichiometric composition of as deposited thin films and nanoparticles
- To investigate the effect of growth temperature, reaction time and relative molar ratio of precursors on size, shape and stoichiometric composition of the nanoparticles grown by colloidal method
- To develop a strategy for deposition of thin films and nanoparticles, that offers better control over size, shape, phase and stoichiometry of the deposited material.

References

1 International Energy Agency, *World Energy Outlook 2008*, (IEA, Paris, France,2009)

2 Energy Information Administration, U.S. Department of Energy, *International Energy Annual, 2005* (EIA, U.S. Department of Energy, Washington DC. 2005)

3 United Nations Development Programme, *Human Development Report, Fighting Climate Change: Human Solidarity in a Divided World* (UNDP, 2007)

4 V. S. Arunachalam and E. L. Fleischer, *MRS Bulletin*, 2008, **33**, 265.

5 Massachusetts Institute of Technology, *The Future of Coal: Options for a Carbon Constrained World* (MIT, Cambridge, MA, 2005).

6 Energy Information Administration, U.S. Department of Energy, *World Net Nuclear Electric Power Generation*, *1980-2005*, (EIA, U.S. Department of Energy, Washington DC. 2007)

7 The Intergovernmental Panel on Climate Change, *IPCC Fourth Assessment Report (AR4)* (IPCC, 2007).

8 R. E. H. Sims, *MRS Bulletin*, 2008, **33**, 389.

9 N. G. Dhere, *Solar Energy Materials & Solar Cells*, 2007, **91**, 1376.

10 United Nations Development Programme, *World Energy Assessment: Energy and the challenge of Sustainability*, UNDP, New York, ISBN 92-1-1261-0 (Chapter 5: Energy Resources)

11 D. M. Chapins, C. S. Fuller and G. L. Pearson, *J. Appl. Phys.*, 1954, **25**, 676.

12 European Commission, A *Vision for Photovoltaic Technology, Report by the Photovaltaic Technology Advisory Research Council (PV-TRAC)*, European Commission, Brussels, Belgium, 2005.

13 V. Fthenakis, *Renewable and Sustainable Energy Reviews*, 2009, **13**, 2746

14 J. Zhao, A. Wang, M. A. Green and F. Ferraza, *Appl. Phys. Lett.,* 1998, **73**, 1991.

15 D. L. King, W. K. Shubert and T. D. Hund, Conference Record: 1st World Conference on Solar Energy Conversion, Hawaii, 1994, 1660.

16 D. M. Bagnall and M. Boreland, *Energy Policy*, 2008, **36**, 4390.

17 L. Kazmerski, *Renewable and Sustainable Energy Reviws*, 1997, **1**, 71.

18 K. Zweibel and M. A. Green, Millenium Issue, *Prog. Photovaltaics*, 2000, **8**, 1.

19 J. Meier, J. Sitznagel, U. Kroll, C. Bucher, S. Fay, T. Moriarty and A. Shah, *Thin Solid Films*, 2004, **451-452**, 518; J. Yang, A. Banerjee, T. Glatfelter, K. Hoffman, X Xu and S. Guha, Conference Records, 1st World Conference on Photovolatic Energy Conversion, Hawaii, December 1994, 380.

20 K. Yamamoto, M. Yoshimi, T. Suzuki, T. Nakata, T. Sawada, A. Nakajima and K.Hayashi, *Proceedings of the 28th IEEE Photovoltaic Specialists Conference-Anchorage*, IEEE, New York, 2000, 1428.

21 K. L. Chopra, P. D. Paulson and V. Dutta, *Prog. Photovolt: Res. Appl.,* 2004, **12**, 69.

22 X. Wu, J. C. Keane, R. G. Dhere, C. DeHart, A. Duda, T. A. Gessert, S. Asher, D. H. Levi and P. Sheldon. *Proceedings of 17th European Photovoltaic Solar Energy Conference,* Munich, 2001, 995.

23 I. Repins, M. Contreras, Y. Romero, Y. Yan, W. Metzger, J. Li, S. Johnston, B. Egaas, C. DeHart, J. Scharf, B. E. McCandless and R. Noufi. *IEEE Photovoltaics Specialists Conference Record*, 2008, 33; K. Ramanathan, M. A. Contreras, C. L. Perkins, S. Asher, F. S. Hasson, J. Keane, D. Young, M. Romero, W. Metzger, R. Noufi, J. Ward and A. Duda, *Prog. Photovolt. Res. Appl.,* 2003, **11,** 225.

24 L. L. Kazmerski, *Journal of Electron Spectroscopy and Related Phenomena*, 2006, **150**, 105.

25 M. A. Green, *Third Generation Photovoltaics: Advanced Solar Energy Conversion*, Springer, New York, 2003.

26 J. F. Geisz, S. Kurtz, M.W. Wanlass, J. S. Ward, A. Duda, D. J. Friedman, J. M. Olson, W. E. McMahon, T. E. Moriarty, and J. T. Kiehl, *Appl. Phys. Lett.,* 2007, **91**, 023502.

27 P. A. Cox, *The Electronic Structure and Chemistry of Solids*, 6th ed. Oxford University Press, 1995.

28 H. P. Myers, *Introductory Solid State Physics*, Taylor and Francis, London, 1990.

29 H. M Rosenberg, *The Solid State*, Oxford University Press, 1987.

30 A. L. Fahrenbruch and R. H. Bube, in '*Fundamentals of Solar Cells: Photovoltaic Solar Energy Conversion'*, Academic Press, New York, 1983.

31 B. G. Yacobe (Ed.), '*Semiconductor Materials – An Introduction to Basic Principles'* Kluwer Academic Publishers, New York, 2004.

32 M. Green and P. O'Brien, *Chem. Comm*., 1999, 2235; R. F. Khairutdinov, *Russian Chemical Reviews*, **67(2)**, 1998, 109; S.P. Gubin, N.A. Kataeva and G. B. Khomutov, *Russian Chem. Bull., Intl. Ed.*, 2005, **54(4),** 827.

33 R. D. Dupuis, P. D. Dapkus, R. D. Yingling, and L. A. Moudy, *Appl. Phys. Lett.*, 1977, **31(3**), 201.

34 R. D. Dupuis, *J. Selected Topics in Quantum Electronics*, 2000, **6(6),** 1040.

35 M. S. El-Shall, W. Slack, W. Vann, D. Kane, D. Hanley, *J. Phys. Chem.,* 1994, **98**, 3067.

36 M. Visca, E. Matijevic, *J. Colloid Interface Sci.,* 1979, **68**, 308.

37 A. Fojtik, H. Weller, S. Fiechler, A. Henglein, *Chem. Phys. Lett.,* 1987, **134**, 477.

38 A. Hagfield, M. Graetzel, *Chem. Rev.,* 1995, **95**, 49.

39 A. Hanglein, *Chem. Rev.,* 1989, **89**, 1861.

40 M. G. Panthani, V. Akhavan, B. Goodfellow, J. P. Schmidtke, L. Dunn, A. Dodabalapur, P. F. Barbara and B. A. Korgel, *J. Am. Chem. Soc.,* 2008, **130**, 16770.

41 Y. Jiang, Y. Wu, X. Mo, W. Yu, Y. Xie, Y. Qian, *Inorg. Chem*., 2000, **39**, 2964.

42 Y.-G. Chun, K.-H. Kim and K.-H. Yoon, *Thin Solid Films*, 2005, **480–481**, 46.

43 K. M. Choi, K. J. Shea, *J. Phys. Chem*., 1994, **98**, 3207.

44 K. M. Choi, K. J. Shea, *J. Am. Chem. Soc.,* 1994, **116**, 9052.

45 Y. Wang, N. Herron, *J. Phys. Chem.,* 1987, **91**, 257.

46 C. B. Murray, D. J. Norris and M. G. Bawendi, *J. Am. Chem. Soc*., **1993**, 115, 8706.

47 T. Trindade, P. O'Brien, X. Zhang, *Chem. Mater.,* **1997**, 9, 523.

48 T. Trindade, P. O'Brien, *Adv. Mater*., **1996**, 8, 161.

49 T. Trindade, P. O'Brien, X. Zhang, M. Motevalli, *J. Mater. Chem.*, **1997**, 7, 1011.

50 P. Reiss, *Synthesis of semiconductor nanocrystals in organic solvents.* in: A.L. Rogach, (ed.) *Semiconductor Nanocrystal Quantum Dots: Synthesis Assembly, Spectroscopy, and Applications*. Springer-Verlag; Vienna (Austria), 2008, 35–72.

51 Q. Guo, S. J. Kim, M. Kar, W. N. Shafarman, R. W. Birkmire, E. A Stach, *Nano Lett.,* 2008, **8**, 2982.

52 A. J. Nozik, *Chem. Phys. Lett.*, 2008, **457**, 3.

53 M. C. Beard, R. J. Ellingson. *Laser Photonics Rev.,* 2008, **2**, 377.

54 J. A. McGuire, J. Joo, J. M. Pietryga, R. D. Schaller, V. I. Klimov, *Acc. Chem. Res.*, 2008, **41**, 1810.

55 H. W. Hilhouse, M. C. Beard, *Current Opinion in Colloid & Interface Sci.,* 2009, **14**, 245.

56 T. Yamaguchi, J. Matsufusa, and A. Yoshida, *Jpn. J. Appl. Phys.,* 1992, **31**, L703.

57 Y. Wu, C. Wadia, W. L. Ma, B. Sadtler, A. P. Alivisatos, *Nano Lett.*, 2008, **8**, 2551.

58 B. M. Basol, *Thin Solid Films*, 2000, **361**, 514.

59 C, Eberspacher, C, Fredric, K, Pauls, J. Serra, *Thin Solid Films*, 2000, **387**, 18.

60 M. Kaelin, D. Rudmann, A. N. Tiwari, *Solar Energy*, 2004, **77**, 749.

61 Q. J. Guo, R. Agrawal, H. W. Hillhouse. US Patent Application, US2007/069349.

62 M. G. Panthani, V. Akhavan, B. Goodfellow, J. P. Schmidtke, L. Dunn, A. Dodabalapur, P. F. Barbara and B. A. Korgel, *J. Am. Chem. Soc.*, 2008, **130(49)**, 16770.

63 J. Tang, S. Hinds, S. O. Kelly and E. H. Sargent, *Chem. Mater.*, 2008, **20(22)**, 6906.

64 J. K. J. van Duren, C. Leidholm, A. Pudov, M. R. Robinson, Y. Roussillon. in: T. Gessert, K. Durose, C. Heske, S. Marsillac, T. Wada, (eds). *Symposium on Thin-Film Compound Semiconductor Photovoltaics, 2007*, MRS Spring Meeting; San Francisco, CA, 2007, 259.

65 U. Hivoto, *Jpn. Kokai Tokkyo Koho JP 01*, 1989, **298**, 10.

66 S. K. Haram, K. S. V.Santhanam, M. Numann-Spallar and C. Levy-Clement, *Mater. Res. Soc. Bull.,* 1992, **27**, 1185.

67 S. T. Lakshmikvmar, *Sol. Energy Mater. Sol. Cells*, 1994, **32**, 7.

68 H. Toyoji, Y. Hiroshi,. *Jpn. Kokai Tokkyo Koho JP 02*, 1990, **173**,622,.

69 V. M. Bhuse, P. P. Hankare, K. M. Garadkar, A. S. Khomane, *Mater. Chem. Phys.*, 2003, **80**, 82.

70 W. S. Chen, J. M. Stewart, R. A. Mickelson, *Appl. Phys. Lett.*, 1985, **46**, 1095.

71 C. Levy-Clement, M. Neumann-Spallart, S. S. Haram, K. S. V. Santhanam, *Thin Solid Films,* 1997, **302**, 12.

72 K. B. Shafizade, I. V. Ivanova, M. M. Kaizinets, *Thin Solid Films.,* 1978, **55**, 211.

73 S. K. Haram, K. S. V. Santhanam, M. Numann-Spallar, C. Levy-Clement, *Mater. Res. Soc. Bull.*, 1992, **27**, 1185.

74 V. M. Gracia, P. K. Nair, M. T. S. Nair, *J. Cryst. Growth,* 1999, **203**, 113.

75 M. Lakshmi, K. Bindu, S. Bini, K. P. Vijayakumar, C. S. Kartha, T. Abe, Y. Kashiwaba, *Thin Solid Films,* 2000, **370**, 89.

76 M. Lakshmi, K. Bindu, S. Bini, K. P. Vijayakumar, C. S. Kartha, T. Abe, Y. Kashiwaba, *Thin Solid Films,* 2001, **386**, *127.*

77 R. D. Heyding, R. M. Murray, *Can. J. Chem.,* 1976, **54**, 841.

78 A. L. N. Stevels, F. Jellinek, *Recueil*, 1971, **111**, 273.

79 A. M. Hermann, L. Fabick, *J. Crystal Growth*, 1983, **61**, 658.

80 A. Tonejc, Z. Ogorelec, B. Mestnik, *Appl. Cryst.*, 1975, **8**, 375.

81 S. K. Haram, K. S.V. Santhanam, *Thin Solid Films*, 1994, **238**, 21.

82 S. Massaccesi, S. Sanchez, J. Vedel, *J. Electrochem. Soc.*, 1993, **140**, 2540.

83 N. Nancheva, P. Docheva, N. Djourelov, M. Balcheva, *Mater. Lett.*, 2002, **54**, 169.

84 K. C. Sharma, R. P. Sharma, J. C. Garg, *Ind. J. Pure Appl. Phys.* 1990, **28**, 590.

85 N. R. Pavaskar, C. A. Menzes, A.B.P. Shinha, *J. Electrochem. Soc.*, 1981, **A 35**, 685.

86 Al-Mamun and A. B. M. O. Islam, *Appl. Surface Sci.*, 2004, **238**, 184.

87 H. M. Pathan, C. D. Lokhande, D. P. Amalnerkar and T. Seth, *Applied Surface Science*, 2003, **211**, 48.

88 M. Kemmler, M. Lazell, P. O'Brien, D. J. Otway, J. H. Park and J. R. Walsh, *J. Mater. Sci. : Mater. Electron.*, 2002, **13**, 531.

89 Y. –J. Hsu, C. –M. Hung, Y. –F. Lin, B. –J. Liaw, T. S. Lobana, S. –Y. Lu and C. W. Liu, *Chem. Mater.* 2006, **18**, 3323.

90 S. R. Gosavi, N. G. Deshpande, Y. G. Gudagea, R. Sharma, *Journal of Alloys and Compounds*, 2008, **448**, 344.

91 T. Ohtani, M. Motoki, K. Koh, K. Ohshima, *Mater. Res. Bull.,* 1995, **30**, 1495.

92 Z. P. Qiao, Y. Xie, J. G. Xu, X. M. Liu, Y. J. Zhu, Y. T. Qian, *Can. J. Chem.,* 2000, **78**, 1143.

93 J. J. Zhu, O. Palchik, S. G. Chen, A. J. Gedanken, *Phys. Chem. B,* 2000, **104**, 7344.

94 T. Ohtani, T. Nonaka, M. *J.* Araki, *Solid State Chem.*, 1998, **138**, 131.

95 Y. Xie,; X. W. Zheng,; X. C. Jiang,; J. Lu,; L. Y. Zhu, *Inorg. Chem.,* 2002, **41**, 387.

96 S. Xu, H. Wang, J. J. Zhu, H. Y. Chen, *J. Cryst. Growth,* 2002. **234**, 263.

97 C. Ricardo, L. Cristina, O. Marco, G. Paula, S. Ricardo, R. Rodrigo, *J. Phys. Chem. B,* 2005, **109**, 3212.

98 C. Kaito, A. Nonaka, S. Kimura, N. Suzuki, Y. Saito, *J. Cryst. Growth,* 1998, **186**, 386.

99 M. Dhanam, P. K. Manoj, R. P. Rajeev, *J. Cryst. Growth,* 2005, **280**, 425.

100 Z. Zulkarnain, N. Saravanan, C. L. Tan, *Mater. Lett.,* 2005, **59**, 1391.

101 R. S. Mane, S. P. Kajve, C. D, Lokhande, S. -H. Han, *Vacuum,* 2006, **80**, 631.

102 S. Yang and David F. Kelly, *J. Phys. Chem. B,* 2005, **109(26)**, 12701.

103 A. Segura, J.P. Guesdon, J.M. Besson, A. Chevy, *J. Appl. Phys.*, 1983, **54**, 876.

104 J. Camassel, P. Merle, H. Mathieu and A. Chevy, *Phys. Rev. B,* 1978, **17**, 4718; A. Sequra, J. P. Guesdon, J. M. Besson and A. Chevy, *J. Appl. Phys.*, 1983, **54(2)**, 876.

105 C. Julien, M. Eddrief, K. Kambas, M. Balkanski, *Thin Solid Films*, 1986, **137**, 27.

106 C. Amory, J, C. Bernede and S. Marcillac, *J. Appl. Phys.*, 2003, **94(10)**, 6495.

107 H. Lee, D. H. Kang and L. Tran, *Mater. Sci. Eng., B,* 2005, **119**, 196.

108 I. H. Mutlu, M. Z. Zarbaliyev and F. Aslan, *J. Sol-Gel Sci. Tecnol.*, 2007, **43**, 223.

109 T. Ohtsuka, T. Okamoto, A. Yamada and M. Konagai, *Jpn. J. Appl. Phys.*, 1999, **38**, 668.

110 S. L. Stoll, E. G. Gillan and A. R. Barron, *Chem. Vap. Deposition*, 1996, **2(5)**, 182.

111 Y. C. Huang, Z.Y. Li, W. Y. Uen, S. M. Lan, K. J. Chang, Z. J. Xie, J. Y. Chang, S. C. Wang and J. L. Shen, , *J. Crystal Growth*, 2008, **310**, 1679.

112 M. Bochmann, *Chem. Vap. Deposition*, 1996, **2**, 85.

113 S. L. Stoll, S. G. Bott and A. R. Barron, *J. Chem. Soc., Dalton Trans.,* 1997, 1315.

114 H. J. Gysling, A. A. Wernberg and T. N. Blanton, *Chem. Mater.*, 1992, **4**, 900.

115 I. H. Choi and P. Y. J. Yu, *Appl. Phys.*, 2003, **93**, 4673.

116 J. Y. Cho, H. C. Jeong, K. S. Kim, D. H. Kang, H. K. Kim and I. W. Shim, *Bull. Kor. Chem. Soc.*, 2003, **24**, 645.

117 P. O'Brien, D. J. Otway and J. R. Walsh, Adv. Mater., *Chem. Vap. Deposition*, 1997, **3**, 227.

118 M. Afzaal, D. Crouch and Paul O'Brien, *Mater. Sci. Eng., B*, 2005, **116**, 391.

119 J. H. Park, M. Afzaal, M. Helliwell, M. A. Malik, P. O'Brien and J. Raftery, *Chem. Mater.,* 2003, **15**, 4205.

120 Y. C. Huang, Z. Y. Li, W. Y. Uen, S. M. Lan, K. J. Chang, Z. J. Xie, J. Y. Chang, S. C. Wang and J. L. Shen, *J. Crystal Growth*, 2008,**310**, 1679.

121 N. M. Dimitrijevic and P. V. Kamat, *Langmuir*, 1987, **3(6)**, 1004.

122 N. Revaprasadu, M. A. Malik, J. Carstens and P. O'Brien, *J. Mater. Chem.*, 1999, **9**, 2885.

123 S. Yang and D. F. Kelly, *J. Phys. Chem. B,* 2005, **109(26)**, 12701.

124 H. Tu and D. F. Kelly, *Nano Lett.*, 2006, **6(1)**, 116.

125 S. Yang and D. F. Kelly, *J. Phys. Chem. B,* 2006, **110(27)**, 13430.

126 X. B. Chan and D. F. Kelly, *J. Phys. Chem. B,* 2006, **110(50)**, 25259.

127 S. Yang, H. Wang, W. Fu and D. F. Kelly, *J. Photochemistry and Photobiology A,* 2007, **192**, 159.

128 S. M. Rabchynski, D. K. Ivanou and E. A. Streltsov, *Electrochem. Commun.*, 2004, **6(10)**, 1051.

129 X. Sun, B. Yu, G. Ng, T. D. Nguyen and M. Meyyapan, *Appl. Phys. Lett.*, 2006, **89**, 233121.

130 A. Kuhn, A. Chevy, R. Chevalier, *Phys. Stat. Sol.*, 1975, **A31**, 469.

131 K. Ueno, N. Takeda, K. Sasaki, A. Koma, *Appl. Surf. Sci.*, 1997, **38**, 113.

132 V. Chikan and D. F. Kelly, *Nano Lett.*, 2002, **2(2)**, 141.

133 K. Jamshidi-Ghaleh and M. Karimi, *Optics Commun.*, 2008, **281**, 5561.

134 A. Segura, J. Bourier, M. V. Andres, F. J. Manjon, V. Munoz, *Phys. Rev.* B, 1997, **56**, 4075.

135 S. Shigetomi, T. Ikari and H. Nakashima, *J. Lumin.*, 1998, **79**, 79.

136 V. Capozzi, *Phys. Rev. B*, 1981, **23(2)**, 836.

137 G.B. Abdullaev, L. A. Kulevskii, A. M. Prokhorov, A. D. Sovel'ev, E. Yu. Solaev, V. V. Smirnov, *JETP Lett.*, 1972, **16**, 90.

138 A. Cingolani, A. Minafra, P. Tontalo and C. Paorici, *Phys. Stat. Solid*, 1971, **4**, K83.

139 H. Tobioka, Y. Mitsumori, F. Minami and A. Hasegawa, *J. Lumin.*, 2001, **94-95**, 601.

140 E. G. Gillan and A. R. Barron, *Chem. Mater.,* 1997, **9**, 3037.

141 E. G. Gillan, S. G. Bott and A. R. Barron, *Chem. Mater.,* 1997, **9**, 796.

142 J.-H. Park, M. Afzaal, M. Helliwell, M. A. Malik, P. O'Brien and J. Raftery, *Chem. Mater.,* 2003, **15**, 4205.

143 T. L. Ng, N. Maung, G. Fan, I. B. Poole, J. 0. Williams, A. C. Wright, D. E. Foster and D. J. Cole-Hamilton, *Chem. Vap. Deposition*, 1996, **2(5)**, 185.

144 T. P. Gujar, V. R. Shinde, J.-W. Park, H. K. Lee, K. –D. Jung, O. –S. Joo, *Electrochemica Acta,* 2008, **54**, 829.

145 H. Peng, S. Meister, C. K. Chan, X. F. Zhang and Y. Cui, *Nano Lett.*, 2007, **7(1)**, 199.

146 I. H. Mutlu, M. Z. Zarbaliyev and F. Aslan, *J. Sol-Gel Sci. Technol.*, 2009, **50**, 271

147 S. L. Stoll, E. G. Gillan and A. R. Barron, *Chem. Vap. Deposition,* 1996, **2(5)**, 182.

148 K. Allakhverdiev, J. Hagen, and Z. Salaeva, *Phys. Status Solidi*, 1997, **163**, 121.

149 U. K. Gautam, S. R. C. Vivekchand, A. Govindaraj, G. U. Kulkarni, N. R. Selvi and C. N. R. Rao, *J. Am. Chem. Soc.*, 2005, **127**, 3658.

150 K. Ramanathan, M. A. Contreras, C. L. Perkins, S. Asher, F. S. Hasoon, J. Keane, D. Young, M. Romero, W. Metzger, R. Noufi, J. Ward, and A. Duda, *Prog. Photovolt: Res. Appl.,* 2003,**11**, 225.

151 H.-W. Schock and R. Noufi, *Prog. Photovolt.: Res. Appl.,* 2000, **8**, 151.

152 T. Kojima, T. Koyanagi, K. Nakamura, T. Yanagisawa, K. Takahisa, M. Nishitani, and T. Wada, *Sol. Energy Mater. Sol. Cells,* 1998, **50**, 87.

153 R. W. Birkmire, *Sol. Energy Mater. Sol. Cells* 2001, **65**, 17.

154 J. M. Merino, J. L. Martın de Vidales, S. Mahanty, R. Dıaz, F. Rueda, and M. Leon, *J. Appl. Phys.,* 1996, **80**, 5610.

155 B. J. Stanbery, *Critical Reviews in Solid State and Materials Sciences*, 2002, **27(2)**, 73.

156 R. W. Birkmire and E. Eser, *Annu. Rev. Mater. Sci.,* 1997, **27**, 625.

157 D. Schmid, M. Ruckh, F. Grunwald, and H. W. Schock, *J. Appl. Phys.,* 1993, **73**, 2902.

158 I. M. Kötschau and H. W. Schock, *J. Phys. Chem. Solids,* 2003, **64**, 1559.

159 J. A. M. AbuShama, S. Johnston, T. Moriarty, G. Teeter, K. Ramanathan, and R. Noufi, *Prog. Photovolt: Res. Appl.,* 2004, **12**, 39.

160 D. L. Young, J. Keane, A. Duda, J. A. M. AbuShama, C. L. Perkins, M. Romero, and R. Noufi, *Prog. Photovolt: Res. Appl.,* 2003, **11**, 535.

161 J. Klaer, J. Bruns, R. Henninger, K. Siemer, R. Klenk, K. Ellmer, and D. Bräunig, *Semicond. Sci. Technol.,* 1998, **13**, 1456.

162 T. Negami, Y. Hashimoto, and S. Nishiwaki, *Sol. Energy Mater. Sol. Cells,* 2001, **67**, 331.

163 Y. Hagiwara, T. Nakada, and A. Kunioka, *Sol. Energy Mater. Sol. Cells,* 2001, **67**, 267.

164 S. Chaisitsak, A. Yamada, and M. Konagai, *Jpn. J. Appl. Phys.,* 2002, **41**, 507.

165 T. Nakada, and M. Mizutani, *Jpn. J. Appl. Phys.,* 2002, **41**, L165.

166 U. Rau, M. Schmidt, A. Jasenek, G. Hanna, and H. W. Schock, *Sol. Energy Mater. Sol. Cells,* 2001, **67**, 137.

167 S. Siebentritt, *Thin Solid Films,* 2002, **403–404**, 1.

168 J. Tringe, J. Nocerino, R. Tallon, W. Kemp, W. Shafarman, and D. Marvin, *J. Appl. Phys.,* 2002, **91**, 516.

169 A. Jasenek, U. Rau, K. Weinert, I. M. K¨otschau, G. Hanna, G. Voorwinden, M. Powalla, H. W. Schock, and J. H. Werner, *Thin Solid Films,* 2001, **387**, 228.

170 M. Yamaguchi, *J. Appl. Phys.,* 1995, **78**, 1476.

171 S. Kawakita, M. Imaizumi, M. Yamaguchi, K. Kushiya, T. Ohshima, H. Itoh, and S. Matsuda, *Jpn. J. Appl. Phys., Part 2,* 2002, **41**, L797.

172 M. Kemell, M. Ritala and M. Laskela, *Critical Reviews in Solid State and Material Sciences*, 2005, 30(1), 1.

173 R. W. Birkmire and E. Eser, *Annu. Rev. Mater. Sci.* 1997, **27**, 625.

174 R. Caballero and C. Guillen, *Thin Solid Films,* 2002, **403–404**, 107; M. Marudachalam, H. Hichri, R. Klenk, R. W. Birkmire, W. N. Shafarman, and J. M. Schultz, *Appl. Phys. Lett.,* 1995, **67**, 3978; M. Klenk, O. Schenker, V. Alberts, and E. Bucher, *Semicond. Sci. Technol.,* 2002, **17**, 435.

175 A. M. Gabor, J. R. Tuttle, D. S. Albin, M. A. Contreras, and R. Noufi, *Appl. Phys. Lett.,* 1994, **65**, 198.

176 S. Chaisitsak, A. Yamada, and M. Konagai, *Jpn. J. Appl. Phys.,* 2002, **41**, 507.

177 W. E. Devaney, W. S. Chen, J. M. Stewart, and R. A. Mickelsen, *IEEE Trans. Electron Dev.,* 1990, **37**, 428.

178 A. M. Hermann, C. Gonzalez, P. A. Ramakrishnan, D. Balzar, N. Popa, B. Rice, C. H. Marshall, J. N. Hilfiker, T. Tiwald, P. J. Sebastian, M. E. Calixto, and R. N. Bhattacharya, *Sol. Energy Mater. Sol. Cells,* 2001, **70**, 345.

179 P. Berwian, A.Weimar, and G.M¨uller, *Thin Solid Films,* 2003, **431–432**, 41.

180 C. Guillen and J. Herrero, *Sol. Energy Mater. Sol. Cells,* 2002, **73**, 141.

181 S. Bandyopadhyaya, S. Roy, S. Chaudhuri, and A. K. Pal, *Vacuum,* 2001, **62**, 61; J. Bekker, V. Alberts, A.W. R. Leitch, and J. R. Botha, *Thin Solid Films,* 2003, **431–432**, 116.

182 M. C. Artaud, F. Ouchen, L. Martin, and S. Duchemin, *Thin Solid Films,* 1998, **324**, 115.

183 S. Duchemin, M. C. Artaud, F. Ouchen, and J. Bougnot, *J. Mater. Sci.: Mater. Electron.,* 1996, **7**, 201.

184 P. A. Jones, A. D. Jackson, P. D. Lickiss, R. D. Pilkington, and R. D. Tomlinson, *Thin Solid Films,* 1994, **238**, 4.

185 J. McAleese, P. O'Brien, and D. J. Otway, *Chem. Vap. Deposition,* 1998, **4**, 94.

186 J.-H. Park, M. Afzaal, M. Kemmler, P. O'Brien, D. J. Otway, J. Raftery, and J. Waters, *J. Mater. Chem.,* 2003, **13**, 1942.

187 M. Afzaal, D. J. Crouch, P. O'Brien, J. Raftery, P. J. Skabara, A. J. P. White, and D. J. Williams, *J. Mater. Chem.,* 2004, **14**, 233.

188 K. K. Banger, M. H.-C. Jin, J. D. Harris, P. E. Fanwick, and A. F. Hepp, *Inorg. Chem.,* 2003, **42**, 7713.

189 J. A. Hollingsworth, K. K. Banger, M. H.-C. Jin, J. D. Harris, J. E. Cowen, E.W. Bohannan, J. A. Switzer,W. E. Buhro, and A. F. Hepp, *Thin Solid Films*, 2003, **431–432**, 63.

190 I. H. Choi and P. Y. Yu, *Phys. Rev.* B*,* 2003, **68**,165339.

191 I. H. Choi and P. Y. Yu*, J. Appl. Phys.*, 2003, **93**, 4673.

192 I. H. Choi and P. Y. Yu, *Phys. Stat. Solid*, 2005, **(b) 242**, 2813.

193 I. H. Choi and D.H. Lee, *Thin Solid Films*, 2007, **515**, 4861.

194 I. H. Choi and P. Y. Yu, *Current Appl. Phys.*, 2009, **9**, 151.

195 H. W. Hillhouse and M. C. Beard, *Current Opinion in Colloid & Interface Sci.,* 2009, **14**, 245.

196 M. A. Malik, P. O'Brien and N. Revaprasadu, *Adv. Mater.*, 1999, **11**, 1441.

197 S. L. Castro, S. G. Bailey, R. F. Rafello, K. K. Banger and A. F. Hepp, *Chem. Mater.*, 2003, **15**, 3142.

198 J. Tang, S. Hinds, S. O. Kelly and E. H. Sargent, *Chem. Mater.*, 2008, **20(22)**, 6906.

199 P. M. Allen and M. G. Bawendi, *J. Am. Chem. Soc.*, 2008, **130**, 9240.

200 M. G. Panthani, V. Akhavan, B. Goodfellow, J. P. Schmidtke, L. Dunn, A. Dodabalapur, P. F. Barbara and B. A. Korgel, *J. Am. Chem. Soc.*, 2008, **130(49)**, 16770.

201 D. B. Mitzi, M. Yuan, W. Liu, A. J. Kellock, S. J. Chey, L. Gignac, and A. G. Schrott, *Thin Solid Films*, 2009, **517**, 2158.

202 A. Schmidpeter, R. Bröhm, and M. H. Groeger*, Angew. Chem.,* 1964, **76**, 860.

203 D. Cupertino, D. J. Birdsall, A. M. Z. Slawin and J. D. Woolins, *Inorg. Chim. Acta*, 1999, **290**, 1; D. Cupertino, R. Keyte, A. M. Z. Slawin, D. J. Williams and J. D. Woolins, *Inorg. Chem.*, 1996, **35**, 2695; D. J. Birdsall, A. M. Z. Slawin and J. D. Woolins, *Polyhedron*, 2001, **20**, 125.

204 D. C. Cupertino, R. W. Keyte, A. M. Z. Slawin and J. D. Woolins, *Polyhedron*, 1999, **18**, 707; T. Q. Ly and J. D. Woolins, *Coord. Chem. Rev.*, 1998, **176**, 451.

205 M. Afzaal, S. M. Aucott, D. Crouch, P, O'Brien, J. D. Woolins and J. H. Park, *Chem. Vap. Deposition*, 2002, **8**, 187; M. Afzaal, D. Crouch, M. A. Malik, M. Motevalli, P. O'Brien, J. –H. Park, and J. D. Woolins, *Eur. J. Inorg. Chem.*, 2004, 171; M. Afzaal, D. Crouch, P, O'Brien, *Mater. Sci. Engineering B*, 2005, **116**, 391.

206 M. Afzaal, D. J. Crouch, P. O'Brien, J. Raftery, P. J. Skabara, A. J. P. White and D. J. Williams, *J. Mater. Chem.*, 2004, **14**, 233; M. Afzaal, S. M. Aucott, D. Crouch, P. O'Brien, J. D. Woolins and J. H. Park, *Adv. Mater.*, 2002, **14**, A187.

207 G. Briand, T. Chivers and M. Parvez, *Angew. Chem.,* 2002, **41**, 3468.

208 T. Chivers, D. J. Eisler, J. S. Ritch, H. M. Tuononen, *Angew. Chem.,* 2005, **44**, 4953.

209 T. Chivers, D. J. Eisler and J. S. Ritch, *Dalton Transactions*, 2005, 2675.

210 S. S. Garje, J. S. Ritch, D. J. Eisler, m. Afzaal, P, O'Brien and T. Chivers, *J. Mater. Chem.*, 2006, **16**, 966.

211 M. V. kudchadker, R. A. Zingaro and K. J. Irgolic, *Can. J. Chem.*, 1968, **46**, 1415.

212 V. Krishnan and R. A. Zingaro, *Inorg. Chem.*, 1969, **8**, 2337.

213 V. Krishnan and R. A. Zingaro, *J. Coord. Chem.*, 1971, **1**, 1.

214 H. Liu, N. A. G. Bandeira, M. J. Calhorda, M. G. B. Drew, V. Felix, J. Novosad, F.F. D. Biani and P. Zanello, *J. Organomet. Chem.*, 2004, **689**, 2808.

215 C. W. Liu, I. J. Shang, C. M. Hung, C. J. Wang and T. C. Keng, *J. Chem. Soc. Dalton Trans.*, 2002, 1974.

216 C. W. Liu, H. C. Chen, J. C. Wang and T. C. Keng, *Chem. Comm.,* 1998, 1831.

217 C. W. Liu, T. S. Lobana, B. K. Santra, C. M. Hung, H. Y. Liu, B. J. Liaw and C. J. Wang, *Dalton Transactions*, 2006, 560.

218 B. K. Santra, C. M. Hung, B. J. Liaw, C. J. Wang and C. W. Liu, *Inorg. Chem.*, 2004, **43**, 7570.

219 C. W. Liu, H. C. Haia, C. M. Hung, B. K. Santra, B. J. Liaw, Z. Lin and C. J. Wang, *Inorg. Chem.*, 2004, **43**, 4464.

220 I. P. Gray, A. M. Z. Slawin and J. D. Woolins, *Polyhedron*, 2001, **20**, 125.

221 M. A. Malik, C. Byrom, P. O'Brien and M. Motevalli, *Inorg. Chim. Acta*, 2002, **338**, 245.

222 M. N. Gibbons, D. B. Sowerby, C. Silvestru and I. Haiduc, *Polyhedron*, 1996, **15**, 4573.

223 C. C. Landry, A. Hynes, A. R. Barron, I. Haiduc, C. Silvestru, *Polyhedron*, 1996, **15**, 391.

224 R. G. Cavell, B. Creed, L. Gelmini, D. J. Law, R. McDonald, A. R. Sanger and A. Somogyvari, *Inorg. Chem.*, 1998, **37**, 757.

225 S. N. Olafsson, T. N. Peterson and P. Andersen, *Acta Chem. Scandinavica*, 1996, **50**, 745.

226 W. Kutchen, J. Metten, A. Judet, *Chemische Berichte-Recueil*, 1964, **97**, 2306; W. Kutchen, B. Knop, *Angew. Chem.,* 1965, **4**, 244; W. Kutchen, H. Hartel, *Angew. Chem.,* 1969, **8**, 89.

227 A. Muller, V. V. K. Rao and P. Christphliemk, *J. Inorg. Nuclear Chem.*, 1974, **36**, 472; A. Muller, P. Christphliemk and V. V. K. Rao, *Chem. Ber.*, 1971, **104**, 1905.

228 M. J. Pilkington, A. M. Z. Slawin, D. J. Williams, J. D. Woolins, *Polyhedron*, 1991, **10**, 2641.

229 R. P. Davies and M. G. Martinelli, *Inorg. Chem.*, 2002, **41**, 348.

230 R. P. Davies, C. V. Francis, A. P. S. Jurd, M. G. Martinelli, A. J. P. White and D. J. Williams, *Inorg. Chem.*, 2004, **43**, 4802.

231 D. Cupertino, R. Keyte, A. M. Z. Slawin, D. J. Williams and J. D. Woolins, *Inorg. Chim. Acta*, 1999, **290**, 1.

232 R. A. Benkeser, K. M. Foley, J. B. Grutzner and W. E. Smith, *J. Am. Chem. Soc.*, 1970, 92; R. A. Benkeser, *Acc. Chem. Res.*, 1971, **4**, 94.

CHAPTER 2

EXPERIMENTAL

2.1 Chemicals

Chlorodiisopropylphosphine (97%), triethylsilane (98%), triethylamine (97%), Se powder ~ 100 mesh (99.5%), indium (III) chloride (99.99%), gallium (III) chloride (99.99%), copper(II) chloride, copper(I) chloride (99.99%), methanol (99.9%), hexadecylamine (90%, technical grade 90%), tri-n-octylphosphine oxide (90%, technical grade), trioctylphosphine, octadecence (90%, technical grade) and oleylamine (90%) were obtained from Sigma-Aldrich Chemical Company and used as received. Solvents toluene and methanol were dried by distillation over sodium/benzophenone and calcium hydride prior to use.

2.2 Experimental

Standard Schlenk line techniques were used to carry out synthetic reactions under an inert atmosphere of nitrogen. Solid air sensitive chemicals ($GaCl_3$) were handled inside a glove box under an atmosphere of dry nitrogen. The glassware was flame dried along with evacuation followed by purging inert gas to remove moisture before each experiment. ^{1}H NMR spectra were obtained using a Bruker AC300 FT-NMR spectrometer. Mass spectra were recorded on a Kratos Concept 1S instrument. Elemental analysis was performed by the University of Manchester micro-analytical facility. TGA measurements were carried out using a Seiko SSC/S200 thermal analyzer under a heating rate of 10 °C min^{-1} under nitrogen. Melting points were recorded using a Stuart melting point apparatus and were uncorrected.

2.3 Synthesis of $[HNEt_3]^+[^iPr_2PSe_2]^-$ (1)

(1) was synthesized as per the procedure reported in the literature with a slight modification.[1] Chlorodiisopropylphosphine, $^iPr_2PCl$ (4.8 mL, 30 mmol) and triethylsilane, $HSiEt_3$ (9.6 mL, 60 mmol) were dissolved in 150 mL cold dry toluene under nitrogen followed by triethylamine, NEt_3 (10.4 mL, 80 mmol). The mixture was stirred for 6 hours at room temperature forming a white cloudy precipitate. Grey Se powder (4.3 g. 60 mmol) was added to the solution and further refluxed for 20 hours, leading to a dark red solution and white precipitate. The white precipitate was filtered off. The resulting solution was reduced to ~ 50 ml and kept at 0 °C to produce pale yellow needle-like crystals.

The crystals were filtered and washed with cold hexane. Yield, 10 g (89%). Elemental analysis, % (Found: C, 38.7; H, 8.1; N, 3.6; P, 8.3; Calc: C, 38.2; H, 8.0; N, 3.7; P, 8.2). ^{1}H NMR (δ, $CDCl_3$, 300 MHz): 3.21 ppm (6H, q, J = 7.3 Hz, 3 x $C\underline{H}_2CH_3$), 2.14 ppm (4H, dsep, $^3J_{HH}$ = 6.7 Hz, $^2J_{PH}$ = 5.5 Hz, 2 x $C\underline{H}(CH_3)_2$), 1.33 ppm (9H, t, J = 7.3 Hz, 3 x $CH_2C\underline{H}_3$), 1.18 ppm (12H, dd, $^3J_{HH}$ = 6.7 Hz, $^3J_{PH}$ = 19.1 Hz, 2 x $CH(C\underline{H}_3)_2$), 13C NMR (100 MHz, $CDCl_3$): 8.72 ppm ($CH_2\underline{C}H_3$), 17.77 ppm ($CH(\underline{C}H_3)_2$), 33.65 ppm & 34.14 ppm ($\underline{C}H(CH_3)_2$), 45.97 ppm ($\underline{C}H_2CH_3$); Mass (APCI), most important fragments include [$HNEt_3$] *m*/*z* 102, [$^iPr_2PSe_2$] *m*/*z* 275.

2.4 Synthesis of precursors

Diisopropyldiselenophosphinato- complexes of indium(III), gallium(III) and copper(I) were used as precursors in this study. Synthesis of the complexes was carried out in accordance with the standard procedure reported by O'Brien *et al.*[2]

2.4.1 Synthesis of copper precursor [$Cu_4(^iPr_2PSe_2)_4$] (2)

In a typical experiment, the solution of CuCl (0.99 g, 10 mmol) in 20 mL MeOH was added drop wise to a solution of [$HNEt_3$][$^iPr_2PSe_2$] (3.77 g, 10 mmol) in 100 ml of MeOH. The mixture was stirred for 1 h at room temperature under atmospheric pressure, forming a yellow precipitate, which was filtered, washed with MeOH and recrystallized in dichloromethane to obtain dark yellow crystals of 1. Yield: 1.32 g (72%). m.p. 230–235 °C (uncorrected). Elemental analysis, % (found: C, 21.9; H, 4.3; P, 9.0; calc. for $C_{24}H_{56}P_4Se_8Cu_4$: C, 21.3; H, 4.2; P, 9.1). ^{1}H NMR (δ, 300 MHz, $CDCl_3$), 1.35 ppm (6H, dd, 12H, $^3J_{HH}$ = 6.7 Hz, $^3J_{PH}$ = 19.2 Hz, $CH(C\underline{H}_3)_2$), 2.44 ppm (2H, dsep, $^3J_{HH}$ = 6.7 Hz, $^2J_{PH}$ = 6.7 Hz, 2 x $C\underline{H}(CH_3)_2$).

2.4.2 Synthesis of indium precursor $In(^iPr_2PSe_2)_3$ (3)

Precursor (3) was synthesized by following the above mentioned procedure. However, $InCl_3$ (0.736 g, 3.33 mmol) was used instead of $CuCl_2$ to obtain yellow crystals (2). Yield, 2.7 g (87 %). M.p. 183 °C (uncorrected). Elemental analysis, % (found: C, 23.1; H, 4.4; P, 10.2; In, 12.0; calc. for $C_{18}H_{42}P_3Se_6In$: C, 23; H, 4.5; P, 9.9; In 12.2). ^{1}H NMR (δ, 300 MHz, $CDCl_3$),

1.37 ppm (36H, dd, , $^{3}J_{HH}$ = 6.7 Hz , $^{3}J_{PH}$ = 20.4, 6 x $CH(C\underline{H}_3)_2$), 2.24 ppm (6H, dsep, , $^{3}J_{HH}$ = 6.7 Hz, $^{2}J_{PH}$= 4.4 Hz, 6 x $C\underline{H}(CH_3)_2$).

2.4.3 Synthesis of gallium precursor $Ga(^{i}Pr_2PSe_2)_3$ (4)

The same procedure was employed for the synthesis of precursor (4); however, $GaCl_3$ (0.586 g, 3.33 mmol) was used instead of $CuCl_2$ to obtain yellow crystals (2). Yield, 2.11 g (72 %). M.p. 180 °C (uncorrected). Elemental analysis, % (found: C, 24.2; H, 4.8; P, 10.1; Ga, 7.6 %; calc. for $C_{18}H_{42}P_3Se_6Ga$: C, 24.2; H, 4.7; P, 10.4; Ga 7.8%; ^{1}H NMR (δ, 300 MHz, $CDCl_3$), 1.31 ppm (36H, dd, , $^{3}J_{HH}$ = 6.7 Hz , $^{3}J_{PH}$ = 20.2, 6 x $CH(C\underline{H}_3)_2$), 2.29 ppm (6H, dsep, , $^{3}J_{HH}$ = 6.7 Hz, $^{2}J_{PH}$= 4.7 Hz, 6 x $C\underline{H}(CH_3)_2$).

2.5 Deposition of thin films by AACVD

The substrates used for deposition of thin film materials were glass slides (1 x 3 cm). They were thoroughly cleaned to remove any possible contamination. The method used for cleaning the substrates involved placing the slides in dilute nitric acid (50%) overnight, washing with distilled water, washing with acetone, rinsing with distilled water, sonication in distilled water for 10 minutes and finally drying in oven.

In a typical deposition experiment, 0.02M of the precursor solution in 15 mL toluene was added in a two-necked 100 mL round-bottom flask with a gas inlet that allowed the carrier gas (argon) to pass into the solution and aid transport of the aerosol. This flask was connected to the reactor tube by a piece of reinforced tubing. The argon flow rate was controlled by a Platon flow gauge. Six glass substrates (approx. 1 x 3 cm) were placed inside the reactor tube, placed in a Carbolite furnace. The precursor solution in a round-bottom flask was kept in a water bath above the piezoelectric modulator of a PIFCO ultrasonic humidifier (Model No. 1077). The aerosol droplets of the precursor thus generated were transferred into the hot-wall zone of the reactor by carrier gas. Both the solvent and the precursor underwent thermolysis as the precursor vapors reached the heated substrate surface where thermally induced reactions and film deposition took place.

All AACVD experiments for the deposition of thin films of semiconductor materials were performed using an improvised AA-CVD Kit. Figure 2.1 illustrates schematic diagram of the AACVD kit used in this work.

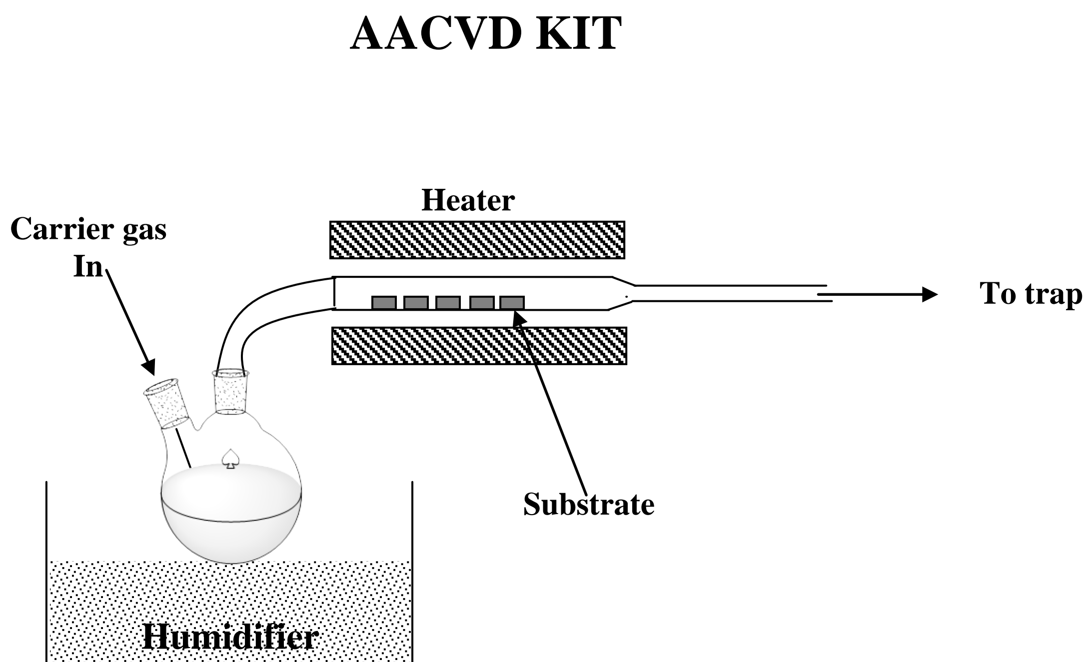

Figure 2.1 Schematic of an AACVD kit

2.6 Synthesis of nanoparticles

A colloidal approach for synthesis of nanoparticles was used in this work which involved thermolysis of precursors at desired temperatures. Rapid injection of precursors (suspended in a suitable solvent e.g. TOP) into the coordinating solvent results in a burst of nucleation. The small nuclei then grow in size till their surface is capped by the coordinating solvent, thus inhibiting further growth of the nanocrystals. Growth temperature and reaction duration were judiciously controlled as they have significant effect on the size and morphologies of the nanoparticles.

2.6.1 Growth of indium selenide nanoparticles

In a typical procedure for the synthesis of InSe nanoparticles, 15 g hexadecylamine (HAD) and 5 ml of octadecene (ODE) were degassed for 1h

in a three-necked flask fitted with a septum, condenser and thermometer. Nitrogen was flushed thrice through the system and the contents of the flask were heated under nitrogen to maintain the desired reaction temperature (270 °C in this case). 0.5 mmol of $[In(^iPr_2Pse_2)_3]$ were suspended in 4 ml TOP under nitrogen and injected into HAD/ODE in the flask at 270 °C). The contents of the flask turned reddish brown indicating formation of InSe nanoparticles. Temperature initially dropped to 255 °C was re-maintained at 270 °C and the reaction continued for a further 2 hours allowing growth of nanocryatals after which the heating was removed and reaction mixture allowed to cool to 60 °C. Excess anhydrous methanol was then added and precipitates formed were separated through centrifugation. The clear supernatant liquid was discarded and a reddish-brown material thus obtained was washed thrice with 10 ml anhydrous methanol, and dispersed in 3 ml dry toluene under nitrogen for further analysis.

2.6.2 Attempted growth of gallium selenide nanoparticles

The same procedure was applied for the synthesis of gallium selenide nanoparticles; however 0.5 mmol of $[Ga(^iPr_2PSe_2)_3]$ was used. The reaction mixture turned pale blue after 2 hours and was worked up as described before.

2.6.3 Growth of copper selenide nanoparticles

The above mentioned procedure was used to grow copper selenide; however copper complex (1) was used as precursor. The colour of the reaction mixture turned dark brown after injection. After 2 hours of reaction, copper selenide nanoparticles were obtained by work up as described above.

2.6.4 Growth of copper indium diselenide nanoparticles

In a typical procedure for the synthesis of $CuInSe_2$ nanoparticles, 15 g hexadecylamine (HAD) and 5 ml of octadecene (ODE) were degassed for 1h in a three-necked flask fitted with a septum, condenser and thermometer. Nitrogen was flushed thrice through the system and the contents of the flask were heated under nitrogen to maintain the desired reaction temperature (120-210 °C). 0.1 mmol of $[Cu_4(^iPr_2Pse_2)_4]$ and 0.4 mmol of $[In(^iPr_2Pse_2)_3]$ were suspended in 4 ml TOP under nitrogen and injected into HAD/ODE in

the flask at desired temperature. The contents of the flask immediately turned dark brown indicating formation of ternary $CuInSe_2$. The temperature initially dropped and was re-maintained at desired level. The reaction was continued for a further 30 minutes allowing growth of nanocrystals after which the heating was removed and the reaction mixture allowed to cool to 60 °C. Excess anhydrous methanol was then added and the precipitates formed were separated through centrifugation. Clear supernatant liquid was discarded and the dark brown semiconductor material thus obtained was washed thrice with 10 ml anhydrous methanol, dispersed in 3 ml dry toluene and centrifuged again. Toluene suspension obtained after centrifugation was stored under nitrogen for further analysis.

2.6.5 Growth of copper gallium diselenide nanoparticles

The above mentioned procedure was followed for the growth of $CuGaSe_2$ chalcogenide nanocrystals except that 0.4 mmol of $Ga(^iPr_2PSe_2)_3]$ were used instead of $In(^iPr_2Pse_2)_3]$ and the reaction was carried out at 250 °C.

2.6.6 Growth of copper indium gallium diselenide (CIGS) nanoparticles

The growth of the CIGS nanocrystals was carried out by the same procedure as described above for $CuInSe_2$ nanoparticles. However, different quantities of the indium and gallium precursors were used to obtain various stoichiometric combinations of CIGS nanomaterials. 0.2 mmol each of $[In(^iPr_2PSe_2)_3]$ and $Ga(^iPr_2PSe_2)_3]$ were used for $CuIn_{0.7}Ga_{0.3}Se_2$, 0.2 mmol of $[In(^iPr_2PSe_2)_3]$ and 0.4 mmol of $Ga(^iPr_2PSe_2)_3]$ were used for $CuIn_{0.5}Ga_{0.5}Se_2$ whereas 0.2 mmol of $[In(^iPr_2PSe_2)_3]$ and 0.5 mmol of $Ga(^iPr_2PSe_2)_3]$ were used for obtaining $CuIn_{0.4}Ga_{0.6}Se_2$ nanomaterials. The reaction temperature for growth of CIGS nanocrystals was maintained at 250 °C.

2.7 Characterization techniques for thin films and nanoparticles

The deposited films were then subjected to characterization by powder X-ray diffraction, scanning electron microscopy (SEM), and energy dispersive X-ray (EDX) analysis, whereas the nanoparticles were characterized by UV-Vis absorption spectrophotometry, photoluminescence measurements (where

possible), powder X-ray diffraction (XRD), transmission electron microscopy and energy dispersive X-ray (EDX) analysis.

2.7.1. UV-Vis optical absorption spectroscopy

Direct band gaps (Eg) of the nanoparticles were determined by UV-Vis absorption spectroscopy. A Heλios-Beta spectrophotometer was used to record the UV-Vis optical absorption spectra of the nanoparticles. The linear dependence of α^2 vs. hν (where α is the absorption coefficient) is indicative of the direct bandgap materials. Extrapolation of the linear region of the absorption plots of α^2 vs. hν provided band gap values.

2.7.2. Photoluminisence (PL) studies

Fluorescence spectrophotometer was used to record optical emission spectra of the nanoparticles.

2.7.3. Powder X-ray Diffraction

Thin films and nanoparticles synthesized in this work were characterized by using powder XRD diffraction studies. In the case of nanoparticles, films of nanocrystals were deposited onto glass substrates by simple drop cast method. Bruker AXS D8 diffractometer using monochromated Cu-Kα radiations was used to record XRD patterns. The samples were mounted flat and scanned from 20 to 80 2-theta range with a step size of 0.05 and a count rate of 9 seconds. The diffraction patterns obtained were then compared to the documented patterns in the ICDD database using EVA software package.

The d-spacings were calculated Bragg's law:

$$n\lambda = 2d\sin\theta$$

Where λ is the wavelength of the radiation used, n is an integer, d is the perpendicular spacing between the lattice planes in the crystal lattice and θ is the complement of the angle of incidence of the X-ray beam.

Crystallite sizes (normal to planes *hkl*) were estimated using the Scherrer formula:

Crystallite size (nm) = $0.9\ \lambda / B \cos \theta_B$

Where λ is the wavelength of the radiation used, and B is the broadening parameter with reference to a standard sample, defined by $B = (B_M^2 - B_S^2)^{0.5}$,

where B_M and B_S are the full width at half maximum (FWHM) of peaks in radians for the measured and standard samples, respectively. Errors were estimated to be of the order ± 5%.

2.7.4 Scanning electron microscopy (SEM) and energy dispersive X-ray (EDX) analysis

SEM was performed using a Philips XL 30 FEGSEM and EDX analysis was carried out using a DX4 instrument. To avoid charging of the sample by the electron beam, thin films were carbon coated using Edwards E-306A coating system before carrying out SEM and EDX analysis.

2.7.5 Transmission electron microscopy (TEM)

TEM samples were prepared by evaporating a dilute toluene solution of the nanoparticles on carbon coated copper grids (S166-3, Agar Scientific) and Philips CM200 transmission electron microscope (TEM), operating at 200 kV was used to obtain TEM images of the nanoparticles. High resolution Transmission Electron Microscopy (HR-TEM) images of the samples were obtained using Philips Tecnai F30 FEG – TEM microscope operating at 300 kV.

References

1 C. Q. Nguyen, A. Adeogun, M. Afzaal, M. A. Malik and P. O'Brien, *Chem. Commun.*, 2006, 2179.

2 C. Q. Nguyen, A. Adeogun, M. Afzaal, M. A. Malik and P. O'Brien, *Chem. Commun.*, 2006, 2182.

CHAPTER 3

RESULTS AND DISCUSSION

3.1 Results and discussion

Provision of sustainable and environmentally benign energy may be regarded as the most important technical challenge faced by humanity today. At present, power generation in almost all the countries is predominantly dependant on fossil fuels, whereas nuclear and large hydroelectric power plants are other leading electricity generation technologies. However, a surge in oil prices during the current decade and environmental concerns about emission of greenhouse gases by burning of fossil fuels, as well as issues limiting widespread use of nuclear and hydroelectric technologies, have led the energy planners to focus more on development of alternative energy technologies.

Solar photovoltaics (PV), has the potential to provide reliable and sustainable energy solutions for the 21st century. Furthermore, PV is environmentally benign as it has no associated environmental footprints. Therefore, substantial research efforts have been dedicated for development and wide spread use of these technologies. However, despite enormous potential of solar energy, one major daunting factor which limits the widespread use of this technology is the relatively higher cost per peak watt hour of electricity produced. Silicon based PV technologies currently dominate global PV market. Despite remarkable enhancement in module efficiencies and the cost reductions, cost per peak Watt of electricity generated from silicon based PV technology is not low enough to offer economically viable electricity for wide spread use.

Material cost for silicon wafers is approximately half of the total cost of PV cells and modules. Furthermore, Si cells and modules are almost approaching theoretical limits in power conversion efficiencies because of the Shockley-Queisser effect[1] and a tremendous boost in PV manufacturing during recent years has now outstripped the supply of silicon. Therefore, new semiconducting materials are being explored which might offer better efficiencies and reduced cost because of lesser material requirement. Cadmium telluride (CdTe), copper indium diselenide (CIS) or copper indium gallium diselenide (CIGS) are a few examples of such compound semiconductors. These semiconductors can be deposited on low cost substrates such as glass and owing to high solar absorption coefficients (greater than 10^5/cm) of these materials, film having thickness typically less than a micron are required.

Therefore, 100-1000 times lesser materials are required for PV technologies based on these semiconductors than conventional silicon wafers based PV technologies.

By virtue of their high efficiency, photo-irradiation stability, lower cost, lesser material requirements, shorter energy payback times and flexible applicability, I-III-VI_2 chalcopyrite semiconductors are materials of choice as absorbers in solar photovoltaic applications. $CuInSe_2$, $CuInS_2$, $CuGaSe_2$ with direct optical band gaps of 1.0, 1.5, and 1.7 eV, respectively and $CuIn_{(1-x)}Ga_xSe_2$ (CIGS), are considered as the leading materials for polycrystalline thin films solar cells. Solar modules based on these materials offer much lower cost and demonstrate superior stability and higher efficiency than conventional crystalline silicon cells. Highest efficiencies recorded for CIGS based terrestrial solar cells, sub-modules and large modules are 19.4%, 16.7% and 13.5%, respectively.[2-4] Therefore, the synthesis of these materials with precise control on size, morphology and stoichiometric composition has attracted remarkable research attention during the past two decades.

A number of techniques have been used for preparation of these materials. These techniques include metal-organic chemical vapor phase epitaxy (MOVPE), physical vapor deposition, co-evaporation, flash evaporation, selenization, chemical bath deposition (CBD) and chemical vapor deposition including LP-CVD and AA-CVD. However, despite a lot of work, it is still a challenge to precisely control the size and shape of the nanostructures, especially in large scale synthesis due to the lack of comprehensive knowledge on various factors governing the growth of nanoparticles and evolution of their morphology.

The single source precursor approach offers many advantages over conventional deposition technique by offering safer and better controlled processes. Furthermore, it avoids the use of highly toxic and/or oxygen or moisture sensitive gases like H_2S, H_2Se, NH_3, SiH_4 *etc*. Over the last several years, Paul O'Brien and co-workers have developed a wide range of single source precursors and used these precursors for deposition of semiconductor materials. More recently, dialkyldichalcogenophosphinatometal complexes have been synthesized and herein we report the use of these complexes as single source precursors for the deposition of thin films and nanoparticles of binary

($Cu_{2-x}Se$, In_2Se_3, Ga_2Se_3), ternary ($CuInSe_2$, $CuGaSe_2$) and quaternary ($CuIn_{(1-x)}Ga_xSe_2$) metal chalcogenides.

3.2 Synthesis and characterization of the ionic ligand

The ionic ligand $[HNEt_3]^+[^iPr_2PSe_2]^-$ was synthesized using a literature procedure.[5] However, it was observed that while attempting synthesis of $[HNEt_3][^iPr_2PSe_2]$, formation of a side product adversely affects the yield of reaction. This product was isolated as reddish coloured octahedral crystals and later characterized as bis(diisopropylselenophosphinyl)diselenide. Synthesis of this product has already been carried out by O'Brien *et al.* under different conditions.[5] Use of 20 % excess quantity of triethylamine significantly improved the yield of the reaction probably by ensuring the availability of $[HNEt_3]^+$ counter ion to stabilize the $[^iPr_2PSe_2]^-$ anion. The reaction for the synthesis of the ligand can be represented as Eq. 1.

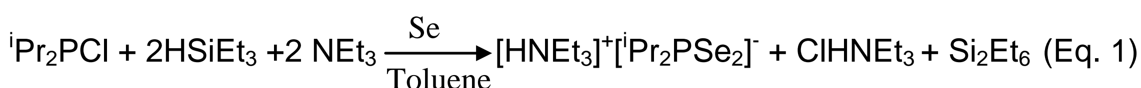

$$^iPr_2PCl + 2HSiEt_3 + 2\,NEt_3 \xrightarrow[\text{Toluene}]{\text{Se}} [HNEt_3]^+[^iPr_2PSe_2]^- + ClHNEt_3 + Si_2Et_6 \quad \text{(Eq. 1)}$$

The synthesized ligand was characterized using microanalysis, ^1H NMR spectroscopy, ^{13}C NMR spectroscopy and mass spectrometry. Microanalysis results were in fair agreement to the weight percentages of the carbon, hydrogen, nitrogen and phosphorus calculated for $[HNEt_3][^iPr_2PSe_2]$ suggesting the purity of the product obtained. A triplet for methyl protons and a quartet for methylene protons were observed in ^1H NMR spectrum. Coupling of methylene protons in the isopropyl group at phosphorus with the methyl group and phosphorus gave doublet of septets while methyl protons there gave doublet of doublets. Splitting of methyl and methylene carbons of isopropyl group was observed in the ^{13}C NMR spectrum which confirmed that these carbons are non-equivalent. Mass spectrum showed a base peak at 275, which was assignable to $[^iPr_2PSe_2]^-$, while another important peak was observed at m/z 102 for $[HNEt_3]^+$. The product obtained was moisture and air stable even after long storage times.

3.3 Synthesis of $M_x[^iPr_2PSe_2]_y$ (M=In, Ga, Cu) complexes

Diisopropyldiselenophosphinatometal complexes were synthesized by metathesis reaction of the ligand with the metal halides in a polar solvent

(methanol). The ionic ligand easily dissociates in methanol producing $[^{i}Pr_2PSe_2]^-$ anion, which readily reacts with metal salts to produce complexes in high yield and with good purity. The one-step reactions between methanolic solution of ligand and methanolic or aqueous solution of metal halide were conducted at room temperature and atmospheric pressure. The reaction for indium and gallium complexes may be represented as Eq. 2.

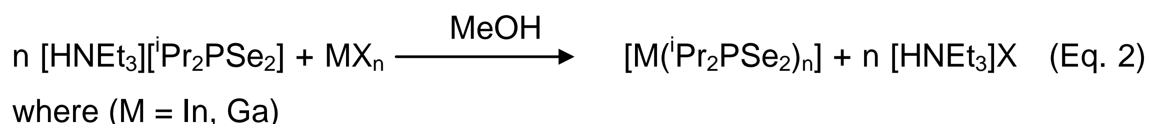

$$n\ [HNEt_3][^{i}Pr_2PSe_2] + MX_n \xrightarrow{MeOH} [M(^{i}Pr_2PSe_2)_n] + n\ [HNEt_3]X \quad \text{(Eq. 2)}$$

where (M = In, Ga)

whereas the reaction for the formation of the tetranuclear copper complex may be represented as Eq. 3.

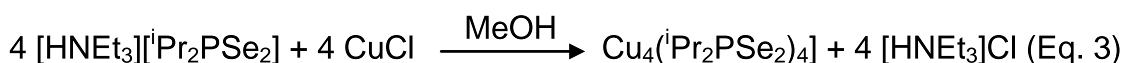

$$4\ [HNEt_3][^{i}Pr_2PSe_2] + 4\ CuCl \xrightarrow{MeOH} Cu_4(^{i}Pr_2PSe_2)_4] + 4\ [HNEt_3]Cl \quad \text{(Eq. 3)}$$

In all these reactions, the complexes were formed in fairly good yield and they were air and moisture stable even after long term storage. The summary of the synthesis process for diisopropyldiselenophosphinatometal complexes is given below in Table 3.1.

Table 3.1 Summary of the synthesis process for diisopropyldiselenophosphinato- metal complexes

Metal Salt	Ligand	Product Formula	Product Appearance	Yield (%)
$InCl_3$ (3.33 mmol)	$[HNEt_3][^{i}Pr_2PSe_2]$ (10 mmol)	$[In(^{i}Pr_2PSe_2)_3]$	Yellow crystals	88.5
$GaCl_3$ (3.33 mmol)	$[HNEt_3][^{i}Pr_2PSe_2]$ (10 mmol)	$[Ga(^{i}Pr_2PSe_2)_3]$	Yellow crystals	71.5
CuCl (10 mmol)	$[HNEt_3][^{i}Pr_2PSe_2]$ (10 mmol)	$[Cu_4(^{i}Pr_2PSe_2)_4]$	Yellow crystals	75.4

Characterization of the complexes was carried out by using microanalysis and ^{1}H NMR spectroscopy. Microanalysis results were in full agreement with those calculated for these complexes. ^{1}H NMR spectra of the complexes exhibited exactly the same signals for methyl and methylenic protons as have been previously reported for these complexes.[6] All the complexes gave only one set of signals for the isopropyl group suggesting the symmetrical nature of the molecule. It showed that all alkyl groups in the molecule have the same degree of shielding. A typical spectrum of diisopropyldiselenophosphinatometal complexes consists of one doublet of doublets for the methyl protons and one doublet of septets for the methylene protons. The $^3J_{HH}$ coupling constants have values around 6.7 Hz whereas chemical shifts for these complexes are summarized below in Table 3.2.

Table 3.2 Summary of H NMR data of diisopropyldiselenophosphinatometal complexes

	$(CH_3)_2C\underline{H}PSe_2$ δ (ppm)	$(C\underline{H}_3)_2CHPSe_2$ δ (ppm)
In	2.24, dsep	1.37, dd
Ga	2.29, dsep	1.31, dd
Cu	2.44, dsep	1.35, dd

3.4 Growth of nanomaterials

A series of experiments were performed in order to establish the possibility of using diisopropyldiselenophosphinate complexes as single source precursors for deposition of thin films and nanoparticles. An improvised AACVD kit was used to carry out deposition of metal chalcogenide semiconductor thin films at different temperatures. Similarly, thermolysis of precursors in coordinating solvents and subsequent growth of nanosized colloids was chosen as the growth methodology for obtaining nanoparticles. Size of nanoparticles was controlled by judicious selection of growth temperatures and reaction duration. Nanomaterials obtained were characterized by optical absorption and emission spectroscopy, powder X-ray diffraction (XRD), scanning electron

microscopy (SEM), transmission electron microscopy (TEM) and energy dispersive X-ray (EDX) analysis.

3.5 Growth of Copper selenide nanostructures

3.5.1 Copper selenide thin films

Thin films of copper selenide were deposited by aerosol-assisted chemical vapor deposition (AACVD) technique using copper complex $[Cu_4(^iPr_2PSe_2)_4]$ as single source precursor (SSP). Temperatures ranging from 300 to 475 ºC were employed in the deposition experiments to find out the optimum temperature for best deposition. At 300 °C, no clear deposition was observed onto the substrates. However, deposition experiments at 350 °C and above temperatures gave uniform deposition of black, shiny and well adhered material onto the substrates. As deposited films were characterized by using UV-Vis spectrometry, powder XRD studies, scanning electron microscopy (SEM) and energy dispersive X-ray (EDX) analysis.

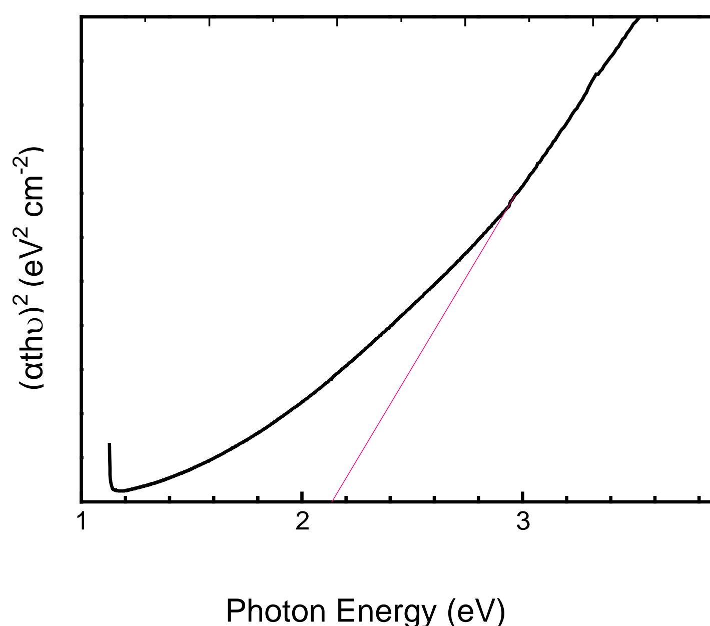

Photon Energy (eV)

Figure 3.1 $(\alpha th\upsilon)^2$ vs. hυ plots of $Cu_{2-x}Se$ films deposited at 475 °C showing a direct bandgap of ~ 2.1 eV

Figure 3.1 shows $(\alpha th\upsilon)^2$ vs. hυ plots of $Cu_{2-x}Se$ films deposited at 475 °C. Extrapolation of the straight line part of the $(\alpha th\upsilon)^2$ vs. hυ plot to the hυ axis,

where $(\alpha h\upsilon)^2 = 0$, gives the direct bandgap value. It was found that the film had a direct bandgap of ~ 2.1 eV which is in fair agreement with the literature values of 2.15 eV.[7,8]

Powder XRD patterns of copper selenide thin films grown at 350 °C, 375 ⁰C, 425 ⁰C and 475 ⁰C are shown in Figure 3.2. Analysis of the diffraction patterns revealed that berzelianite phase of $Cu_{2-x}Se$ (ICDD pattern 00-006-680) was deposited at all temperatures. No peaks assignable to other phases of copper selenide were observed in the diffraction pattern. Relatively narrow and sharper peaks were observed for thin films deposited at higher temperatures of 450 ⁰C and 500 ⁰C. This reflects larger grain size and better crystallinity of $Cu_{2-x}Se$ material deposited at higher temperatures.

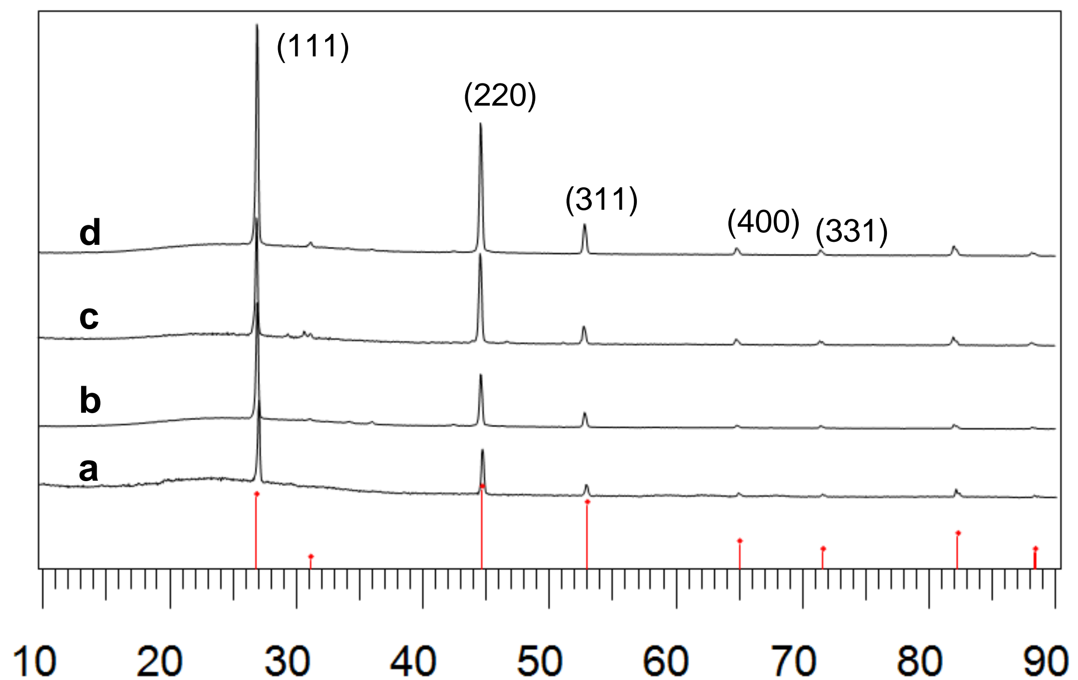

Figure 3.2 XRD patterns of deposited thin films of $Cu_{2-x}Se$ at 350 °C, 375 ⁰C, 425 ⁰C and 475 ⁰C. Red vertical lines at the bottom show standard ICDD pattern (00-006-680) for berzelianite phase of $Cu_{2-x}Se$ material

Surface morphology of deposited films was studied by using scanning electron microscopy. Representative SEM images of $Cu_{2-x}Se$ films deposited at various temperatures are shown in Figure 3.3. It was clearly evident that the shape of the deposited grains varies significantly with the deposition temperature. Randomly distributed globular grains are formed at 350 ⁰C

whereas deposition at higher temperature yields granular and predominantly triangular morphology. At 475 ºC, large grains with multiple triangular faceting are clearly visible. EDX analysis shows deviation from normal stoichiometric ratio of 2 : 1 for copper and selenium. Materials obtained at 300 ºC and 350 ºC temperatures were slightly Cu deficient while materials obtained at higher temperatures showed even more Cu deficient stoichiometry.

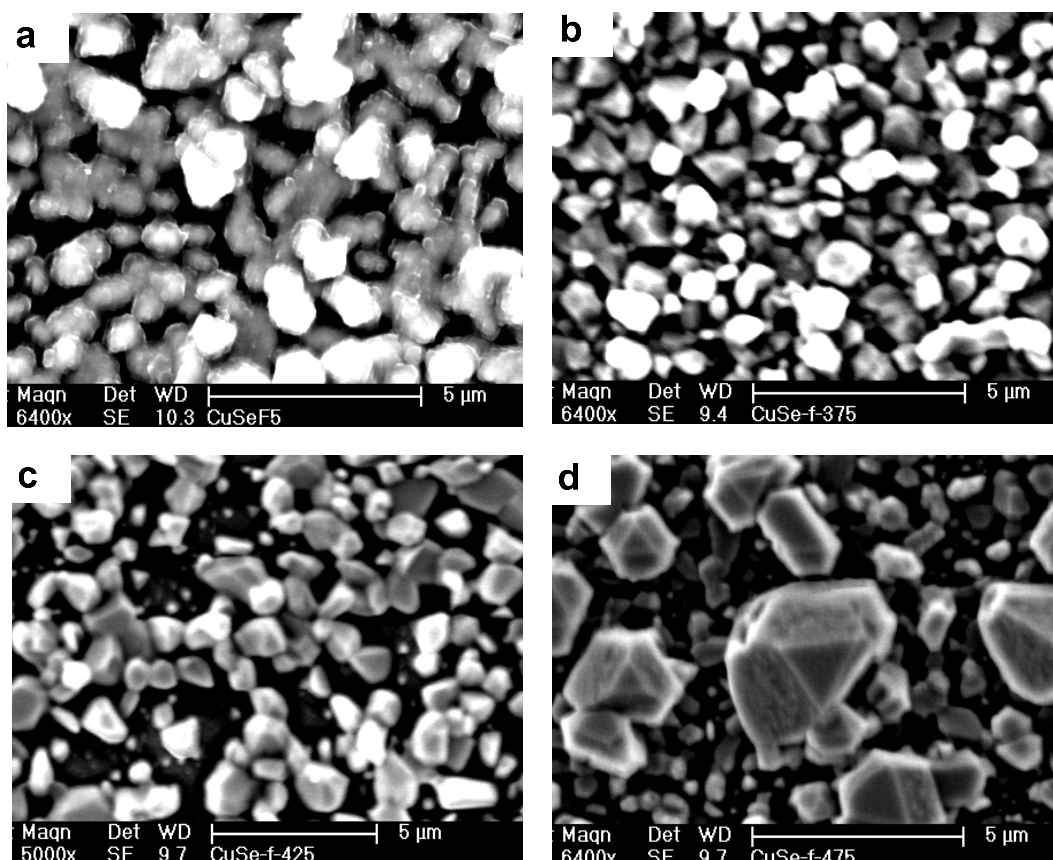

Figure 3.3 SEM images of the $Cu_{2-x}Se$ films deposited at (a) 350 °C (b) 375 °C (c) 425 °C and (d) 475 °C

3.5.2 Copper selenide nanoparticles

Thermolysis of $[Cu_4(^iPr_2PSe_2)_4]$ in HDA/TOP system at 250 °C yielded brown $Cu_{2-x}Se$ nanoparticles. The average size of the nanoparticles was calculated as 13 ± 2.5 nm. Reactions carried out below 200 °C resulted in partial decomposition of the precursor. UV-Vis absorption spectrum of grown nanoparticles showed band edge at 860 nm (Figure 3.4).

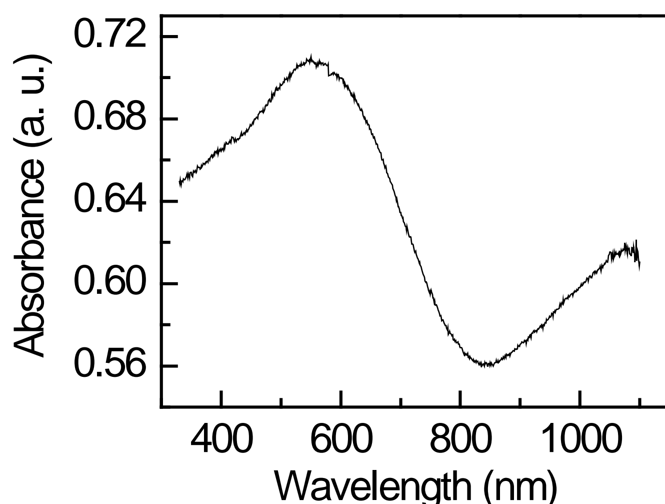

Figure 3.4 UV-Vis absorption spectrum of $Cu_{2-x}Se$ nanoparticles synthesized from 0.3 g precursor at 250 °C.

Powder XRD pattern of the HDA capped nanoparticles is shown in Figure 2.5 which corresponds to standard ICDD pattern for cubic $Cu_{2-x}Se$ phase (ICDD 00-006-0680). No peaks assignable to other phases of CuSe were traceable in the diffraction pattern. The size of the nanoparticles was calculated using Scherrer equation:

$$t = 0.9\lambda / (B \cos\theta_B)$$

where t is the average size of crystallites; K is the Scherrer constant; λ is the wavelength of X-ray; and B is the full width half maximum (FWHM) of peak located at 2θ.

The data of the three strongest peaks, (111), (220), and (311) peak, were used to calculate the average, and the average size of nanoparticles synthesized from 0.3 g precursor at 250 °C was found to be 14.4 nm, which is in fair agreement with the results obtained from TEM images. A few experiments carried out to investigate the effect of concentration of precursor used and reaction temperature revealed that the higher precursor concentration and reaction temperature leads to the increased mean size of the nanoparticles, as evident from the peaks becoming stronger and narrower (Figure 3.3 B). Similar results have already been reported by O'Brien *et al.* for synthesis of $Cu_{2-x}Se$ nanoparticles from Cu(II) acetylactonate and TOPSe.[9]

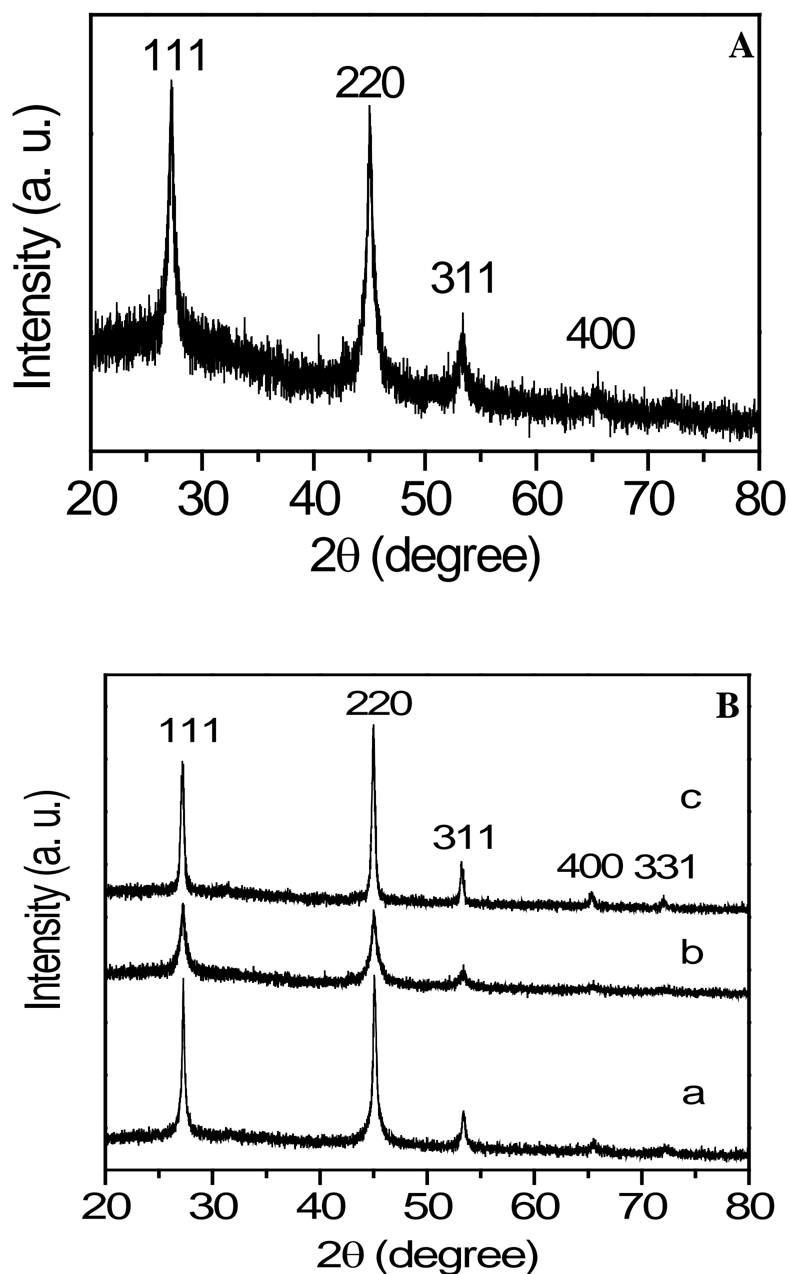

Figure 3.6 (A) XRPD pattern of cubic $Cu_{2-x}Se$ (JCPDS 06-0680) nanoparticles synthesized at 250 °C. (B) XRD patterns of cubic $Cu_{2-x}Se$ (JCPDS 06-0680) nanoparticles synthesized from (a) 0.3 g precursor at 250 °C, (b) 0.15 g precursor at 250 °C, and (c) 0.15 g precursor at 300 °C.

Figure 3.6 shows the TEM images of the HDA capped $Cu_{2-x}Se$ nanoparticles obtained from thermolysis of 0.3 g of $[Cu_4(^iPr_2PSe_2)_4]$ precursor at 250 °C. Well-defined $Cu_{2-x}Se$ nanocrystals were observed in TEM images while HR-TEM images clearly showed lattice fringes. Interplanar distances were

found to be 0.33 nm which are consistent with the known value for d_{111} interplanar distance of cubic $Cu_{2-x}Se$ nanoparticles.

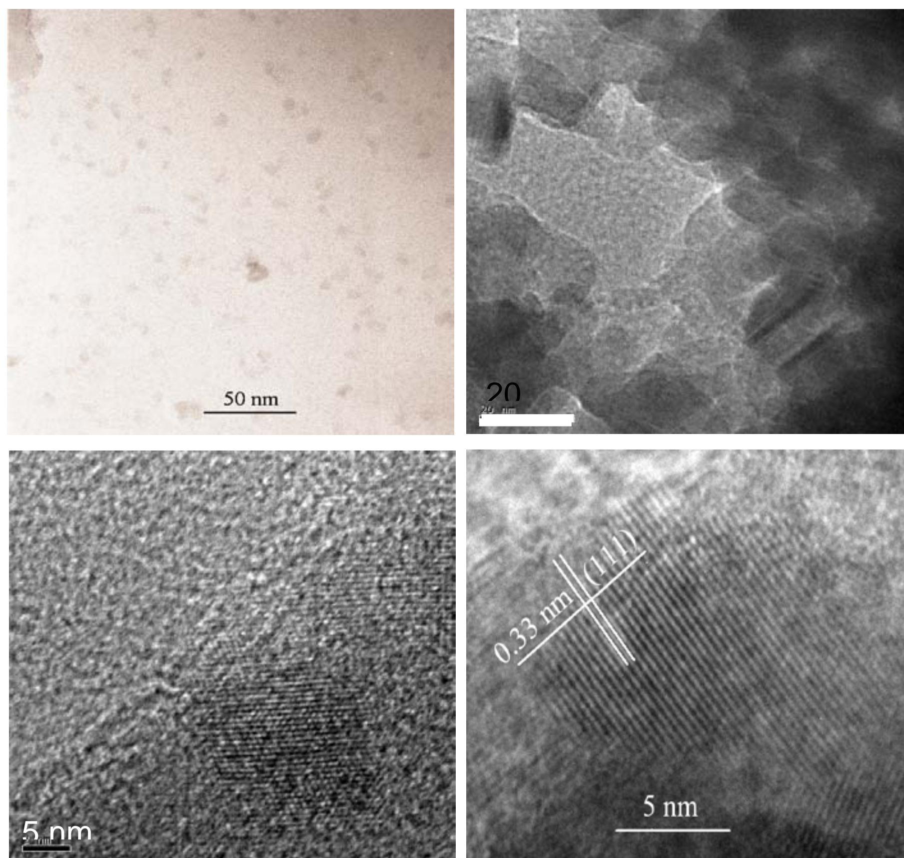

Figure 3.6 (a-b) TEM and (c-d) HR-TEM images of $Cu_{2-x}Se$ nanoparticles grown from thermolysis of $[Cu_4(^iPr_2PSe_2)_4]$ precursor at 250 °C

3.6 Growth of Indium selenide nanostructures

3.6.1 Indium selenide thin films

Thin films of In_2Se_3 were deposited by AACVD process using $[In(^iPr_2PSe_2)_3]$ as the single source precursor (SSP). Aerosols generated from solution of 0.2 g of $[In(^iPr_2PSe_2)_3]$ precursor in 20 ml of toluene were transferred to the reactor where thermally induced decomposition of the precursor resulted in deposition of indium selenide onto glass substrates placed in the CVD reactor. Owing to our previous experience with AACVD of this precursor, In_2Se_3 was deposited only at 450 °C as deposition at this temperature gave best films. Reddish black colour films of indium selenide were deposited which were well

adhered to the substrate and successfully passed scotch-tape test. Uniform coverage of the substrates was obtained. Optical and structural characterization of the films was carried out by using UV-Vis spectrometry, powder XRD studies and SEM/EDX studies.

UV/Vis spectrum of the films was recorded and band gap of the films was measured by extrapolating the straight line part of the $(\alpha h\upsilon)^2$ vs. hυ plot to the hυ axis, where $(\alpha h\upsilon)^2 = 0$. It was found that the films had an optical bandgap of about 1.82 eV (Figure 3.7), which is in good agreement with literature values of the same for γ-In_2Se_3.[10,11]

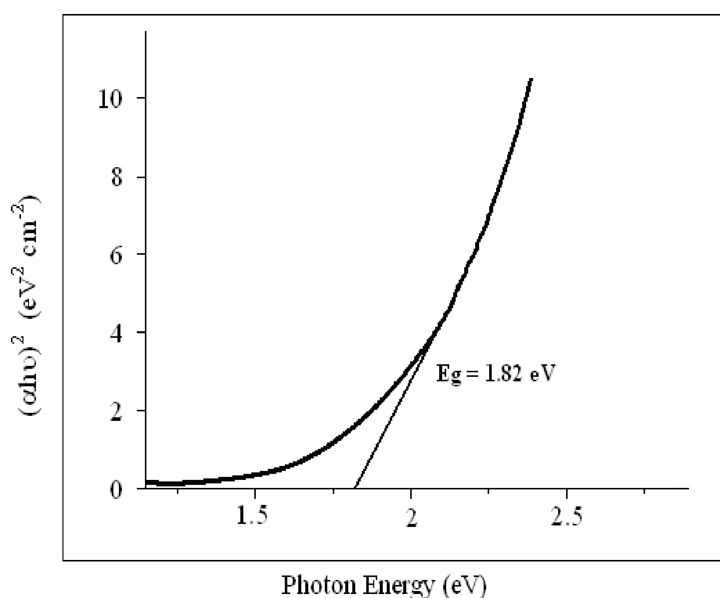

Figure 3.7 Plot of $(\alpha h\upsilon)^2$ *vs* band gap of γ-In_2Se_3 thin film showing a band gap of ~ 1.82 eV

Crystallographic phase of the deposited material was determined by using powder X-ray diffraction techniques. The XRD pattern revealed that the material obtained was γ-phase of In_2Se_3 (standard ICDD pattern 00-040-1407) which was preferentially oriented along (110) plane. Figure 3.8 shows XRD pattern of the material indexed to standard ICDD pattern for γ- In_2Se_3. Crystallinity of the In_2Se_3 material was reflected by sharpness of the XRD peaks. Furthermore, appearance of no additional peaks indicates that the material is significantly pure and no other phases of indium selenide are present.

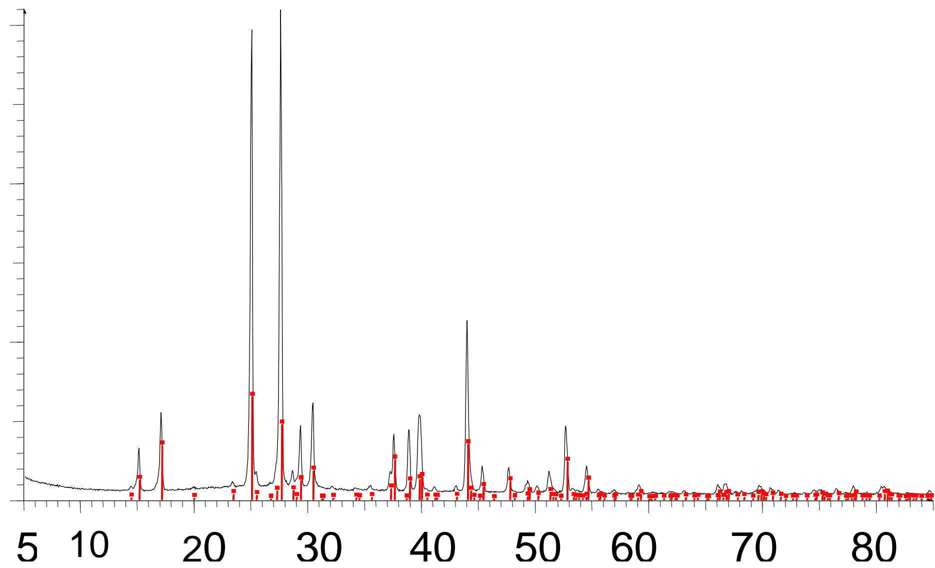

Figure 3.8 XRD pattern of γ-In_2Se_3 thin film at 450 °C. Red lines below show standard ICDD pattern 00-040-1407 for γ-phase of In_2Se_3

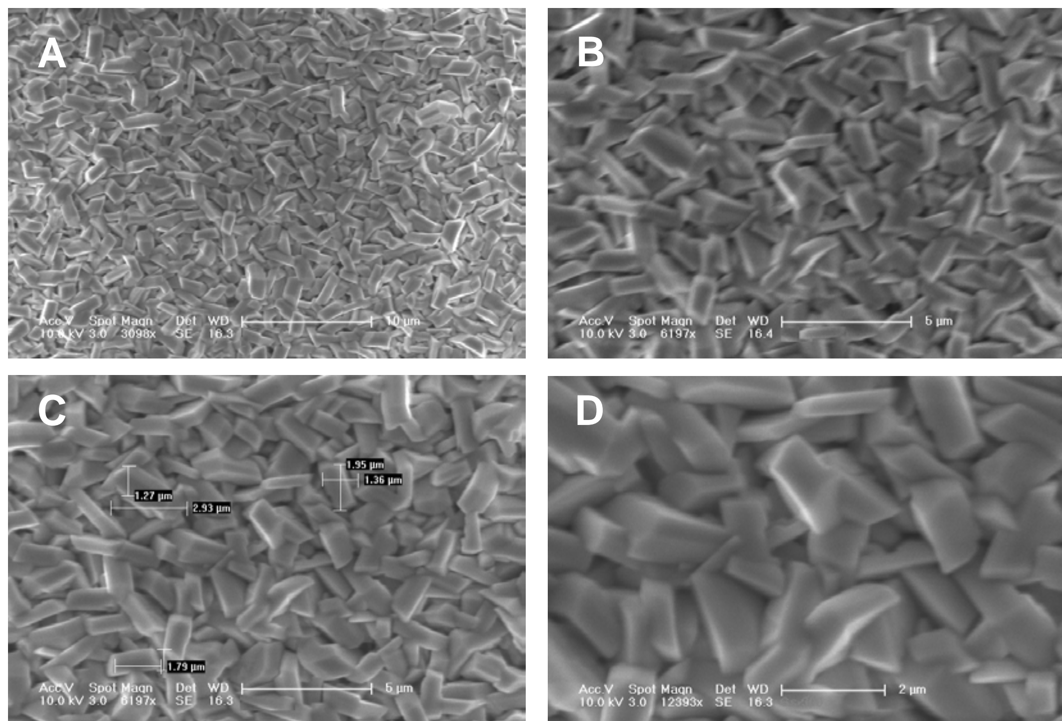

Figure 3.9 SEM images of the deposited γ-In_2Se_3 thin film at 450 °C.

SEM images of as deposited thin films (Figure 3.9) were obtained to study surface morphology of the deposited material. As expected, the SEM images showed uniform coverage of the substrates with highly crystalline grains deposited. These grains had a cylindrical morphology with approximate

dimensions of 1.27-1.36 μm x 1.79-1.95 μm. Homogeneous distribution of the grains on the surface was clearly evident as well. Stoichiometric composition of the material was determined by EDX analysis which showed that the material obtained is slightly Se rich, the ratio of indium to selenium being 2.05:3.5. Furthermore, no appreciable differences in stoichiometric composition of individual grains were observed.

3.6.2 Indium selenide nanoparticles

Indium selenide nanoparticles were grown by thermolysis of the $[In(^iPr_2PSe_2)_3]$ precursor at 270 °C in HDA/TOP system. Thermolysis of the precursor at lower temperatures yielded materials with poor crystallinity which showed no XRD pattern thus making it impossible to characterize through powder XRD. The TEM image of nanoparticles grown at 270 °C for 2 hours show well formed quasi spherical crystallites with an average size of 5.0 ± 1.2 nm (Figure 3.12). Absorption and emission spectra of obtained nanoparticles are shown in Figure 3.10. A calculated band edge of 430 nm in UV-Vis spectrum is clearly blue shifted indicating the presence of quantum confinement in nanocrystals. The emission spectrum shows maxima close to the band edge and FWHM of the emission peak suggests that the quantum dots obtained are nearly monodispersed. This is also reflected in the standard deviation obtained from the TEM images.

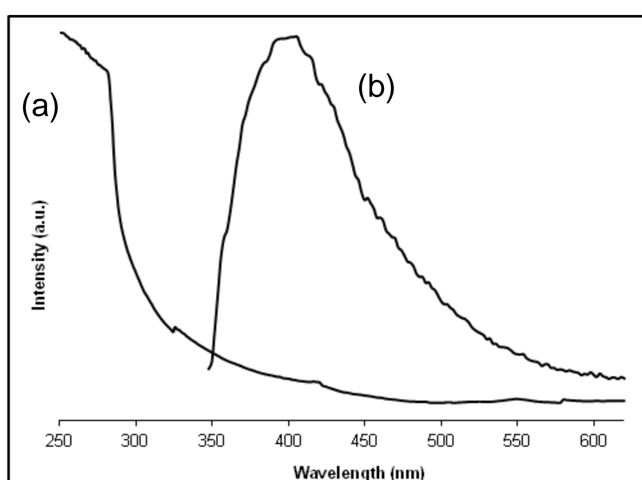

Figure 3.10 Room temperature (a) Optical absorption spectrum and (b) emission spectrum of toluene suspension of HDA capped InSe nanoparticles grown at 270 °C

Crystallographic phase of the nanoparticles was studied by powder X-ray diffraction. XRPD pattern of the HDA capped nanoparticles (Figure 3.11) corresponds to the hexagonal In_2Se_3 phase (ICDD pattern 00-012-0117). Preferred orientation along the (101) lattice plane was observed in the material and broader diffraction peaks indicated growth of very small nanoparticles. This was also supported by TEM images of the nanoparticles.The Scherrer equation was used to calculate the mean size of the nanoparticles. Data from (101), (110) and (202) peaks in the XRD pattern was used and the mean size of the nanoparticles was calculated as 4.7 nm, which fairly conform to the size of the nanoparticles obtained from TEM microscopy.

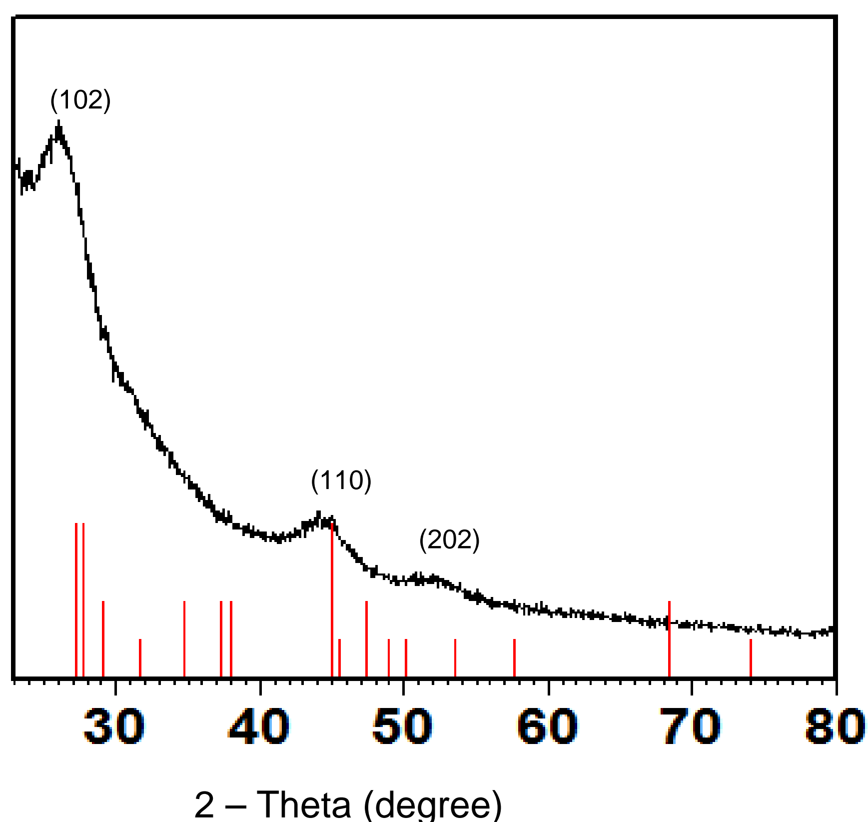

Figure 3.11 XRD pattern of HDA capped In_2Se_3 nanoparticles grown at 250 °C

Selected TEM images of the In_2Se_3 nanoparticles are shown in Figure 3.12. Predominantly spherical nanoparticles with an average diameter of 5.0 nm (± 1.1) are evident from TEM images. HR-TEM images show lattice fringes with an interplanar spacing of 3.28 nm which is the characteristic value for d_{102} interplanar distances for hexagonal In_2Se_3 phase. The slight excess of Se in the material was indicated in the EDX analysis.

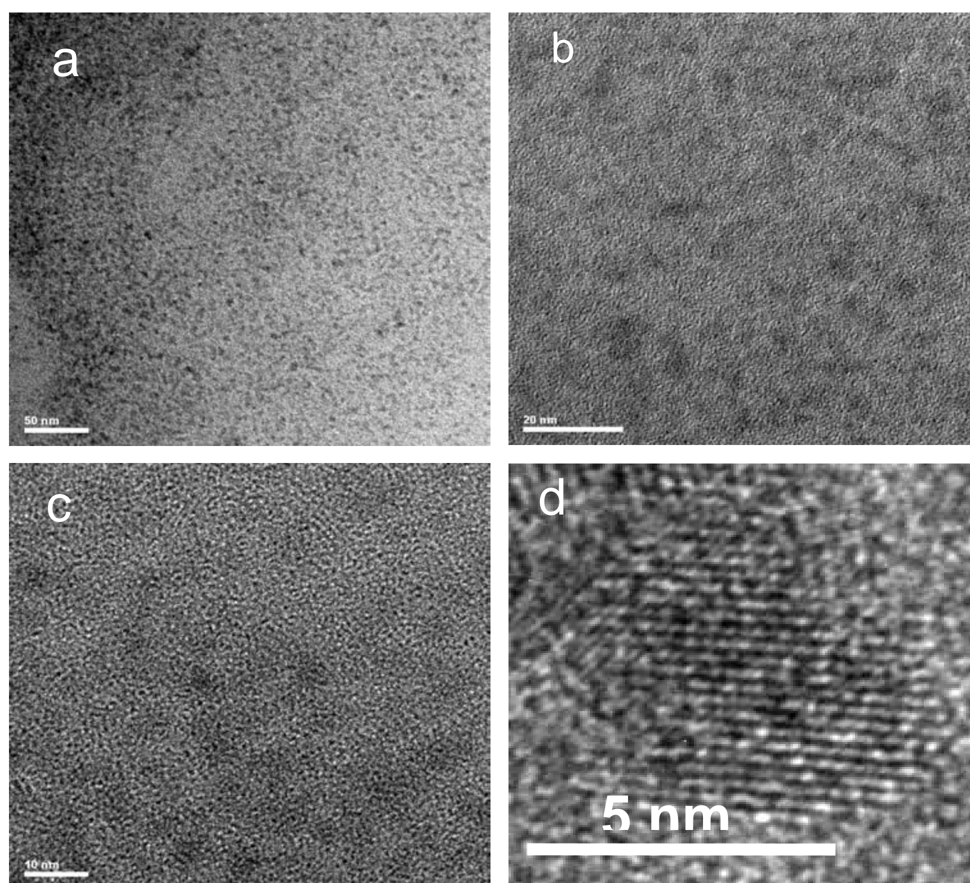

Figure 3.12 (a-c) TEM and (d) HR-TEM images of HDA capped indium selenide nanoparticles grown at 270 °C

In_2Se_3 exists in the α, β and λ phases while phase transition temperatures are 200 and 250 °C, respectively for the α-β and β-λ transitions. Previously O'Brien *et al.* have synthesized InSe nanoparticles with an average size of 6.4 nm by thermolyzing single source precursor $[In(Se_2CNEt_2)_3]$ in TOPO at 250 °C.[12] However, in their study, phase present in the nanoparticles could not be defined due to poor crystallinity of the material. In a later report, hexagonal 'wafer-like' nanocrystals with average diameter of 141 nm (± 24 nm)

were synthesized by reaction of $In(ac)_3$ and Se in HDA at 300 °C.[13] Longer reaction durations (18 h) were employed which might be the cause of the formation of larger nanocrystals.

3.7 Growth of gallium selenide nanostructures

3.7.1 Deposition of Ga_2Se_3 thin films

Deposition of Ga_2Se_3 thin films onto glass substrates was attempted by AACVD process at temperatures ranging from 300 °C to 500 °C. Very little or almost no deposition occurred at 300 °C, while at 350 °C poor coverage of films was obtained which was not enough for characterization through powder XRD studies. However, yellow transparent films were obtained at higher temperatures (400 °C - 500 °C).

Optical absorption spectra of the films were used to calculate band gap of the deposited material. Band gap (E_g) was determined by extrapolation of the straight line of the linear part of the spectrum as shown in Figure 3.13 and it was found to be 2.15 eV. This value fairly coincides with band gap values of Ga_2Se_3 (2.1 – 2.7 eV) already reported in literature.[14-16]

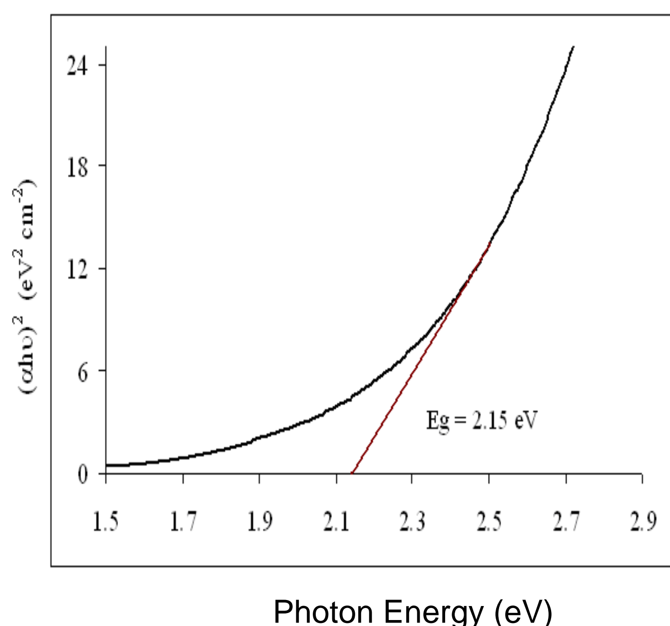

Figure 3.13 Plot of $(\alpha h\upsilon)^2$ *vs* band gap of Ga_2Se_3 thin films (Bandgap ~ 2.15 eV)

Crystallographic phase of the deposited material was identified by powder XRD technique. Very poor diffraction patterns (Figure 3.14) were obtained below 450 °C which were indicative of poor crystallinity of the material. However, diffraction peaks observed for AACVD experiments at 500 °C were assignable to monoclinic phase of Ga_2Se_3 (ICDD pattern 01-076-0975). These experiments demonstrate that crystallinity of the Ga_2Se_3 material improves when higher deposition temperatures are employed.

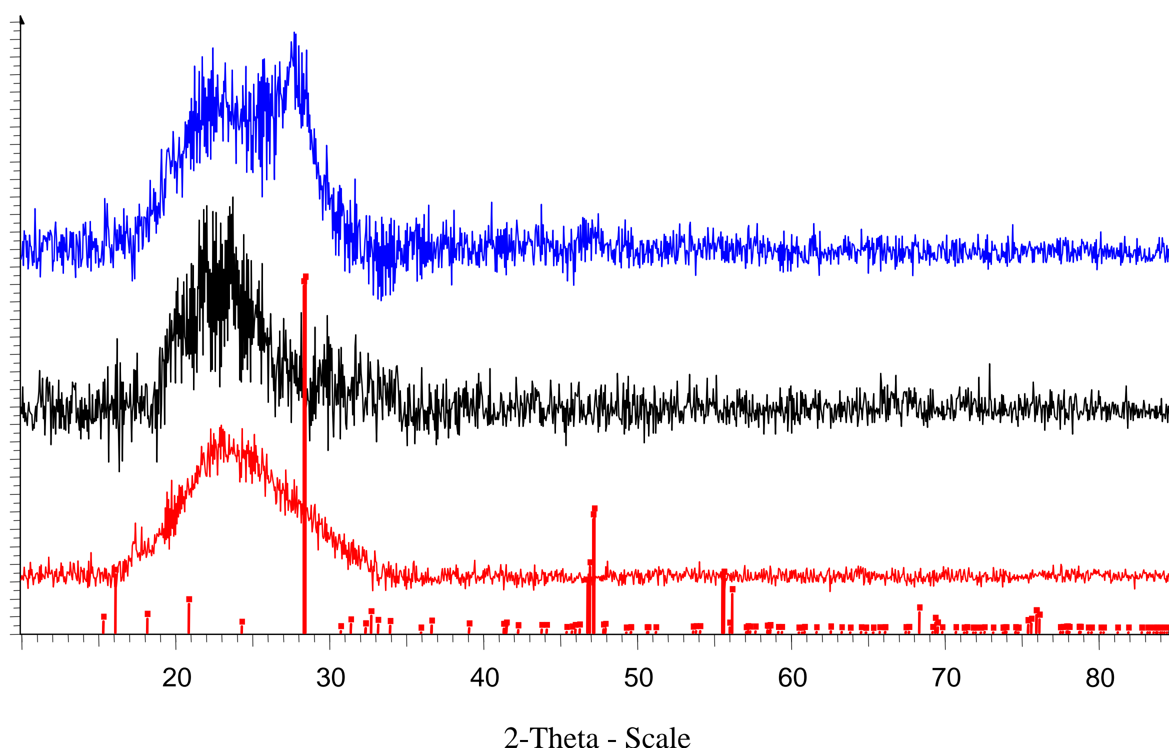

Figure 3.14 XRD patterns of Ga_2Se_3 thin films deposited at 400 ºC (red), 450 ºC (black) and 500 (blue) ºC indexed with standard ICDD pattern 01-076-0975

Scanning electron microscopy was used to study surface morphology of the deposited films. SEM images of the films deposited at 500 °C (Figure 3.15) illustrate that the film contains very small grains with poorly defined flake-like morphology. The particle size was found to be in the range of 0.1-0.25 μm. This is in agreement with the result of XRD analysis which showed broader and less sharp peaks which arise from smaller particles with poorly defined crystallographic arrangement. Attempts to improve crystallinity of deposited gallium selenide material by annealing at 400 °C for 14 hours proved

unsuccessful. The SEM images of annealed sample show bubble like holes of 1-2 μm diameter, but no crystallites were traceable in the film.

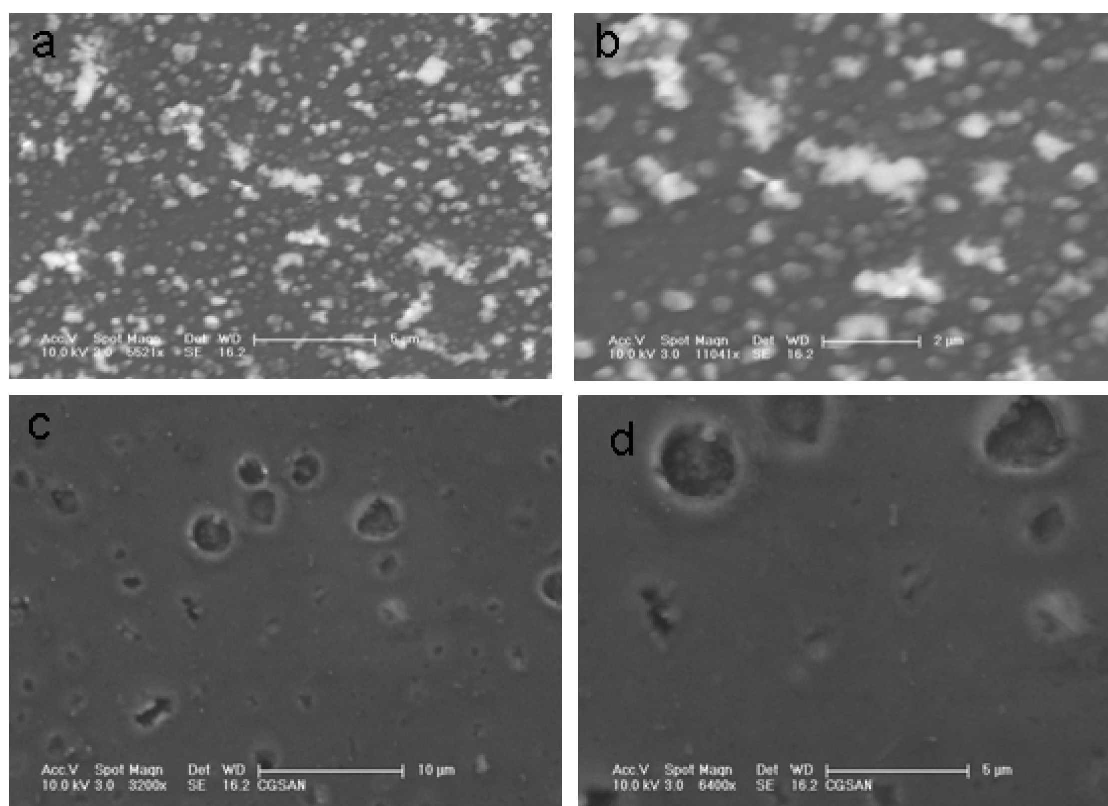

Figure 3.15 (a – b) SEM images of thin film of monoclinic Ga_2Se_3 deposited at 500 ºC (c – d) SEM image of monoclinic Ga_2Se_3 after annealing at 400 ºC for 14 hours

Surface morphology of the film was also studied by atomic force microscopy (AFM). AFM images (Figure 3.16) also show the similar random distribution of granules onto the films. However, the surface of the film was found to be smooth and uniform with 66.15 root mean square roughness (RMS). For photovoltaic application, the smoothness of the surface with small RMS is an important feature that contributes significantly towards overall device efficiency. Rough and non-uniform surfaces suffer from light scattering thus retarding the power conversion efficiency of fabricated PV devices and modules.

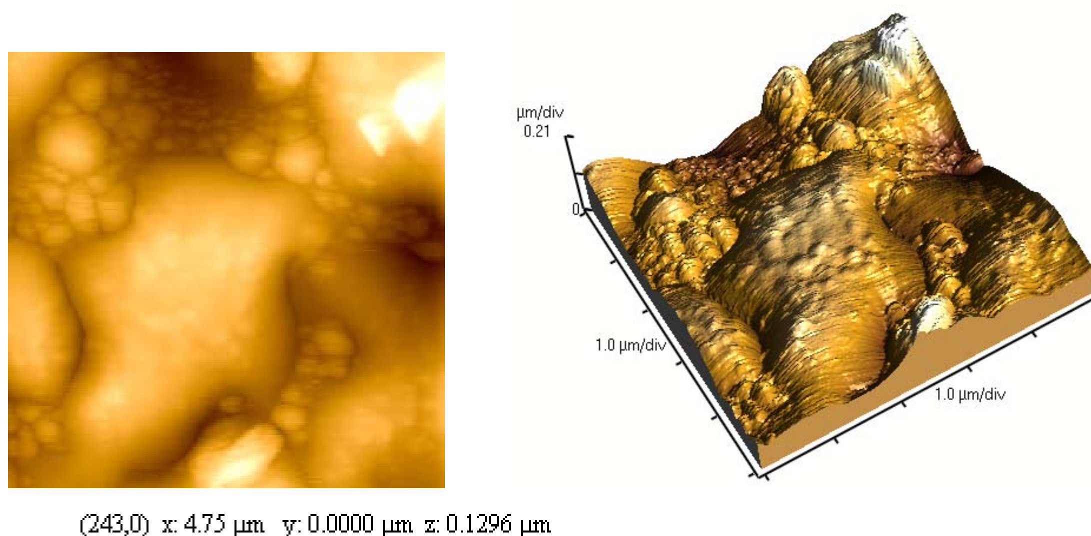

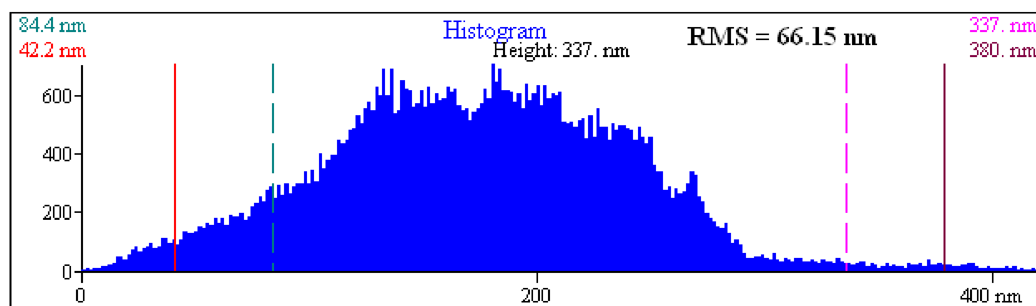

Figure 3.16 1D and 2D AFM images of as deposited Ga_2Se_3 thin films at 500 ºC and histogram of AFM image showing size distribution along with surface roughness

3.7.2 Attempted growth of gallium selenide nanoparticles

Repeated attempts to synthesize GaSe nanoparticles by thermolyzing the [Ga($^iPr_2PSe_2$)$_3$] precursor in HDA at 270 °C proved unsuccessful. The material obtained in these experiments was either amorphous as revealed by powder XRD studies or it gave an XRD pattern which corresponds to the standard ICDD pattern (00-022-0301) for gallium selenate hydrate, $Ga_2(SeO_4)_3 \cdot 16H_2O$ (Figure 3.17). Synthesis of gallium selenide nanoparticles has been scarcely reported in the literature and to best of our knowledge, colloidal synthesis of gallium selenide quantum dots has only been reported by Chikan and Kelly who have carried out high temperature inorganic synthesis of surface

capped GaSe nanoparticles by the reaction of trimethylgallium (Me_3Ga) with trioctylphosphine selenium (TOPSe) in TOPO/TOP system.[17] In the present study, inherent characteristics of the precursor may be the reason for unsuccessful synthesis of GaSe nanoparticles.

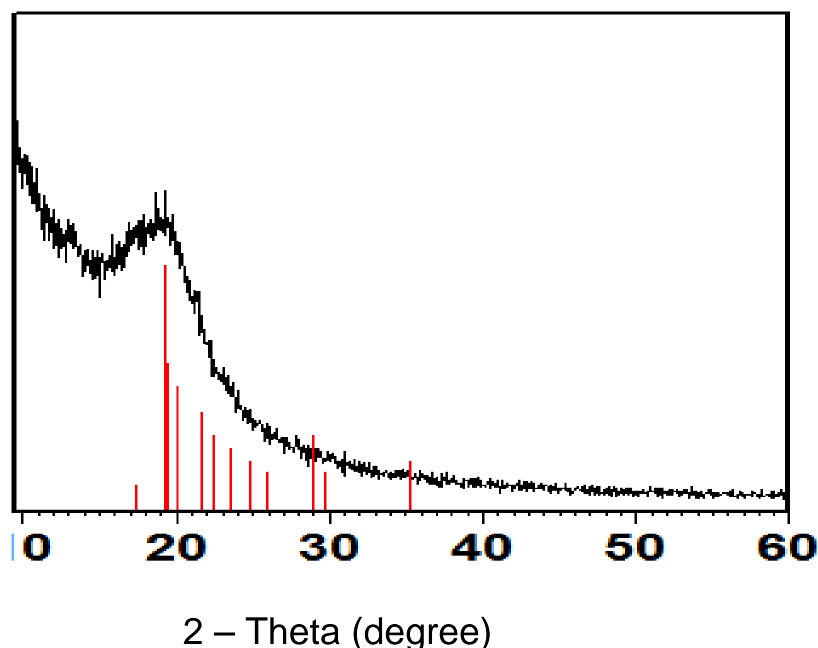

Figure 3.17 XRD pattern of gallium selenate hydrate nanoparticles corresponding to standard ICDD pattern 00-022-0301

3.8 Growth of copper indium diselenide nanostructures

3.8.1 Deposition of $CuInSe_2$ thin films

$CuInSe_2$ thin films were deposited by AACVD technique from 1:4 molar equivalents of $[Cu_4(^iPr_2PSe_2)_4]$ and $[In(^iPr_2PSe_2)_3]$ precursors, respectively. Temperatures ranging from 350 to 500 ºC were used to carry out deposition and micro-structural properties of the deposited material were investigated to find out the optimal temperature for deposition of $CuInSe_2$ from these precursors. No appreciable deposition occurred at 350 °C. However, deposition experiments undertaken at temperatures above 350 °C yielded well adhered, black transparent films. Optical band gap of the films was measured by direct band gap methods and it was found to be about 1.17 eV (Figure 3.18). The reported band gap energies of $CuInSe_2$ are 1.05 eV, 1.13 eV and 1.2 eV.[18,19]

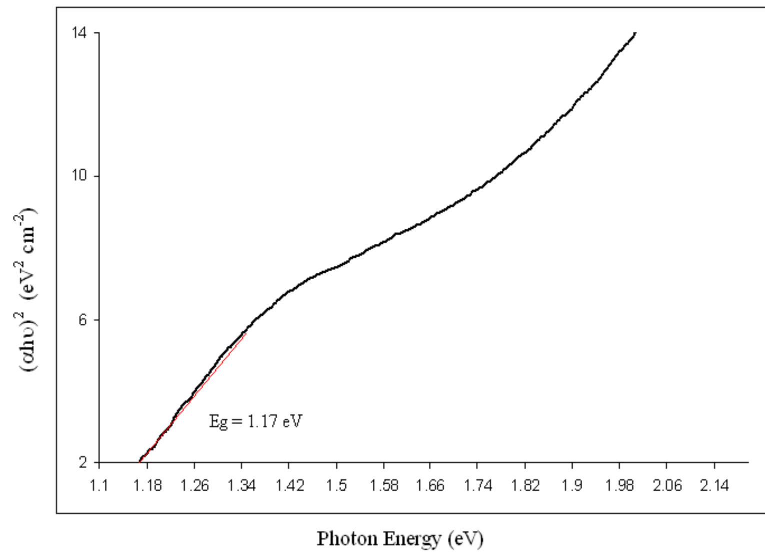

Figure 3.18 Plot of $(\alpha h\upsilon)^2$ *vs* band gap of $CuInSe_2$ thin films showing band gap of 1.17 eV.

Powder X-ray diffraction patterns of thin films were recorded to determine crystallographic phase of material. XRD patterns (Figure 3.19) demonstrated

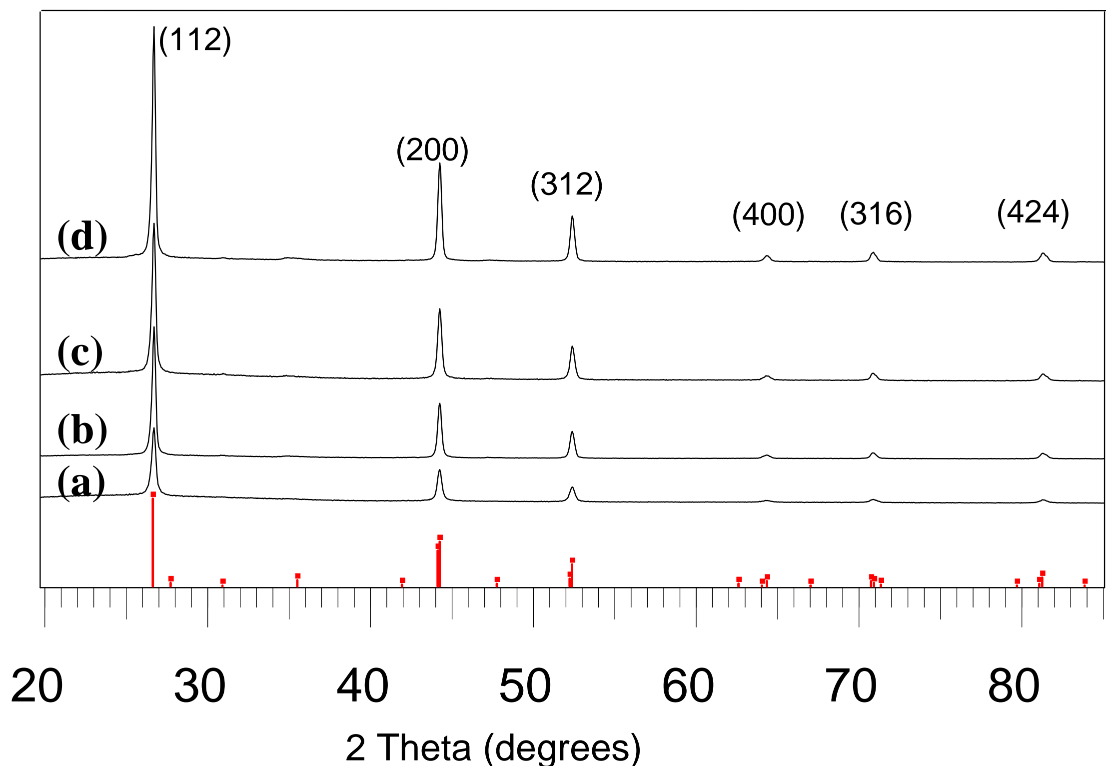

Figure 3.19 XRD patterns of deposited $CuInSe_2$ thin films in 1:4 ratios at temperatures (a) 350 °C, (b) 400 °C, (c) 450 °C and (d) 500 °C.

that tetragonal phase of $CuInSe_2$ (standard ICDD pattern 01-075-0107) was deposited at all temperatures. In all the cases, the material obtained exhibited preferred orientation along the (112) plane which is typical of ternary copper chalcopyrite compounds deposited by CVD. Fairly sharp peaks in the diffraction pattern reflected improved crystallinity of the material, whereas pure and monophasic nature of deposited material was demonstrated by absence of any additional peaks from binary phases of copper and indium selenide.

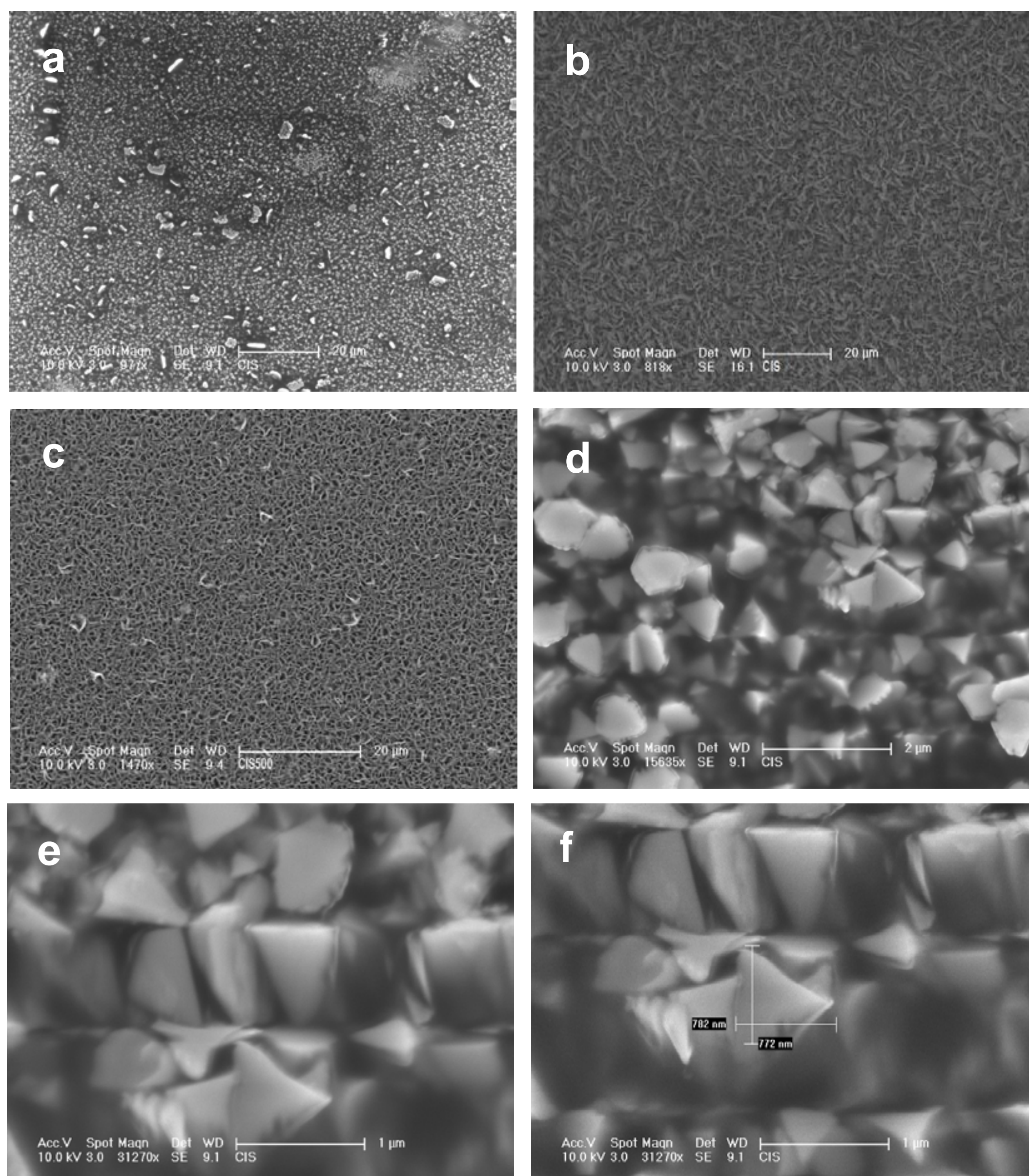

Figure 3.20 SEM images of as deposited thin films of $CuInSe_2$ at (a) 400 °C, (b) 450 °C and (c) 500 °C. Figures (d-f) show various magnifications of the thin film deposited at 400 °C

Surface morphology of the thin films was studied with the help of scanning electron microscopy. SEM images show a homogeneous deposition onto the substrate. Different morphologies of the deposited material were obtained at different temperatures. At 400 °C, the material exhibited predominantly triangular morphology with some hexagonal structures. Individual grains were having approximate dimensions of 782 nm x 772 nm. At 450 °C and 500 °C, flake like structures were deposited. Although narrow and sharp peaks in the XRD pattern suggested larger grains, the SEM images revealed that the size of the grains was significantly lower than expected. EDX analysis showed that the material was slightly Cu deficient but Se rich stoichiometric composition. Se rich composition of the $CuInS_2$ may be attributed to the precursors used which inherently contain more selenium.

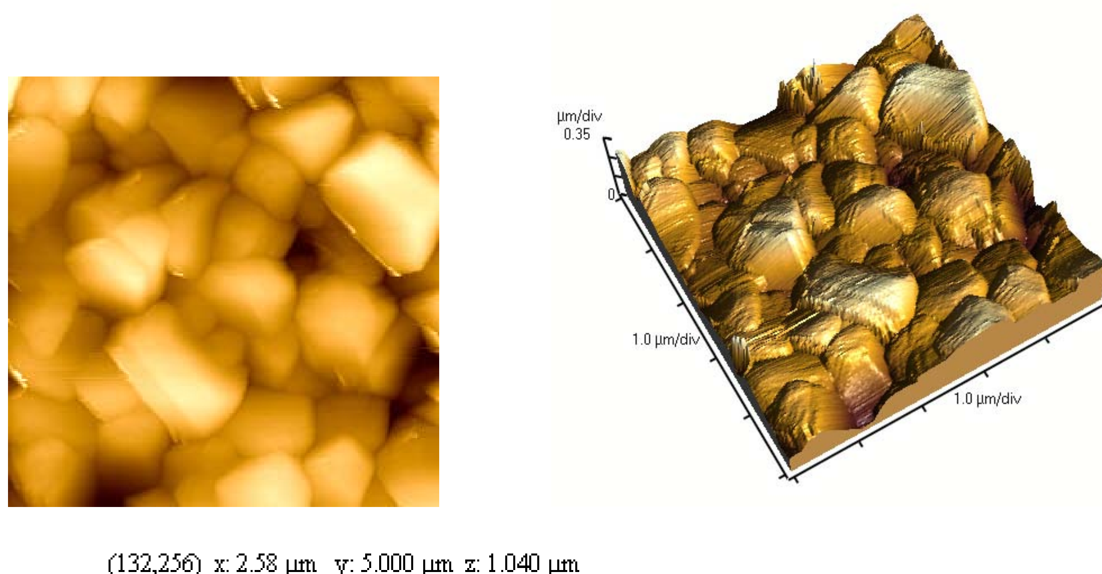

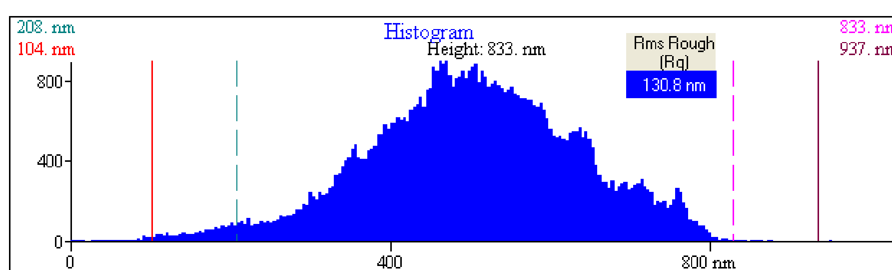

Figure 3.21 1D and 2D AFM images of as deposited $CuInSe_2$ thin films at 450 °C along with AFM histogram showing grain size distribution and surface roughness.

Morphological characterization of the $CuInSe_2$ films was also carried out by AFM analysis. AFM images of deposited $CuInSe_2$ thin films deposited at 450 °C are shown in Figure 3.21. The images revealed that deposited material consists of uniform sized granules which are homogeneously distributed onto the surface of glass substrates as agglomerates. The root mean square roughness of the thin film surface was calculated by acquiring a number of scans from different areas of the film and it was found to be130.8 nm.

3.8.2 Copper indium diselenide nanoparticles

Copper indium diselenide ($CuInSe_2$) nanoparticles were grown by thermolysis of 1:4 molar ratios of copper precursor and indium precursor in HDA at temperatures ranging from 120 – 210 °C in HDA/TOP system. Right after injection of precursors suspension in TOP into preheated HDA, the reactants turn dark brown indicating the formation of $CuInSe_2$ nuclei which undergo Ostwald's ripening to grow into nanocrystals. Work up of the reaction yielded well formed, monodispersed spherical particles. The size of the nanoparticles obtained depends upon the growth temperature and the reaction durations employed.

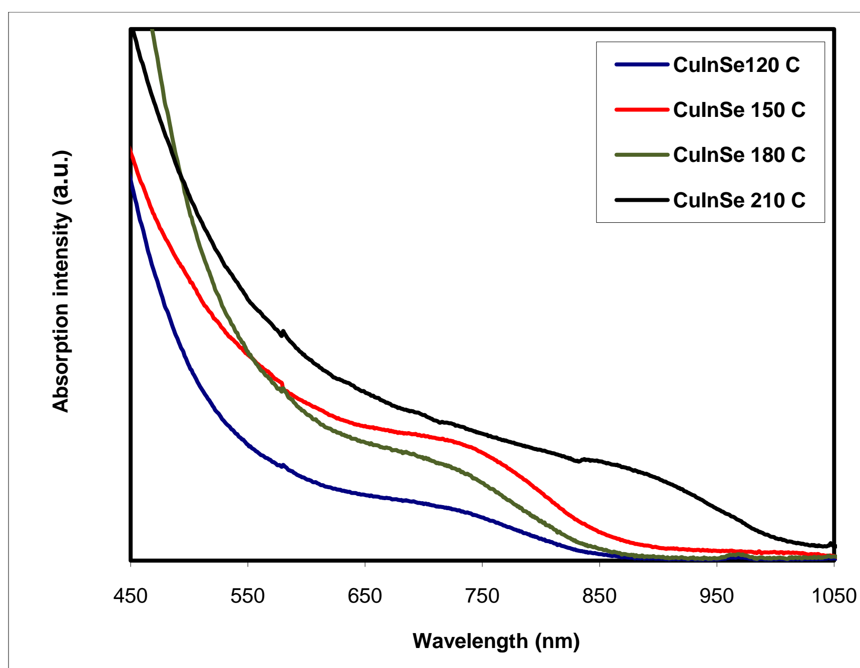

Figure 3.22 Room temperature Vis-NIR absorption spectra of HDA capped $CuInSe_2$ nanoparticles grown at different temperatures (120 – 210 °C) showing red shift of absorption band edge with increased growth temperatures.

Figure 3.22 shows the UV-Vis absorption spectra of HDA capped $CuInSe_2$ nanoparticles grown at different reaction temperatures. At all temperatures, nanoparticles obtained show significant red shifts in band edge compared to the same (1244 nm) for bulk $CuInSe_2$ which shows the presence of quantum confinement in these nanocrystals. It was observed that formation of larger nanoparticles takes place at higher growth temperatures and it was clearly evident from the shift of their absorption band edge to longer wavelengths. Therefore, judicious selection of the reaction parameters leads to size controlled synthesis of the nanoparticles.

Powder X-ray diffraction patterns of HDA capped $CuInSe_2$ nanoparticles are shown in Figure 3.23. XRD analysis revealed the deposition of tetragonal $CuInSe_2$ phase (standard ICDD pattern 00-040-1487) for the nanoparticles prepared at all the temperatures (120 – 210 °C). This is in coincidence with previous reports as the tetragonal chalcopyrite structure is most oftenly observed crystallographic arrangement in case of ternary Cu-chalcogenides.[20] No extra peaks were observed in the diffraction pattern which suggests that no significant impurities or side products were present in the materials obtained.

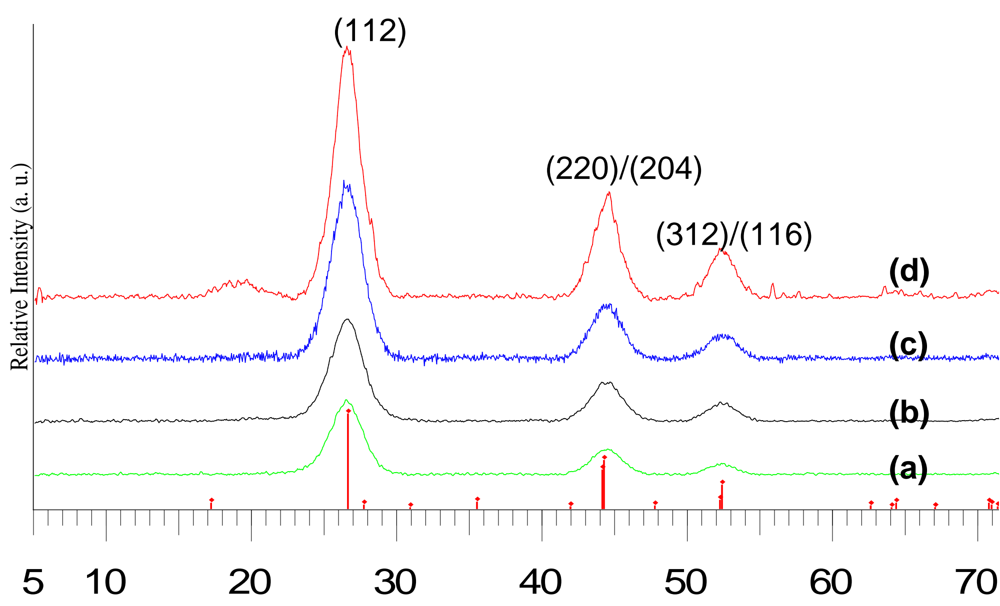

Figure 3.23 XRPD pattern of HDA capped $CuInSe_2$ nanoparticles grown at (a)120 °C (b) 150 °C (c) 180 °C and (d) 210 °C. Red lines below represent standard ICDD pattern (00-040-1487) for tetragonal $CuInSe_2$ phase.

In all cases, preferred orientation of the materials along the (112) plane was observed. Similar materials having preferred orientation along the (112) plane have been obtained by many groups.[21,22] XRD peaks appeared narrower and sharper for materials obtained at higher growth temperatures which indicate gradual increase in the size of nanoparticles obtained. The Scherrer formula

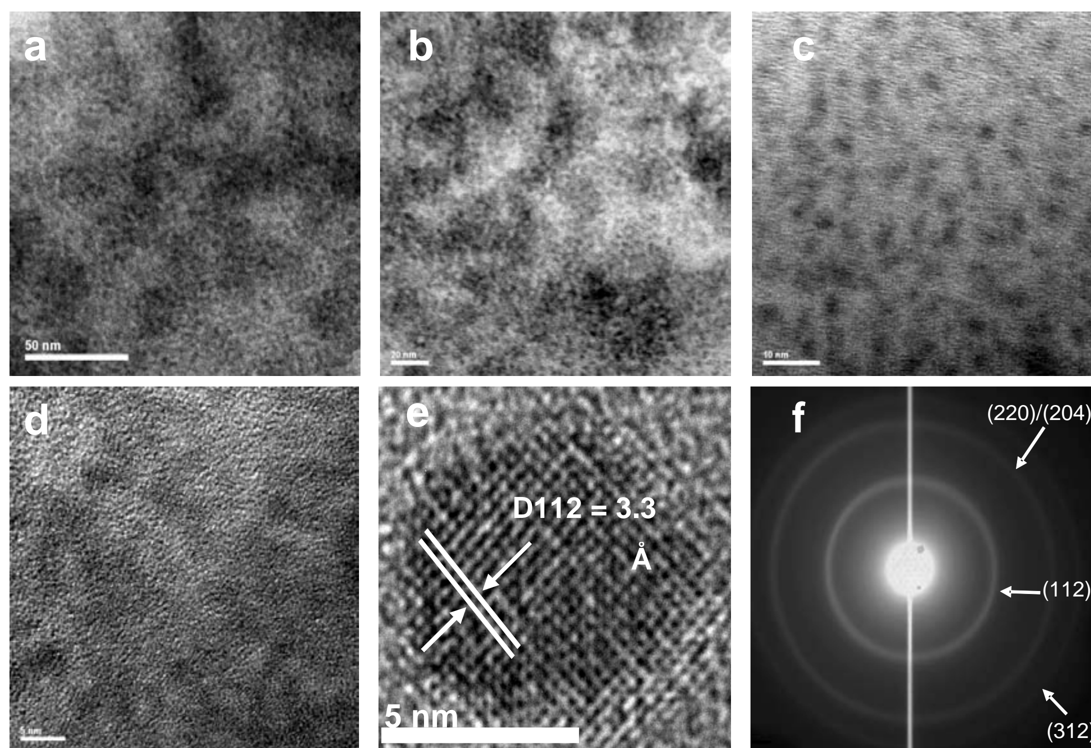

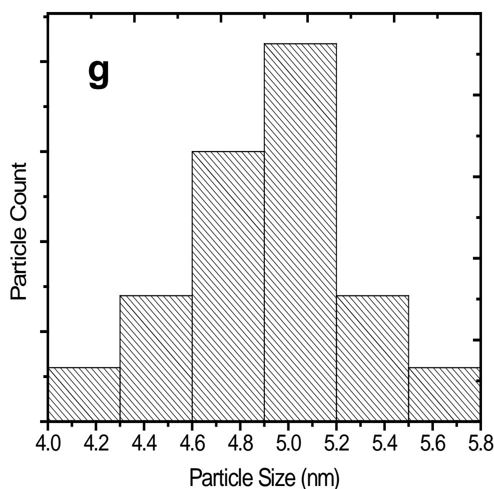

Figure 3.24 (a-d) TEM images (e) HR-TEM image and (f) SAED pattern of the HDA capped $CuInSe_2$ Quantum dots grown at 180 °C (g) Histogram showing size distribution of $CuInSe_2$ Quantum dots

was employed to calculate the size of the nanoparticles. Data from the (112) diffraction peak was used for calculation of the size of nanocrystallites and the results obtained gave slightly lower sizes than the same determined from TEM images. The size of the nanoparticles grown at 180 °C for instance was found to be 4.14 nm by Scherrer equation while average mean size of the particles revealed by TEM images was 4.9 ± 0.6 nm.

Figure 3.24(a-d) shows TEM images of HDA capped $CuInSe_2$ nanoparticles grown at 180 °C. Monodispersed spherical particles with a mean particle diameter of 4.9 ± 0.6 nm are clearly visible in TEM images. HR-TEM image (Figure 3.24e) showed lattice fringes and interplanar distance for these lattice fringes was found to be 3.3 Å which is characteristic for d_{112} plane of the tetragonal $CuInSe_2$. Figure 3.24f shows selected area electron diffraction (SAED) pattern of the dots which manifests that the material obtained is polycrystalline in nature. Figure 3.24g shows a size distribution histogram which demonstrates that the $CuInSe_2$ quantum dots grown in this study are fairly monodispersed.

3.9 Growth of copper gallium diselenide nanostructures

3.9.1 Copper gallium diselenide thin films

1:4 molar equivalents of $[Cu_4(^iPr_2PSe_2)_4]$ and $[Ga(^iPr_2PSe_2)_3]$ precursors, respectively were used to carry out deposition of $CuGaSe_2$ thin films by AACVD methods. A solution of 0.05 g (0.036 mmol) of Cu precursor $[Cu_4(^iPr_2PSe_2)_4]$ and 0.12 g (0.134 mmol) of Ga precursor $[Ga(^iPr_2PSe_2)_3]$ in 20 ml of tetrahydrofuran (THF) was converted into aerosols by an ultrasonic modulator and transferred to preheated glass substrates placed in an open tube CVD reactor. AACVD experiments were carried out at temperatures ranging from 300-500 °C. Poorly deposited films were obtained below 400 °C which showed very poor diffraction in powder XRD studies. However, greenish black transparent films were obtained at 400 - 450 °C deposition temperatures while the film deposited at 500 °C, showed a very fine black powder layer on the surface of substrates which may be attributed to access of the same deposited material. The optical band gap of the films was measured by direct bandgap method and it was found to be about 1.74 eV (Figure 3.25).

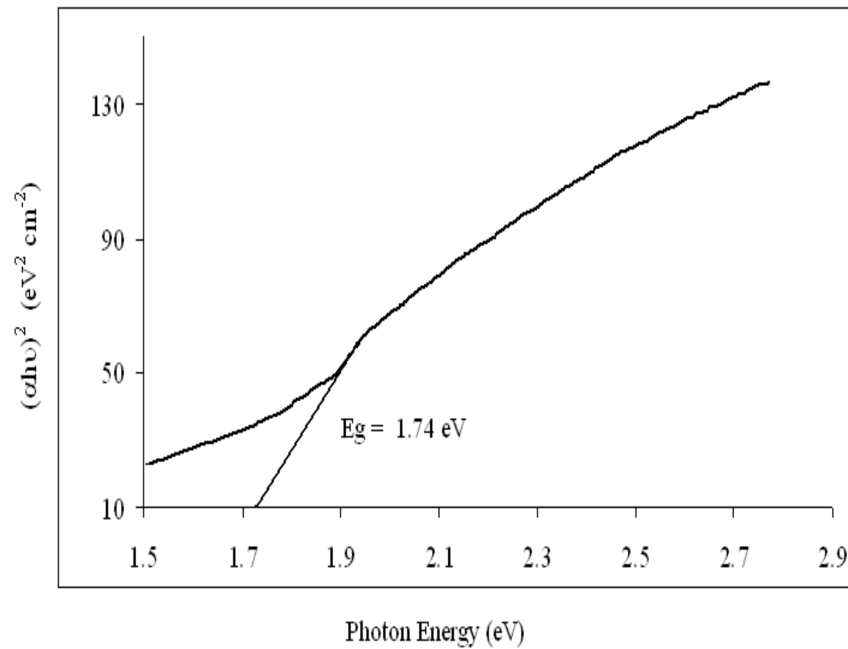

Figure 3.25 Plot of $(\alpha h\upsilon)^2$ *vs* band gap of $CuGaSe_2$ thin films showing band gap energy of 1.74 eV.

Powder X-ray diffraction patterns of deposited thin films of $CuGaSe_2$ are shown in the Figure 3.26. As mentioned earlier, films deposited at lower temperatures did not give a good diffraction pattern. Therefore, phase identification was not possible. However, broader and less sharp peaks obtained from thin films deposited at 400 - 450 °C show that the material is not very crystalline and consists of smaller grains. No extra peaks were observed in the diffraction pattern recorded at 400 °C, but some extra peaks assignable to copper selenide were found in diffraction pattern of the film deposited at 450 °C. At 500 °C, sharp diffraction pattern was obtained which showed deposition of tetragonal phase of chalcopyrite $CuGaSe_2$ (ICDD pattern 00-035-1100). The material showed preferred orientation along (112) plane which is typical of tetragonal phase of chalcopyrite compounds. Deposition experiments performed with 1:1 and 1:1.5 molar ratio of the precursor yielded berzelianite phase of $Cu_{2-x}Se$ with some unidentified impurities. The formation of binary $Cu_{2-x}Se$ preferentially occurs due to availability of more Cu atoms as compared to In atoms after thermal degradation of the precursor onto the substrate.

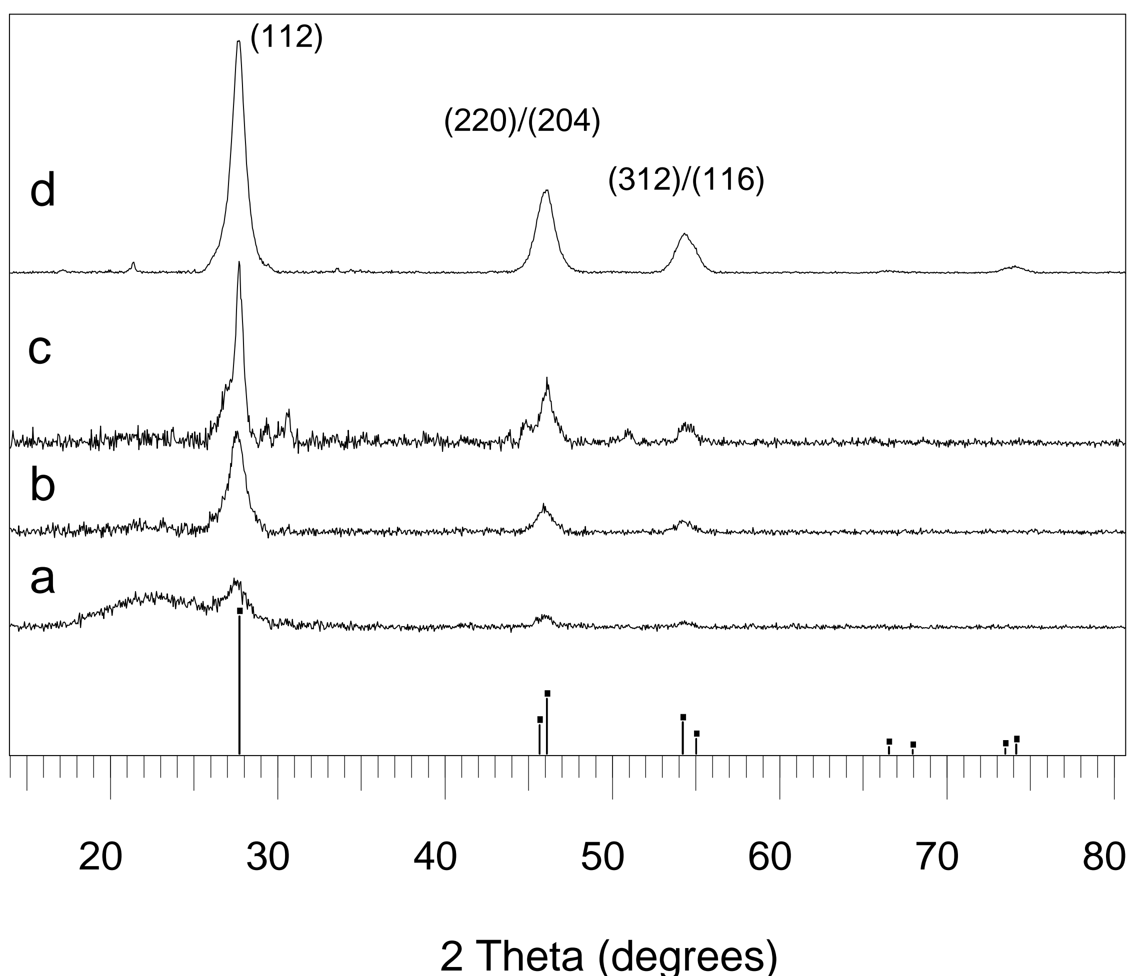

Figure 3.26 XRD pattern of as deposited $CuGaSe_2$ thin films at (a) 350 °C, (b) 400 °C, (c) 450 °C and (d) 500 °C from 1:4 molar ratios of Cu and Ga precursors

The surface morphology of the films was studied with the help of scanning electron microscopy. SEM images of thin films deposited at different temperatures are shown in Figure 3.27. It was observed that the morphology of CuGaSe2 thin films was strongly influenced by the deposition temperature. As expected, films deposited at 300 ºC showed deposition of very small globules which were not crystalline enough to give good diffraction pattern. SEM images of thin films deposited at 350 °C and 400 °C reveal the formation of nano wires. These wires are randomly formed onto the surface of the substrate yielding densely covered and well adhered films. Films deposited at 450 ºC exhibit rosette like structures in which individual layers of the materials are stacked over each other to give this morphology. Deposition at 500 ºC resulted in formation of randomly oriented globular structures of uniform size.

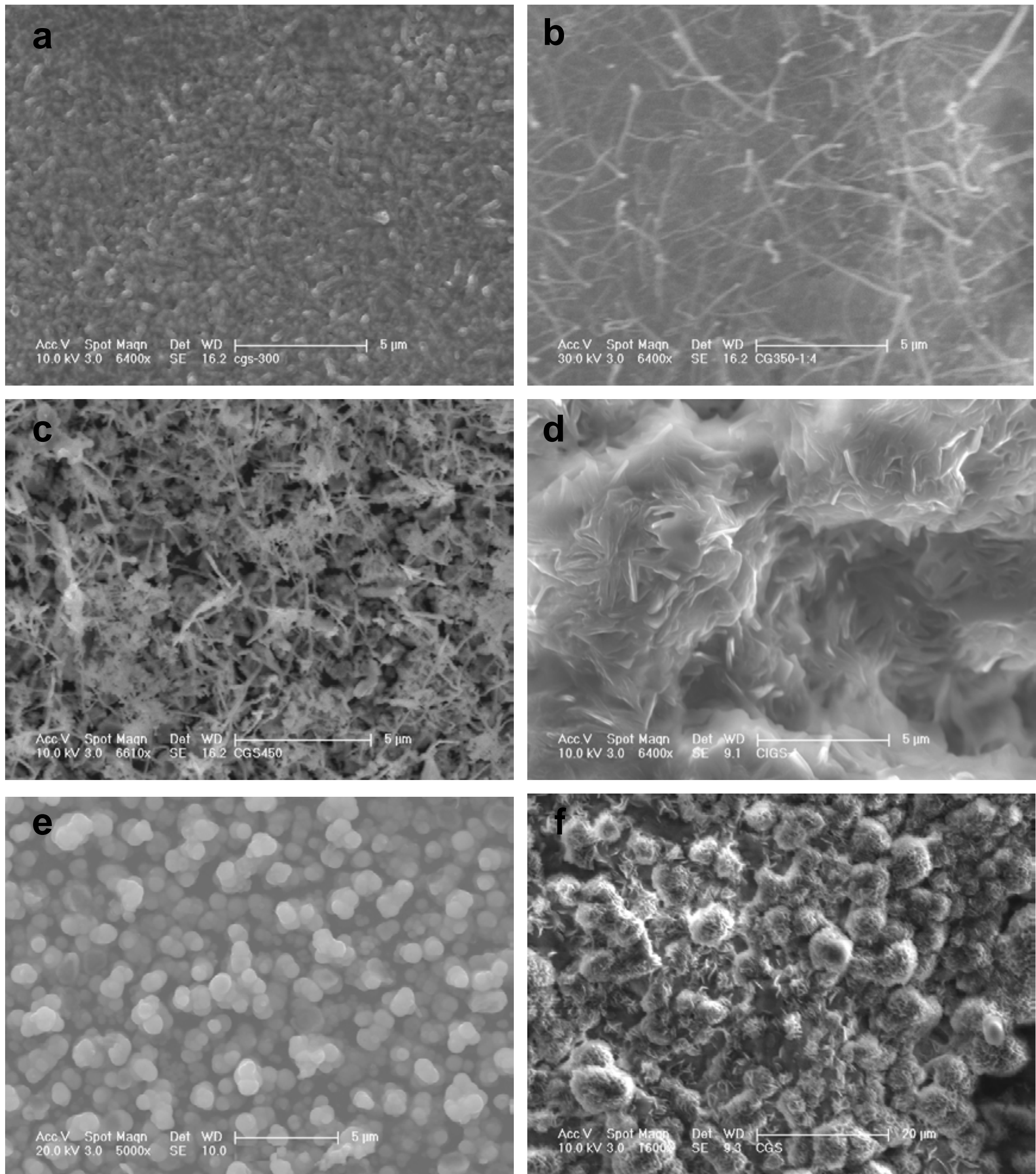

Figure 3.27 SEM images of as deposited $CuGaSe_2$ thin films at (a) 300 °C, (b) 350 °C, (c) 400 °C, (d) 450 °C and (e) & (f) 500 °C.

Higher magnification images reveal that these globules are formed by morphological transformations occurring in stacked layers at higher deposition temperatures. Energy dispersive X-ray analysis showed a stoichiometric ratio closer to the expected 1:1:2 ratio for copper, gallium and selenium. However, a slight excess of Se was found in the films deposited at lower temperatures. Phosphorus contamination was observed in thin films deposited below 400 ºC,

however no considerable phosphorous contamination is observed in films deposited above 400 °C.

The surface profile of the films was further examined with the help of Atomic force microscopy (AFM). Two-dimensional and three dimensional AFM images of $CuGaSe_2$ thin film deposited at 450 °C are shown in Figure 3.28, which shows root mean square roughness of 41.39 nm for the surface of as deposited film.

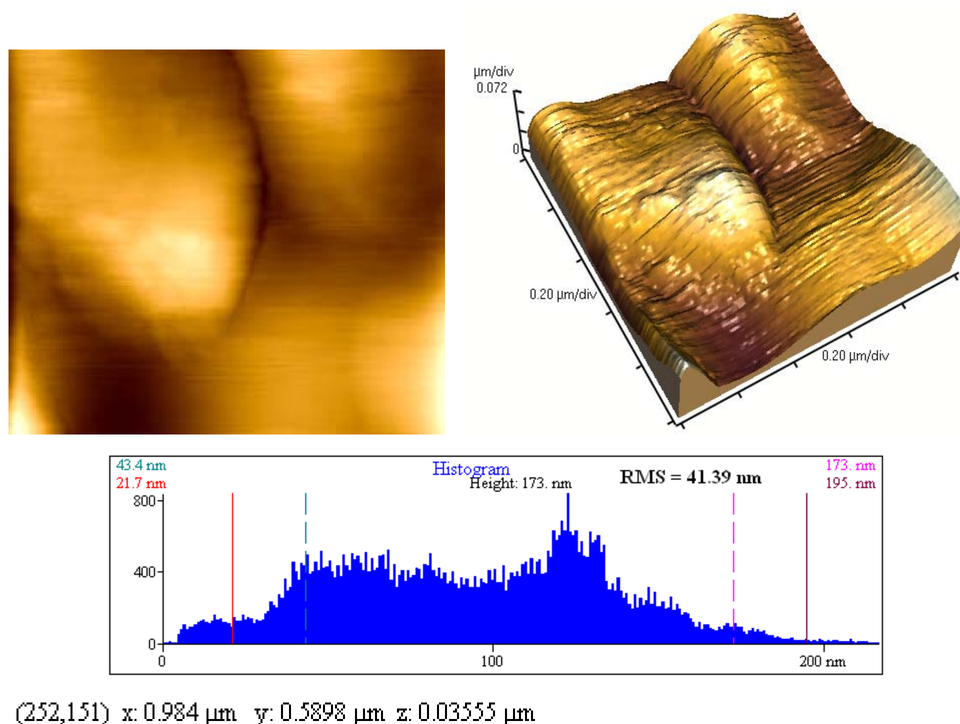

Figure 3.28 1D and 3D AFM images of as grown $CuGaSe_2$ thin films at 450°C from 1:4 equivalent of $[Cu_4(^{i}Pr_2P_2Se_2)_4]$ and $[Ga(^{i}Pr_2PSe_2)_3]$ respectively along with AFM histogram showing size distribution and surface roughness

3.9.2 Copper gallium diselenide nanoparticles

Thermolysis of 1:4 molar ratios of copper precursor $[Cu_4(^{i}Pr_2PSe_2)_4]$ and gallium precursor $[Ga(^{i}Pr_2PSe_2)_3]$, respectively in HDA gave monodispersed and predominantly spherical copper gallium diselenide ($CuGaSe_2$) nanoparticles. Figure 3.29 represents UV-Vis absorption spectrum of HDA capped $CuGaSe_2$ nanoparticles grown at 250 °C. The absorption curve shows a broad shoulder with a tail in long wavelength direction. The optcal absorption band edge at around 612 nm for HDA capped $CuGaSe_2$ nanoparticles, is significantly blue shifted as compared to corresponding band edge for bulk (732

nm). This indicates the presence of quantum confinement in grown $CuGaSe_2$ nanoparticles.

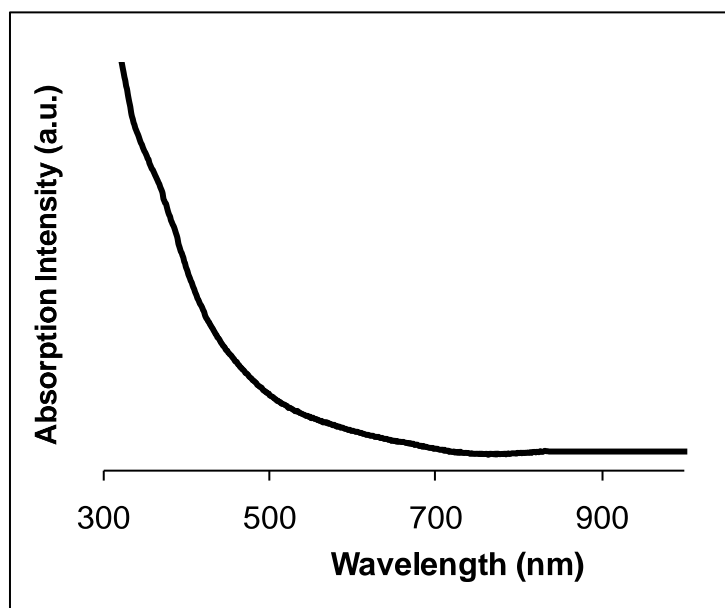

Figure 3.29 UV-Vis absorption spectrum of HDA capped $CuGaSe_2$ nanoparticles grown at 250 °C

Powder XRD pattern of HDA capped $CuGaSe_2$ nanoparticles is shown in Figure 3.30. Analysis of the XRD pattern showed growth of the tetragonal phase of $CuGaSe_2$ material corresponding to standard ICDD pattern 00-035-1100. It showed an intense diffraction peak at 2θ = 27.77° which is oriented along (112) plane of the tetragonal crystal lattice. Other prominent peaks observed in the diffraction pattern appear at 2θ = 46.11° and 54.23° which can be indexed to (220)/(204) and (312)/(116) planes of the tetragonal chalcopyrite crystal lattice, respectively. No diffraction peaks for binary phases of CuSe and GaSe were observed in the diffraction pattern. Appearance of sharp diffraction peaks was indicative of relatively larger size of the nanoparticles. The Scherer formula was used to calculate size of the quantum dots and calculated size was found to be 14.8 nm.

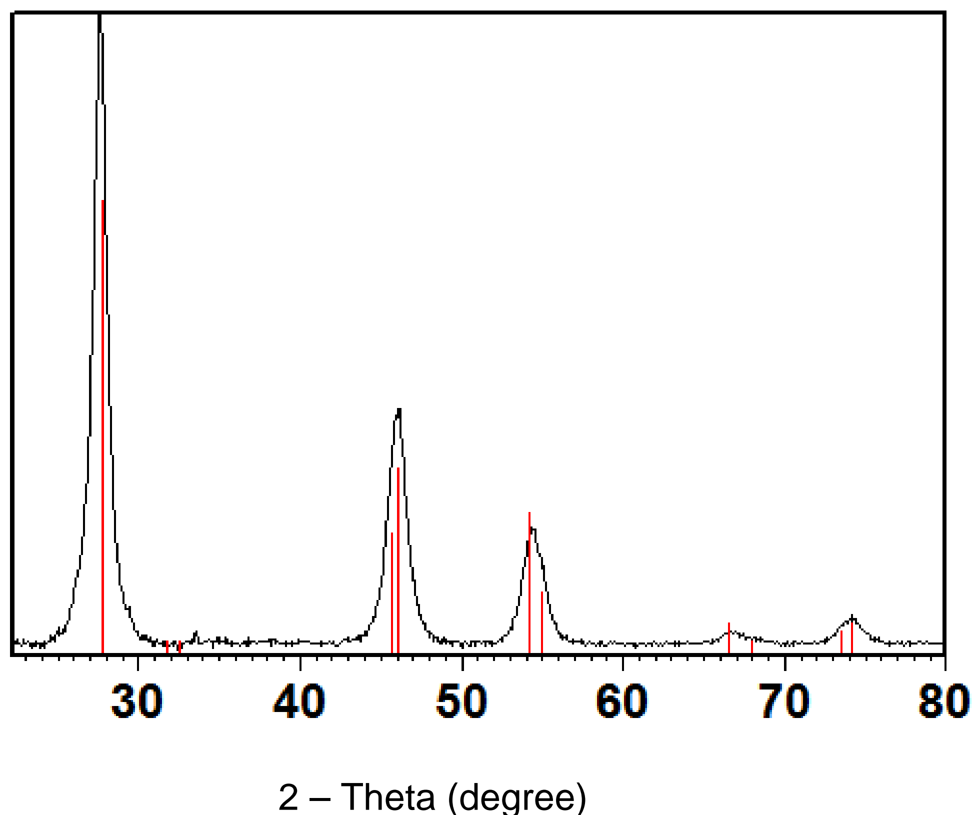

Figure 3.30 XRD pattern of HDA capped $CuGaSe_2$ nanoparticles grown at 250 °C

Representative TEM images of grown $CuGaSe_2$ quantum dots are shown in Figure 3.31(a-d), histogram showing size distribution of the nanoparticles is shown in Figure 3.31(e). In these TEM images, well passivated and fairly spaced quantum dots with somewhat spherical morphology and narrow size distribution are evident. Previously, there have been very few reports of the growth of phase pure, monodispersed $CuGaSe_2$ nanoparticles. Mean size of the nanoparticles was found to be 13.5 ± 2.9 nm which is agrees well with the above mentioned size calculated by using Scherrer formula. The morphology of the particles, not being perfectly spherical also contributed towards deviation from mean size. Despite repeated attempts, lattice fringes could not be obtained for this material.

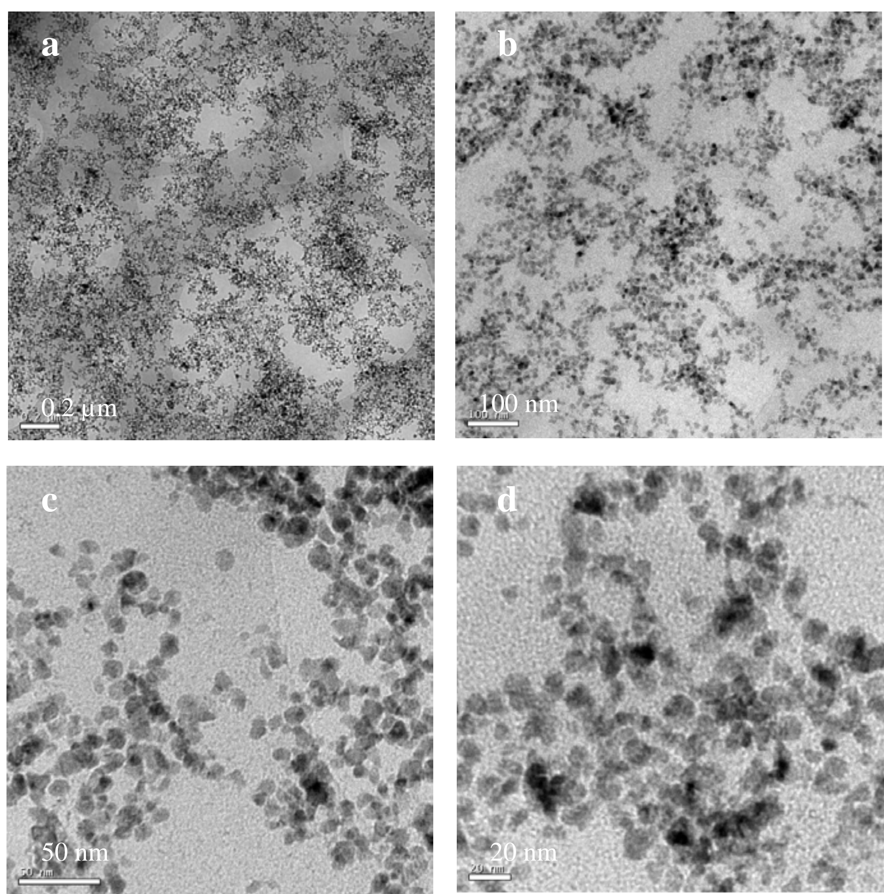

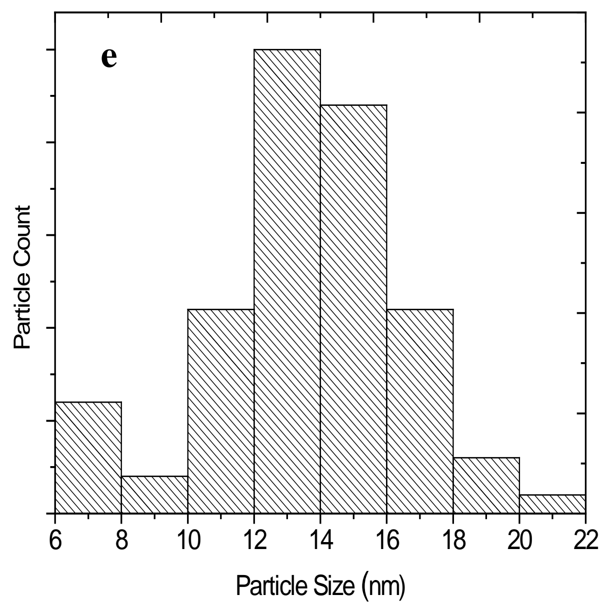

Figure 3.31 (a - d) TEM images of HDA capped $CuGaSe_2$ nanoparticles grown at 250 °C (e) Histogram showing size distribution of HDA capped $CuGaSe_2$ nanoparticles

3.10 Growth of copper indium gallium diselenide (CIGS) nanostructures

3.10.1 Deposition of $CuIn_{0.7}Ga_{0.3}Se_2$ thin films

Thin films of CIGS material were deposited onto glass substrates by using different molar equivalents of copper precursor [$Cu_4(^iPr_2PSe_2)_4$], indium precursor [$In(^iPr_2PSe_2)_3$] and gallium precursor [$Ga(^iPr_2PSe_2)_3$] to obtain films of varying stoichiometric combinations. Deposition experiments were carried out using 1:1:1, 1:2:2 and 1:2:4 molar ratios of copper, indium and gallium precursor, respectively at temperatures ranging from 300 to 500 ºC. The flow rate of carrier gas Ar was controlled by a Platon flow gauge. For all molar ratios, black shiny films were obtained at temperatures of 400 °C. At 500 °C, the films were covered by black powdery material. Poor coverage of the substrates was obtained at temperatures below 400 °C.

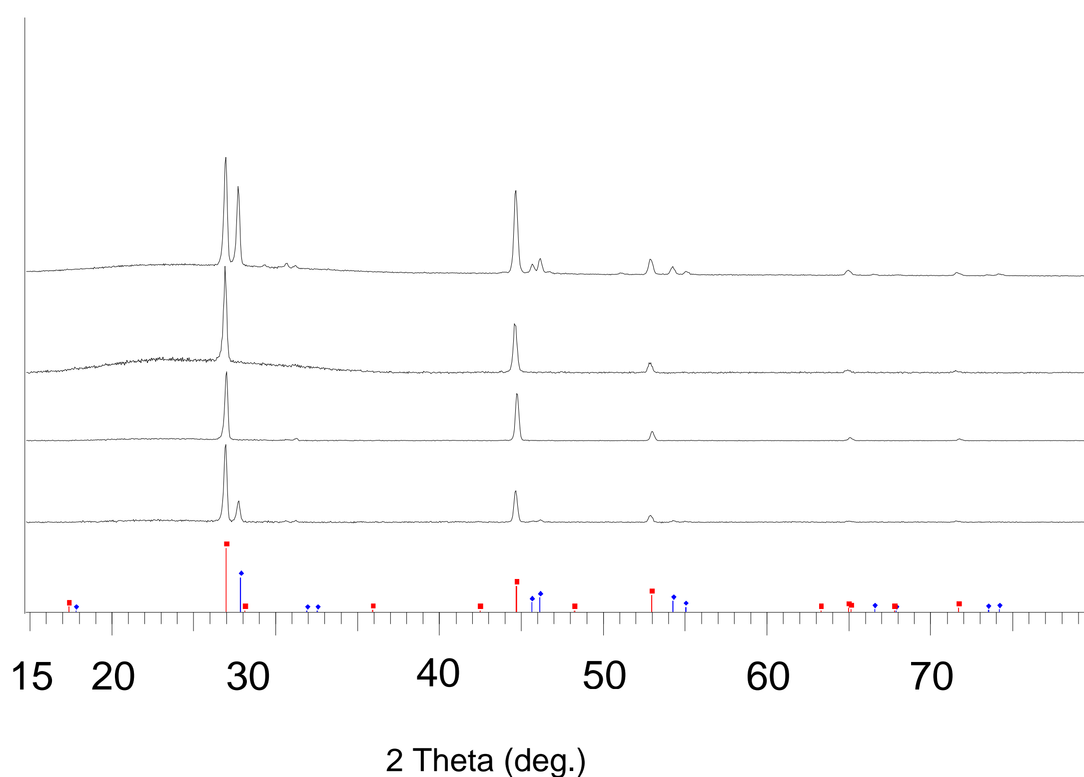

Figure 3.32 (a) XRD patterns of deposited $CuIn_{1-x}Ga_xSe_2$ in 1:1:1 ratio showing $CuIn_{0.7}Ga_{0.3}Se_2$ along with $CuGaSe_2$ as secondary phase

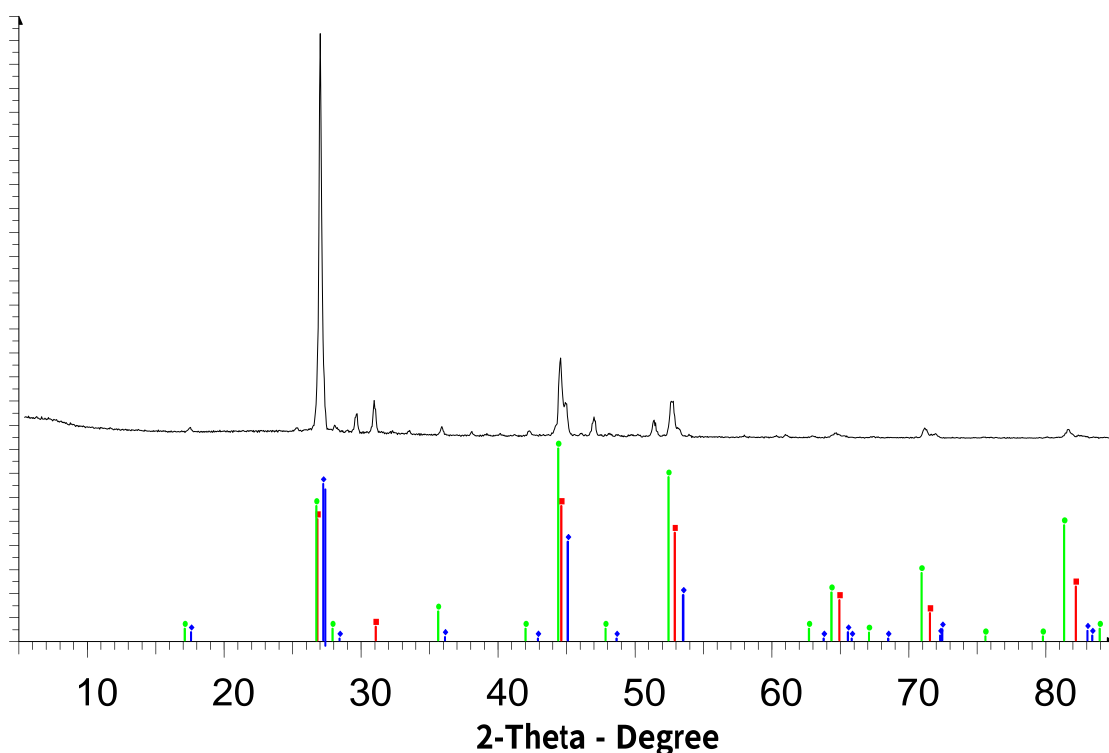

Figure 3.32(b) XRD patterns of deposited $CuIn_{1-x}Ga_xSe_2$ in 1:2:4 ratios at 450 ^oC showing $CuIn_{0.7}Ga_{0.3}Se_2$ along with $CuInSe_2$, $Cu_{2-x}Se$ and α-In_2Se_3 as additional phases.

Powder XRD patterns of thin films grown from different molar combinations of precursors are shown in Figures 3.32a & b. Analysis of the XRD patterns revealed that material deposited in case of 1:1:1 and 1:2:4 molar ratios of Cu, In and Ga precursors respectively, was multiphasic in nature. Besides CIGS, $CuGaSe_2$, $Cu_{2-x}Se$ and $CuInSe_2$ were present as impurities affecting microstructure of the films. However, in deposition experiments involving 1:2:2 molar ratios of copper, indium and gallium precursors, respectively (Fig. 3.33), pure, mono-phasic material, with no traceable impurities was deposited. Diffraction peaks obtained in this case were assignable to tetragonal $CuIn_{0.7}G_{0.3}Se_2$ crystallographic phase (standard ICDD pattern 00-035-1102) with preferred orientation along (112) plane. The well defined and sharp diffraction peaks confirmed that the material was sufficiently crystalline and purity of as deposited chalcopyrite material was evident from the absence of any additional diffraction peaks from binary phases or impurities.

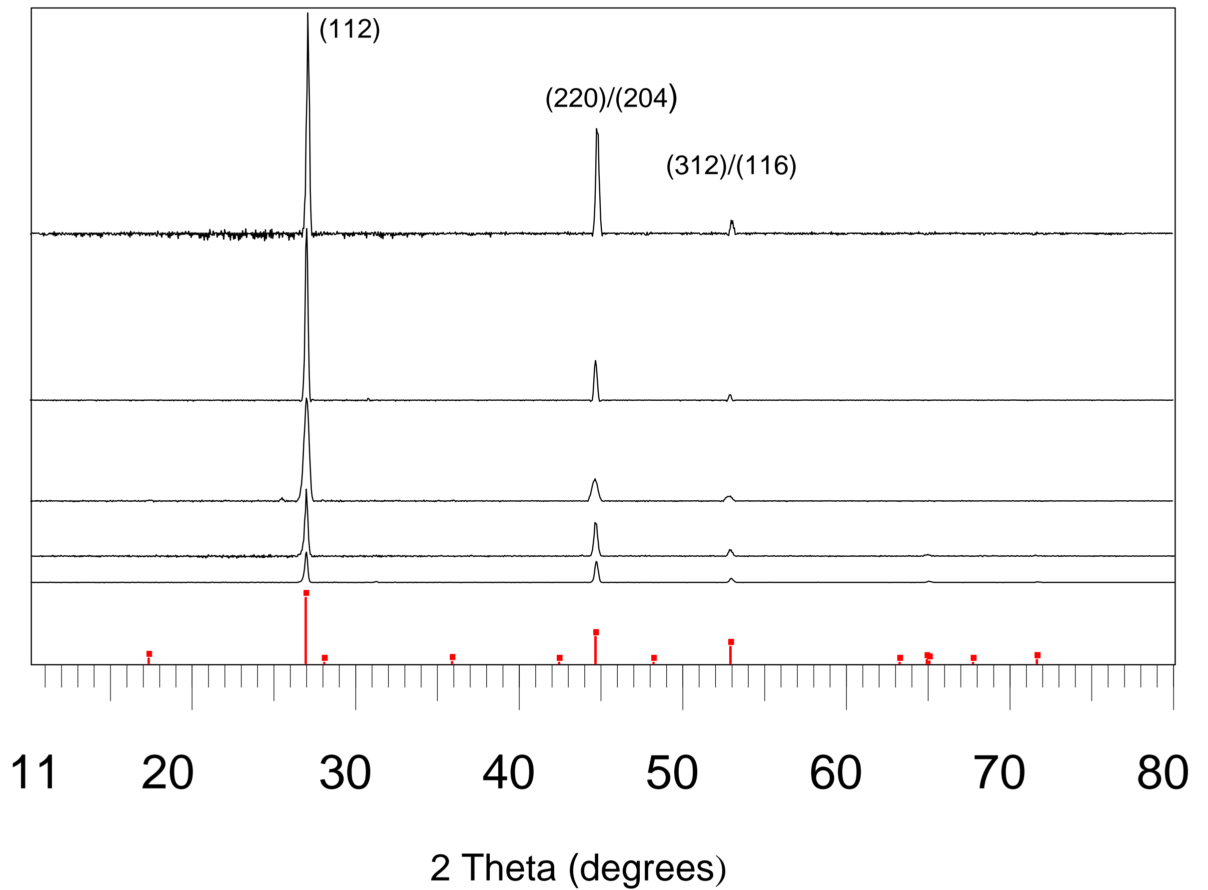

Figure 3.33 XRD pattern of deposited $CuIn_{0.7}Ga_{0.3}Se_2$ thin films at (a) 300 °C, (b) 350 °C, (c) 400 °C, (d) 450 °C and (e) 500 °C from 1:2:2 molar equivalents of $[Cu_4(^{i}Pr_2P_2Se_2)_4]$, $[In(^{i}Pr_2PSe_2)_3]$ and $[Ga(^{i}Pr_2PSe_2)_3]$ respectively.

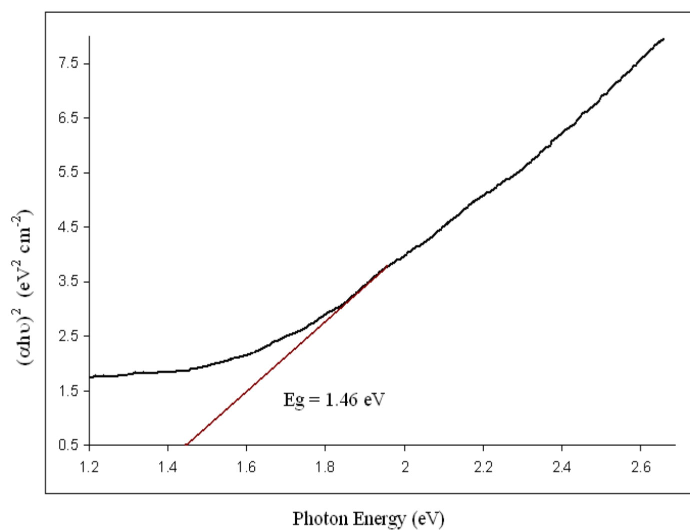

Figure 3.34 Plot of $(\alpha h\upsilon)^2$ *vs* band gap of $CuIn_{0.7}Ga_{0.3}Se_2$ thin films showing band gap energy of 1.46 eV.

Optical bandgap of $CuIn_{0.7}Ga_{0.3}Se_2$ thin films deposited from 1:2:2 molar equivalents of copper, indium and gallium precursors, respectively was determined by extrapolating the straight line part of the $(\alpha h\upsilon)^2$ vs hυ curve to the hυ axis, where $(\alpha h\upsilon)^2 = 0$. Bandgap of the films was found to be 1.46 eV (Figure 3.34). Values of band gap energies reported in literature for CIGS vary from 1.04 to 1.68 eV.[18, 23]

Scanning electron microscopy was used to study the microstructure of the films. SEM images, as shown in Figure 3.35, revealed that the films were uniformly covered with material having well defined shapes of grains. It was further observed that the shapes of grains are influenced by deposition

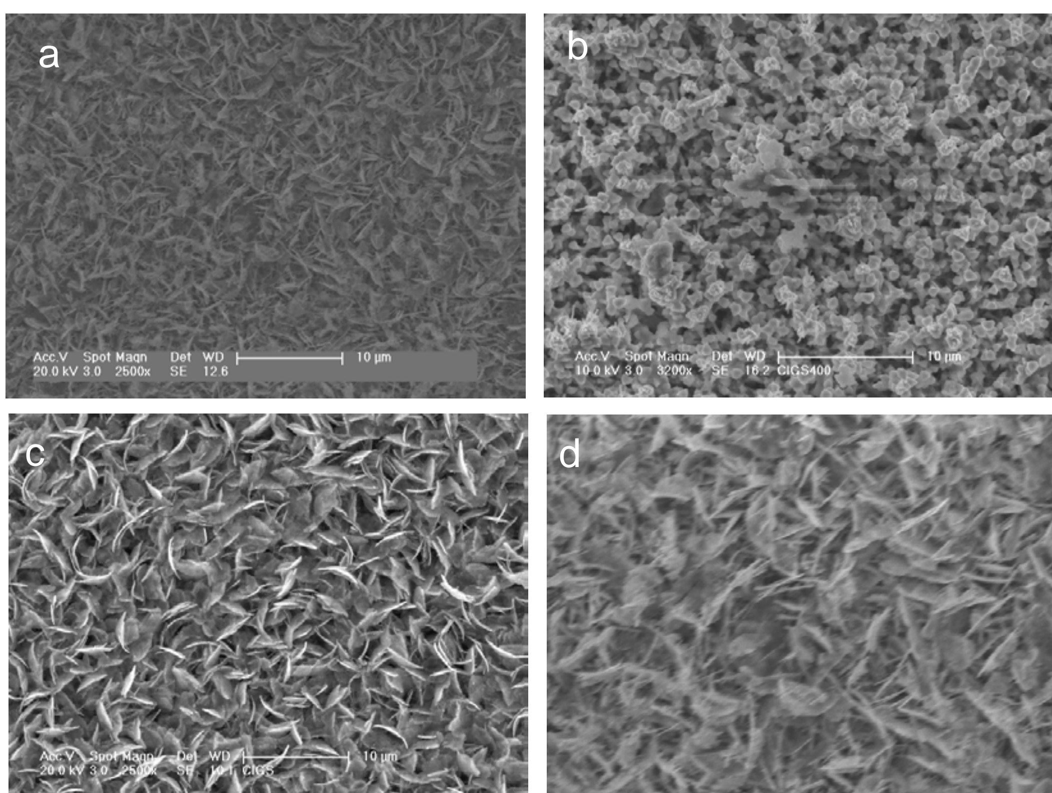

Figure 3.35 SEM images of as deposited $CuIn_{0.7}Ga_{0.3}Se_2$ at (a) 350 °C, (b) 400 °C, (c) 450 °C and (d) 500 °C from 1:2:2 molar equivalent of $[Cu_4(^iPr_2P_2Se_2)_4]$, $[In(^iPr_2PSe_2)_3]$ and $[Ga(^iPr_2PSe_2)_3]$, respectively.

temperature. Randomly oriented flake-like grains were observed at 300 and 350 °C temperature, while triangular non-edged faceted grains (~20-40 nm) were observed at 400 °C. Evenly distributed, uniform sized flakes like crystallites were deposited at 450 °C to 500 °C. These images reveal that the surface

roughness of the film is decreased as larger and more uniform grains are deposited at higher deposition temperature.

The same is evidenced from AFM analysis shown in two-dimensional and three dimensional AFM images (Figure. 3.36 & 3.37), which revealed that the root mean square roughness of CIGS deposited at 400 ° was 55.46 nm.

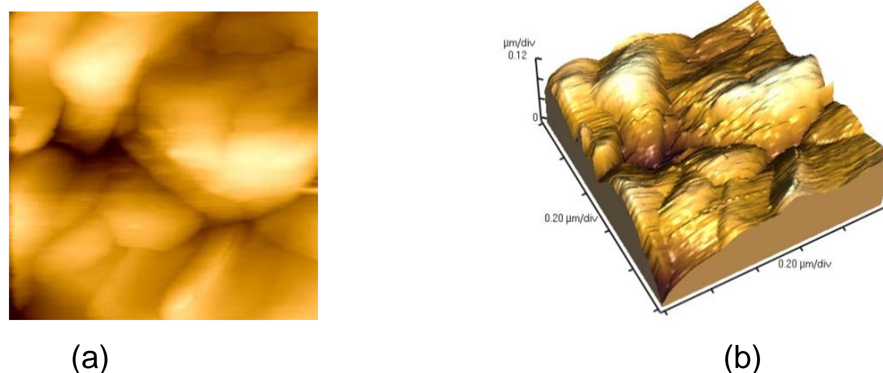

(a) (b)

Figure 3.36 (a) 2D (b) 3D AFM image of as deposited $CuIn_{0.7}Ga_{0.3}Se_2$ thin films at 400 °C with Root mean square roughness 55.46 nm.

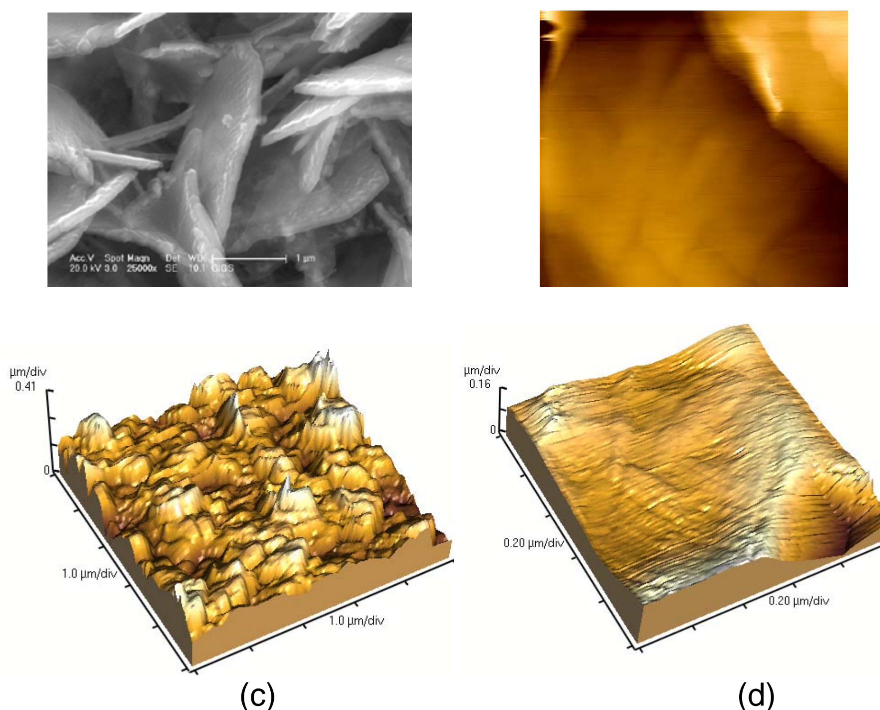

(c) (d)

Figure 3.37 (a) SEM image of $CuIn_{0.7}Ga_{0.3}Se_2$ at 450 °C, (b) 2D, (c) 3D AFM images of as deposited $CuIn_{0.7}Ga_{0.3}Se_2$ at 450 °C with Root mean square roughness 44.50 nm, (d) 3D AFM image of nano indent type microstructures found at the surface of the film.

while CIGS deposited at 450 °C had a root mean square roughness of 44.50 nm. EDX data of CIGS across the entire film revealed a uniform composition that was fairly compatible the stoichiometric ratio expected for $CuIn_{0.7}Ga_{0.3}Se_2$.

SEM images of thin films deposited from 1:1:1 molar equivalent of copper, indium and gallium precursors revealed presence of additional phases, especially $Cu_{2-x}Se$ and $CuInSe_2$ along with grains of CIGS material. Deviation from targeted stoichiometry was observed in all these experiments. Attempts to deposit gallium rich CIGS thin films by increasing the molar ratio of the gallium precursor (by using 1:2:4 molar ratio for copper, indium and gallium precursors) was unsuccessful. In this case, additional phases of $CuGaSe_2$ and Ga_2Se_3 were obtained. These results fully conform to those deduced from aforementioned XRD analysis of the films. A very interesting feature is shown in Figure 3.38. Big grains of $CuInSe_2$ in trigonal shapes (ca. 3.37nm x 3.91) were found randomly distributed on the surface of films along with other secondary phases.

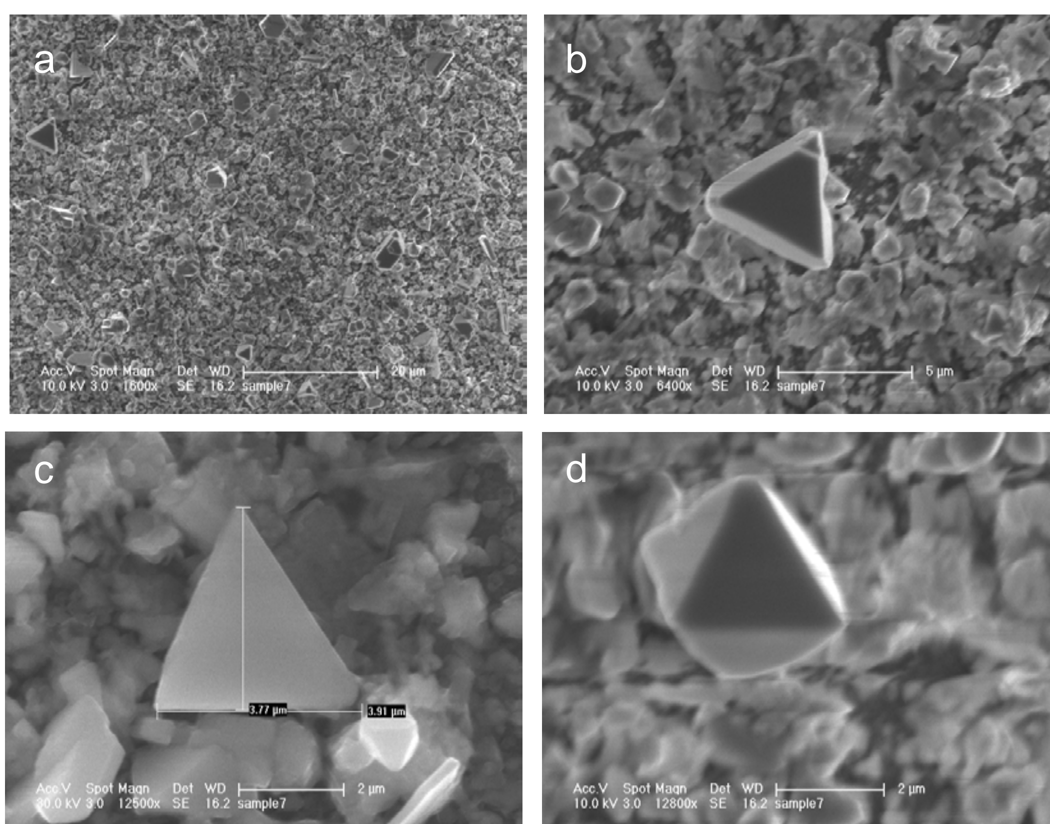

Figure 3.38 SEM images of as deposited $CuIn_{0.7}Ga_{0.3}Se_2$ thin films in 1:2:4 ratio at 450 ^{o}C showing various secondary phases especially random distribution of big grains of $CuInSe_2$.

3.10.2 Copper indium gallium diselenide nanoparticles

Growth of $CuIn_xGa_{1-x}Se_2$ nanoparticles was carried out using the similar approach as utilized for growth of $CuGaSe_2$ nanocrystals, but in this case varying quantities of In precursor and Ga precursor were used to obtain different stoichiometric compositions of CIGS materials. A brief summary of the combination of precursors used and stoichiometric compositions of CIGS materials obtained after reaction is given in Table 3.3.

Table 3.3 Summary of the combination of precursors used and stoichiometric compositions of CIGS materials obtained after reaction

Moles of precursors used in reaction (mmol)			Stoichiometric composition of CIGS obtained		
Cu Precursor	In Precursor	Ga Precursor	From XRD	From EDX	Lattice Parameter 'c'
0.1	0.2	0.1	-	$CuIn_{0.81}Ga_{0.19}Se_2$	11.506
0.1	0.2	0.2	$CuIn_{0.7}Ga_{0.3}Se_2$	$CuIn_{0.68}Ga_{0.32}Se_2$	11.442
0.1	0.2	0.4	$CuIn_{0.5}Ga_{0.5}Se_2$	$CuIn_{0.54}Ga_{0.46}Se_2$	11.361
0.1	0.2	0.5	$CuIn_{0.4}Ga_{0.6}Se_2$	$CuIn_{0.47}Ga_{0.53}Se_2$	11.296
0.1	0.2	0.8	-	$CuIn_{0.19}Ga_{0.81}Se_2$	11.148

It was possible to tune the In/Ga ratio across the whole range of stoichiometric compositions with the value of x ranging from 0 to 1 using this approach. However, relatively more amount of gallium precursor was required than theoretically calculated to obtain a desired stoichiometric combination. For instance, when equimolar ratios of copper and indium were used in the reaction, the material obtained was $CuIn_{0.7}Ga_{0.3}Se_2$ and for obtaining $CuIn_{0.5}Ga_{0.5}Se_2$, 0.4 mmol of gallium precursor were used with 0.2 mmol of In precursor. Gallium rich composition $CuIn_{0.4}Ga_{0.6}Se_2$ was obtained when 0.5 mmol of Ga precursor and 0.2 mmol of In precursor were used in the reaction. Standard ICDD patterns were not available for stoichiometric combinations obtained by using 0.1 mmol and 0.8 mmol of the Ga precursor with 0.2 mmol of In precursor.

Previously, Korgel *et. al.*, have obtained different stoichiometric compositions of CIGS material, by using a route that involved direct combination of Cu, In and Ga salts and solid Se in a flask containing oleylamine and subsequent heating to 240 °C for 4 hours. In their work, they have obtained In/Ga ratio of the nanocrystals which were consistent with the mole ratios of In and Ga in the reaction mixture.[22]

However, many others have pointed out that in various approaches used for synthesis of $CuIn_xGa_{1-x}Se_2$, formation of Ga-containing phases would require relatively longer reaction times and/or higher temperatures than those employed for deposition of indium containing phases. This means that initially $CuInSe_2$ is formed but at some later stage of the reaction, Ga atoms start replacing In atoms in the matrix. Therefore, longer reaction times and higher temperatures might yield stoichiometric combinations of the CIGS material that are consistent with the molar ratios of In and Ga precursors used in the reaction. However, these reaction conditions in our experiments resulted in the formation of bulk materials which were not dispersible in commonly used non-polar solvents.

Figures 3.39 shows powder XRD data of CIGS nanoparticles grown by thermolyzing different molar ratio combinations of Ga/In precursors, while molar ratios of the copper precursor was the same in all reactions. It was evident from analysis of the XRPD patterns that the diffraction peaks were clearly assignable to the tetragonal chalcopyrite crystallographic phase of CIGS material. Relatively broad peaks were obtained which are indicative of crystallite size in nano size domain. In all cases, a preferential orientation along (112) plane was observed, while other prominent peaks originate from (204)/(220) and (312) plane of the lattice. Absence of any additional diffraction peaks suggests purity of the material. As Ga content is increased in the material, gradual shifting of diffraction peaks to higher 2θ is observed, which is consistent with theoretical expectations. When relatively smaller Ga atoms substitute In atoms in the lattice, this results in gradual change of lattice parameters.

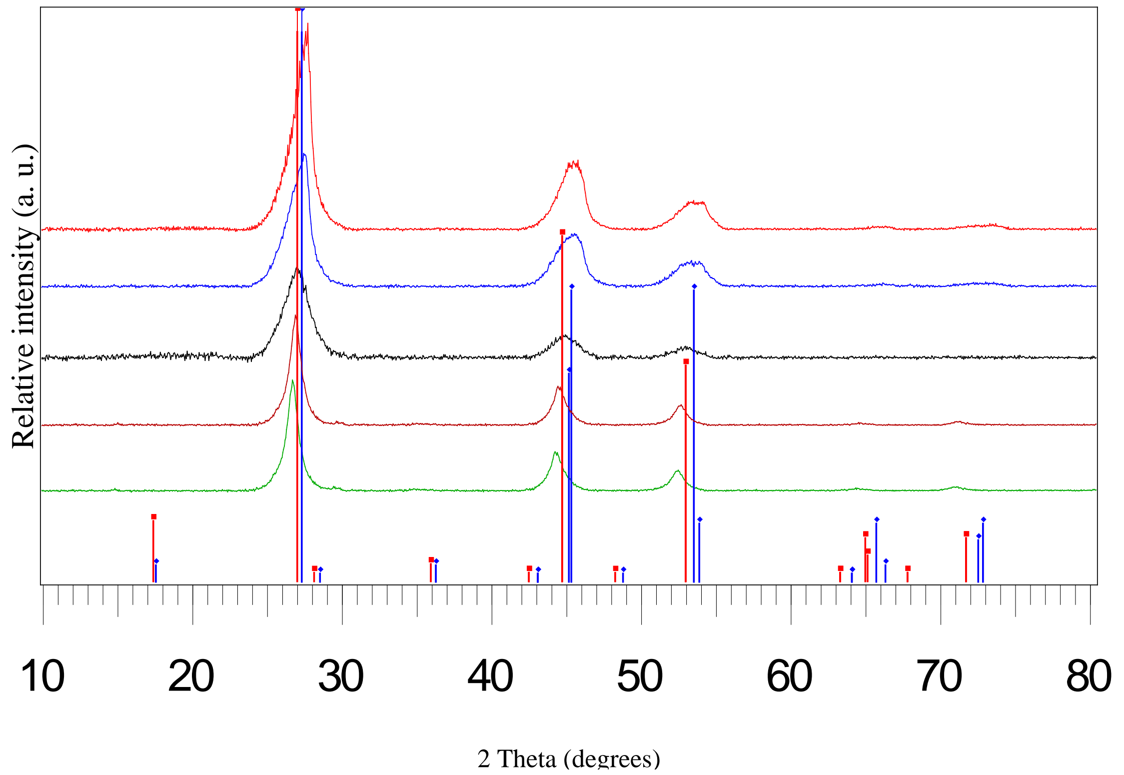

Figure 3.39 Powder XRD Pattern of various stoichiometric compositions of HDA capped $CuInGaSe_2$ nanoparticles indexed with standard ICDD Patterns for $CuIn_{0.7}Ga_{0.3}Se_2$, $CuIn_{0.5}Ga_{0.5}Se_2$ and $CuIn_{0.4}Ga_{0.6}Se_2$. . XRD Patterns shift to higher diffraction angles with increase in gallium content

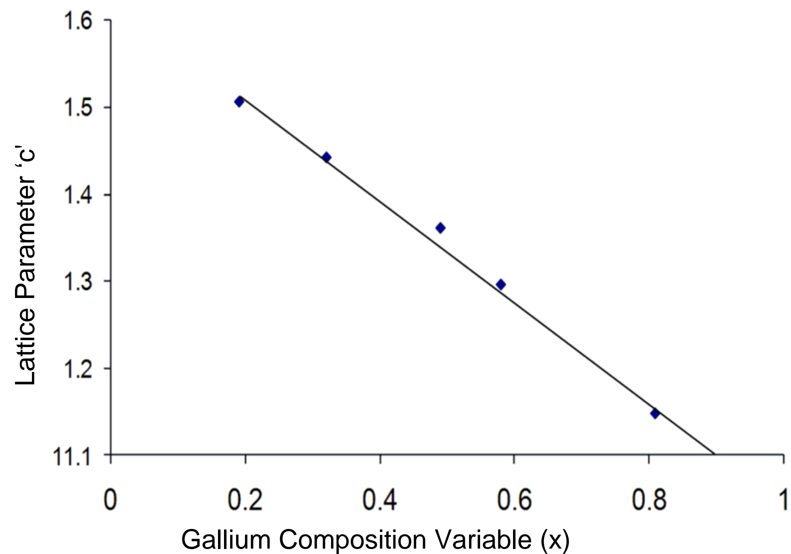

Figure 3.40 Plot of the Gallium composition variable x in $CuIn_{(1-x)}Ga_xSe_2$ verus lattice parameter 'c'

Vegard's law states that there should exist a linear relationship between the lattice parameter c and the composition x. These lattice parameters c were calculated from the XRD patterns shown in Figure 3.39. Plot of the gallium composition variable x in $CuIn_{(1-x)}Ga_xSe_2$ verus lattice parameter 'c' for various stoichiometric compositions obtained is shown in Figure 3.40. Value of lattice parameter 'c' decreases linearly with gradual decrease in In composition in Ga rich phases. This confirms the formation of a homogeneous alloy structure. The indium rich phase of CIGS i.e $CuIn_{0.7}Ga_{0.3}Se_2$ corresponded to a standard ICDD pattern 00-35-1102, $CuIn_{0.5}Ga_{0.5}Se_2$ corresponded to 00-040-1488 while gallium rich phase $CuIn_{0.4}Ga_{0.6}Se_2$ corresponded to standard ICDD pattern 00-035-1101. Shifting of diffraction angles to higher values of 2 θ can be more clearly visible in Figure 3.41, where magnification of (112) peak from corresponding XRD pattern is shown along with standard ICDD patterns for various stoichiometric compositions of the CIGS materials. Within error limits of the EDX technique, the In/Ga ratio of the nanocrystals determined by the EDX analysis coincided with the In/ Ga ratios obtained from calculations of lattice parameter c from the corresponding XRPD patterns. Additionally, no noticeable differences in particle to particle Cu/In/Ga ratio were observed in EDX measurements on different nanoparticles in the sample.

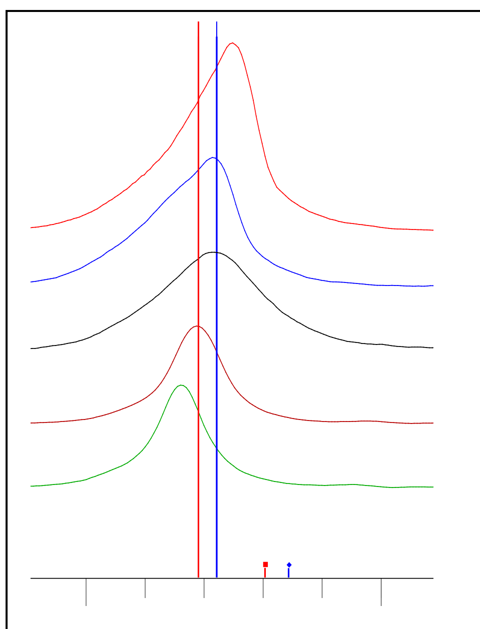

Figure 3.41 Magnification of the (112) peak of XRPD patterns of various compositions of CIGS. Vertical lines show standard ICDD patterns 00-35-1102 (red) and 00-35-1101 (blue)

Figure 3.42 (a-d) shows TEM images of tetragonal $CuIn_{0.7}Ga_{0.3}Se_2$ quantum dots with an average size diameter of 14 nm. This value is consistent with the particle size evaluated for this sample by the Scherrer equation from powder XRD data. Both HRTEM and powder XRD data confirm that the nanoparticles are crystalline having tetragonal morphology. The d-spacing observed in the HRTEM images are consistent with the (112) plane of the tetragonal $CuIn_{0.7}Ga_{0.3}Se_2$ material. Figure 3.42(e) shows SAED pattern of the $CuIn_{0.7}Ga_{0.3}Se_2$ nanoparticles which clearly demonstrates the polycrystalline nature of the sample. A histogram representing size distribution for $CuIn_{0.7}Ga_{0.3}Se_2$ quantum dots is shown in Figure 3.42 (f). The average size comes out to be 14 nm with standard deviation of 2.21. Previously, there are very limited reports of CIGS nanomaterials synthesis with narrow size distribution.

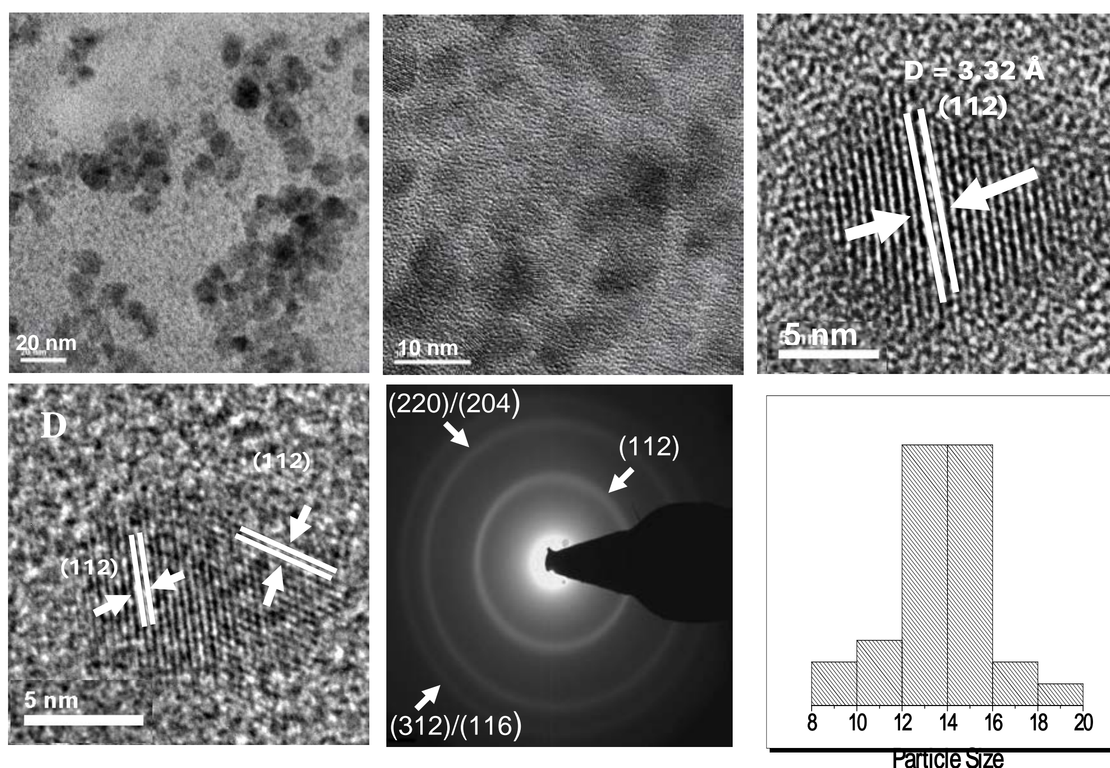

Figure 3.42 (a-d) show TEM images of tetragonal$CuIn_{0.7}Ga_{0.3}Se_2$ quantum dots (e) SAED pattern of the $CuIn_{0.7}Ga_{0.3}Se_2$ nanoparticles and (f) Histogram representing size distribution for $CuIn_{0.7}Ga_{0.3}Se_2$ quantum dots

References

1 W. Shockley and H, J. Queisser. *J. Appl. Phys.,* 1961, **32**,510.

2 I. Repins, M. Contreras, Y. Romero, Y. Yan, W. Metzger, J. Li, S. Johnston, B. Egaas, C. DeHart, J. Scharf, B. E. McCandless and R. Noufi. *IEEE Photovoltaics Specialists Conference Record*, 2008, 33; K. Ramanathan, M. A. Contreras, C. L. Perkins, S. Asher, F. S. Hasson, J. Keane, D. Young, M. Romero, W. Metzger, R. Noufi, J. Ward and A. Duda, *Prog. Photovolt. Res. Appl.,* 2003, **11,** 225.

3 J. Kessler, M. Bodegard, J. Hedstrom, L. Stolt. *Proceedings of 16th European Photovoltaic Solar Energy Conference*, Glasgow, 2000, 2057.

4 Y. Tanaka, N. Akema, T. Morishita, D. Okumura, K. Kushiya, *Proceedings of 17th EC Photovoltaic Solar Energy Conference,* Munich, Germany, 2001, 989.

5 C. Q. Nguyen, A. Adeogun, M. Afzaal, M. A. Malik and P. O'Brien, *Chem. Commun.*, 2006, 2179.

6 C. Q. Nguyen, A. Adeogun, M. Afzaal, M. A. Malik and P. O'Brien, *Chem. Commun.*, 2006, 2183.

7 P. P. Hankare, A. S. Khomane, P. A. Chate, K. C. Rathod and K. M. Garadkar, *J. Alloys Compounds*, 2009, **469**, 478.

8 V. M. Bhuse, P. P. Hankare, K. M. Garadkar, A. S. Khomane, *Mater. Chem. Phys.*, 2003, **80**, 82.

9 Y. Hu, M. Afzaal, M. A. Malik and P. O'Brien, *J. Crystal Growth*, 2006, **297**, 61.

10 M. Afzaal, D. Crouch and P. O'Brien, *Mater. Sci. Eng. B,* 2005, **116**, 391.

11 C. Julien, A. Chevy, D. Siapkas, *Phys. Status Solidi,* 1990, **A 118**, 553.

12 N. Ravaprasadu, M. A. Malik and P. O'Brien, *J. Mater. Chem.*, 1999, 9, 2885.

13 J. Tabernor, P. Christian and P. O'Brien, *J. Mater. Chem.,* 2006, **16**, 2082.

14 M. Takumi, T. Ueda, Y. Koshio, H. Nishimura and K. Nagata, *Phys. Stat. Solidi B*, 2001, **223**, 271.

15 K. Ueno, M. Kawayama, Z. R. Dai, A. Koma and F. S. Ohuchi, *J. Cryst. Growth*, 1999, **207**, 69.

16 J. –H. Park, M. Afzaal, M. Helliwell, M. A. Malik, P. O'Brien and J. Raftery, *Chem. Mater.,* 2003**, 15***,* 4205.

17 V. Chikan and D. F. Kelly, *Nano Lett.*, 2002, **2(2)**, 141.

18 B. J. Stanbery, *Critical Reviews in Solid State and Materials Sciences*, 2002, **27(2),** 73.

19 R. H. Bari, L. A. Patil, P. S. Sonawane, M. D. Mahanubhav, V. R. Patil, P. K. Khanna, *Mater. Lett*. 2007, **61**, 2058.

20 J. M. Merino, J. L. Martın de Vidales, S. Mahanty, R. Dıaz, F. Rueda, and M. Leon, *J. Appl. Phys.,* 1996, **80**, 5610.

21 J. Tang, S. Hinds, S. O. Kelly and E. H. Sargent, *Chem. Mater.*, 2008, **20(22)**, 6906.

22 M. G. Panthani, V. Akhavan, B. Goodfellow, J. P. Schmidtke, L. Dunn, A. Dodabalapur, P. F. Barbara and B. A. Korgel, *J. Am. Chem. Soc.*, 2008, **130(49)**, 16770.

23 S. Seyrling, S. Bucheler, A. Chirila, J. Perrenoud, S. Wenger, T. Nakada, M. Gratzel, A.N. Tiwari, Photovoltaic Specialists Conference (PVSC), 2009, 34th IEEE, Philadelphia, PA; C. –H. Huang, *J. Phys. Chem. Solids*, 2008, **69**, 330; A. Kinoshita, M. Fukaya, H. Nakanishi, M. Sugiyama, S. F. Chichibu, *Phy. Stat. Sol.*, 2006, **3(8)**, 2539.

CHAPTER 4

CONCLUSION

Conclusion and future work

In present work, diisoprpyldiselenophosphinato-metal complexes $M_x[R_2PSe_2]_y$ (where M = Cu, In, Ga) have been synthesized and used as precursors for the deposition of binary ($Cu_{2-x}Se$, InSe and GaSe), ternary ($CuInSe_2$ and $CuGaSe_2$) and quaternary ($CuInGaSe_2$) metal chalcogenide thin films and nanoparticles. Thin films of $CuInSe_2$ and related materials were deposited by AACVD, whereas nanoparticles were grown by employing the colloidal approach. These techniques offers good control over size, morphology and stoichiometric composition of the materials. Deposited materials were characterized by using optical spectroscopy, powder X-ray diffraction (XRD), scanning electron microscopy (SEM), atomic force microscopy (AFM), transmission electron microscopy (TEM) and energy dispersive X-ray (EDX) analysis.

In case of binary materials, copper precursor $[Cu_4(^iPr_2PSe_2)_4]$ and indium precursor $In(^iPr_2PSe_2)_3$ underwent clean decomposition to give thin film of $Cu_{2-x}Se$ and In_2Se_3, respectively at deposition temperatures of 400 °C or higher. Similarly, thermolysis of the precursor in HDA/TOP system yielded clearly defined and passivated nanoparticles. However, neither good quality thin films nor nanoparticles could be deposited from the gallium precursor $Ga(^iPr_2PSe_2)_3$.

Good quality ternary ($CuInSe_2$ and $CuGaSe_2$) and quaternary metal chalcogenide $CuIn_{1-x}Ga_xSe_2$ (CIGS) thin films and nanocrystals were deposited using a combination of these precursors. In all cases, tetragonal chalcopyrite phase of the corresponding material was deposited. In case of nanoparticles, it was observed that size of the nanoparticles obtained could be tuned by changing the growth temperature, reaction time or precursor concentration. Longer reaction durations and higher growth temperatures yield larger nanoparticles. It was further demonstrated that by suitable adjustment of molar precursor ratios, materials with desired stoichiometric combinations may also be obtained. $CuIn_{1-x}Ga_xSe_2$ nanoparticles with variable values of x have been obtained in this study, whereas in case of thin films the deposited material was found to be $CuIn_{0.7}Ga_{0.3}Se_2$.

Future work can include other materials such as $AgInSe_2$, $AgGaSe_2$ and $AgIn/GaSe_2$ by using $[Ag_4(^iPr_2PSe_2)_4]$ as silver precursor.